



UNIVERSITÀ  
DEGLI STUDI  
DI PADOVA

UNIVERSITA' DEGLI STUDI DI PADOVA

**Dipartimento di Ingegneria Industriale DII**

Corso di Laurea Magistrale in Ingegneria Meccanica

**Analisi della risposta strutturale di una turbina  
idraulica: validazione di un modello semplificato  
sommerso**

Relatore:

Giovanna Cavazzini

Laureando:

Nicolò Martinelli 2053715

Anno Accademico 2022/2023



UNIVERSITÀ  
DEGLI STUDI  
DI PADOVA





## Abstract

Il presente progetto è incentrato sull'analisi della risposta dinamica di un disco rotante in aria e immerso in acqua. L'obiettivo principale è quello di creare un modello matematico in grado di riprodurre il comportamento della geometria reale nelle condizioni specificate. L'approccio è stato quello di utilizzare l'ambiente ANSYS WORKBENCH per eseguire diversi tipi di analisi modale, in aria, in acqua, con e senza rotazione, utilizzando gli strumenti di analisi modale e di analisi armonica. Il primo strumento serve a individuare i modi di vibrazione della struttura, ovvero le frequenze naturali e le forme di modo caratterizzate dall'orientamento delle linee nodali. Il secondo strumento è utilizzato per analizzare la risposta a un carico esterno applicato con un patch piezoelettrico eccitato con un segnale di tensione. Con questa simulazione, è possibile calcolare le deformazioni e gli sforzi indotti dalle frequenze naturali sul corpo.

In primo luogo, il modello è stato convalidato in aria, senza e con rotazione, per convalidare il modello attraverso il confronto con i risultati sperimentali. Quindi, è stato analizzato l'effetto della rotazione sulle frequenze naturali.

In secondo luogo, il disco immerso in acqua è stato studiato con una serie di simulazioni per analizzare l'effetto dell'acqua sulle frequenze naturali e sulle forme di modo. Per effettuare queste analisi, è stato necessario aggiungere un nuovo componente alla geometria, ovvero un serbatoio pieno d'acqua, e sviluppare un nuovo modello numerico basato sull'approccio acustico-strutturale della modellazione agli elementi finiti. Anche in questo caso, i risultati sono stati confrontati con quelli del laboratorio per la validazione con l'uso di una serie di analisi armoniche.

Va notato che per ottenere risultati ragionevoli con questi modelli, le condizioni al contorno per i cuscinetti e i materiali sono di particolare importanza e uno sforzo importante è stato dedicato all'ottenimento di risultati accurati.

Infine, dalle analisi effettuate e dal confronto con i risultati dei test, il modello è stato validato sia in aria che in acqua con una buona accuratezza; il modello è in grado di simulare sia l'effetto della presenza dell'acqua sulle frequenze naturali che l'effetto della rotazione sulle frequenze naturali.



## Abstract

The present project is focused on the analysis of the dynamic response of a rotating disk in air and submerged in water. The main objective is to create a mathematical model that can reproduce the behavior of the actual geometry in the specified conditions. The approach has been to use the *ANSYS WORKBENCH* environment to perform different types of modal analysis, in air, in water, with and without the rotation using the *modal analysis* and the *harmonic analysis* tools. The first tool is used to find out the modes of vibrations of the structure, or what is the same, the natural frequencies and the mode shapes characterized by the orientation of the nodal lines. The second tool is used to analyze the response to an external load applied with a piezoelectric patch excited with a voltage signal. With this simulation, it is possible to calculate the strains and deformations induced by the natural frequencies on the body.

Firstly, the model has been validated in the air without and with rotation to validate the model by comparison with experimental results. Then, the effect of the rotation on the natural frequencies has been analyzed.

Secondly, the disk submerged in water has been investigated with a series of simulations to analyze the effect of water on the natural frequencies and the mode shapes. To carry out these analyses, it has been necessary to add a new component to the geometry, which is a tank full of water, and to develop a new numerical model based on the acoustic-structural Finite Element Modelling approach. Again, the results have been compared with the ones of the laboratory for validation with the use of a series of harmonic analyses.

It must be noted that to obtain reasonable results with these models, the boundary conditions for bearings and the materials are of particular importance and an important effort has been devoted to obtaining accurate results.

Lastly, from the analysis performed and from the comparison with the test results the model is validated both in air and in water with good accuracy, the model can simulate both the effect of the presence of the water on the natural frequencies and the effect of the rotation on the natural frequencies.

## Acronyms

**AVMI:** added virtual mass incremental

**CAD:** computer-aided design

**E:** Young modulus [ $\text{N/m}^2$ ]

**FFT:** Fast Furier transformation

**FRF:** Frequency response function

**FRR:** frequency reduction ratio

**ND:** nodal diameter

**NC:** nodal circle

**P:** density

**SFR:** Strain frequency response

**SHM:** Structural Health Monitoring

**SG:** strain gauge

**SFR:** strain frequency response



# Sumari

<b>SUMARI</b>	<b>8</b>
<b>1. PREFACE</b>	<b>16</b>
<b>2. INTRODUCTION</b>	<b>17</b>
2.1. Objectives.....	18
2.2. Scope of the project.....	18
2.3. Methodology.....	19
<b>3. BASIC CONCEPTS</b>	<b>21</b>
3.1. Vibration .....	21
3.2. Mode shapes.....	23
3.3. The influence of the rotation on the vibration .....	25
3.4. The influence of the water on the vibration.....	26
3.4.1. Mathematical formulation .....	26
3.5. Dynamic response of the structure.....	30
3.5.1. Modal analysis .....	30
3.5.2. Harmonic analysis.....	34
<b>4. EXPERIMENTAL SETUP AND NUMERICAL MODEL</b>	<b>37</b>
4.1. Experimental setup.....	37
4.2. Model setup.....	44
4.2.1. Set up in the air .....	45
4.2.2. Set up in the water .....	49
<b>5. SIMULATION IN AIR</b>	<b>52</b>
5.1. Modal analysis simulation .....	54
5.2. Harmonic analysis validation.....	63
5.2.1. 1ND.....	64
5.2.2. 0NC.....	68
5.2.3. 2ND.....	72
5.2.4. 3ND.....	76
5.2.5. 4ND.....	80
5.2.6. Strain Frequency Response.....	84
5.3. Influence of the rotation .....	91
<b>6. SIMULATION IN WATER</b>	<b>95</b>
6.1.1. Modal acoustic.....	99
6.1.2. Harmonic analysis.....	101

<b>7. COMPARISON BETWEEN THE STRUCTURAL RESPONSE IN AIR AND WATER</b>	<b>103</b>
<b>8. PROJECT PLAN</b>	<b>112</b>
<b>9. BUDGET</b>	<b>113</b>
<b>10. ENVIRONMENTAL IMPACT</b>	<b>114</b>
<b>11. CONCLUSION</b>	<b>116</b>
<b>BIBLIOGRAFIA</b>	<b>118</b>
Referències bibliogràfiques:.....	118
<b>12. APPENDIX</b>	<b>122</b>
A CHARACTERISTIC OF THE PIEZOELECTRIC PATCH .....	122
A1 Piezoelectric effect.....	122
A.2 Piezoelectric patch P-876.A12hure .....	123
A.3 Piezoceramic material PIC255.....	125
B ANSYSIS.....	130
B.1 modal analysis .....	131
B.2 Harmonic analysis.....	133
B.3 Modal acoustic .....	135
B.4 Harmonic modal analysis.....	136
C LabVIEW .....	137
D. RESULTS OF THE HARMONIC ANALYSIS IN AIR .....	138
E. COORDINATE SYSTEMS FOR THE THREE SG.....	149
<b>ACKNOWLEDGMENTS</b>	<b>151</b>

## List of figures

<b>Figure 1</b> Frequency response graph with just one natural frequency .....	22
<b>Figure 2</b> Representation of node and anti-node for the 1ND. Image from [20] .....	24
<b>Figure 3</b> Nodal lines of composite mode shapes. Image from [20] .....	24
<b>Figure 4</b> Circular plate in contact with fluid. Image from [14] .....	26
<b>Figure 5</b> CAD scheme of the structure without the tank .....	38
<b>Figure 6</b> Complete structure in UPC's laboratory .....	38
<b>Figure 7</b> Sensors on the bottom of the disk .....	39
<b>Figure 8</b> Position of the bearings .....	40
<b>Figure 9</b> Duract transducer P-876.A12 design, geometry, and dimensions. Image from [10] .....	41
<b>Figure 10</b> Schematic of the section of a P-876.A12 patch Image from [10] .....	41
<b>Figure 11</b> Scheme and properties of the strain gauge "WFRA-3-11-1LDBB-F Image from [10] .....	42
<b>Figure 12</b> Properties of the epoxy resin material .....	42
<b>Figure 13</b> Construction of a piezoelectric accelerometer. Image from [5] .....	43
<b>Figure 14</b> Geometry of the structure built in CAD .....	44
<b>Figure 15</b> Sensors on the bottom of the disk in virtual geometry(right) and laboratory (left) .....	45
<b>Figure 16</b> Stiffness coefficients defined for the bearings .....	47
<b>Figure 17</b> quality of the mesh .....	48
<b>Figure 18</b> Illustration of the three directions of the SG2 .....	49
<b>Figure 19</b> New boundary conditions for the second bearings .....	49
<b>Figure 20</b> Comparison between mesh in water (left) and air (right) .....	51
<b>Figure 21</b> Virtual piezoelectric patch on the bottom of the disk .....	53
<b>Figure 22</b> On the left the torsional mode shapes, on the right the shaft bending .....	54
<b>Figure 23</b> The first seven mode shapes of the disk .....	54
<b>Figure 24</b> Representation of the nodal line (red line) of the +1ND on the left and -1ND on the right .....	56
<b>Figure 25</b> Representation of the nodal line of the ONC .....	56
<b>Figure 26</b> Representation of the nodal line of the -2ND on the left and +2ND on the right .....	57
<b>Figure 27</b> Representation of the nodal lines (red lines) of the +3ND on the left and -3ND on the right .....	57
<b>Figure 28</b> Representation of the nodal line (red circle) of the 1NC .....	57
<b>Figure 29</b> Representation of the nodal line (red line and red circle) of the +1ND-1NC on the left and -1ND+1NC on the right .....	58
<b>Figure 30</b> Strain obtained for Equivalent von mises on the left and Maximum principal on the right for 1ND (SG2) .....	64
<b>Figure 31</b> Comparison between the Normal elastic Strain for the three directions of SG2 for the 1ND .....	64
<b>Figure 32</b> Comparison between the Normal elastic Strain for the three directions of SG3 for the 1ND .....	65
<b>Figure 33</b> Comparison between the Normal elastic Strain for the three directions of SG4 for the 1ND .....	65
<b>Figure 34</b> Peak of the strain on the left and the normal strain on the right .....	66
<b>Figure 35</b> Strain obtained for Equivalent von mises on the right and Maximum principal on the left for ONC .....	68
<b>Figure 36</b> Comparison between the Normal elastic Strain for the three directions of SG2 for the ONC .....	68

<b>Figure 37</b> Comparison between the Normal elastic Strain for the three directions of SG3 for the ONC .....	69
<b>Figure 38</b> Comparison between the Normal elastic Strain for the three directions of SG4 for the ONC .....	69
<b>Figure 39</b> Peak of the strain on the left and the normal strain on the right.....	70
<b>Figure 40</b> Strain obtained for Equivalent von mises on the left and Maximum principal on the right for 2ND.....	72
<b>Figure 41</b> Comparison between the Normal elastic Strain for the three directions of SG2 for the 2 <sup>ND</sup> .....	72
<b>Figure 42</b> Comparison between the Normal elastic Strain for the three directions of SG3 for the 2ND.....	73
<b>Figure 43</b> Comparison between the Normal elastic Strain for the three directions of SG4 for the 2ND.....	73
<b>Figure 44</b> Peak in the strain frequency response on the top and normal strain along the orthogonal direction on the bottom.....	74
<b>Figure 45</b> Strain obtained for Equivalent von mises on the left and Maximum principal on the right for 3ND.....	76
<b>Figure 46</b> Comparison between the Normal elastic Strain for the three directions of SG2 for the 3ND.....	76
<b>Figure 47</b> Comparison between the Normal elastic Strain for the three directions of SG3 for the 3ND.....	77
<b>Figure 48</b> Comparison between the Normal elastic Strain for the three directions of SG4 for the 3ND.....	77
<b>Figure 49</b> Peak in the strain frequency response on the top and normal strain along the orthogonal direction on the bottom.....	78
<b>Figure 50</b> Strain obtained for Equivalent von mises on the left and Maximum principal on the right for 4ND.....	80
<b>Figure 51</b> Comparison between the Normal elastic Strain for the three directions of SG2 for the 4ND.....	80
<b>Figure 52</b> Comparison between the Normal elastic Strain for the three directions of SG3 for the 4ND.....	81
<b>Figure 53</b> Comparison between the Normal elastic Strain for the three directions of SG3 for the 4ND.....	81
<b>Figure 54</b> Peak in the strain frequency response on the top and normal strain along the orthogonal direction on the bottom.....	82
<b>Figure 55</b> FFT of the strain obtained from the chirp 0-100 Hz in air.....	85
<b>Figure 56</b> Strain gauges signal from laboratory and simulation for SG2 .....	86
<b>Figure 57</b> Strain gauges signal from laboratory and simulation for accelerometer .....	87
<b>Figure 58</b> Strain gauges signal from laboratory and simulation for SG3 .....	88
<b>Figure 59</b> Strain gauges signal from laboratory and simulation for accelerometer .....	88
<b>Figure 60</b> Strain gauges signal from laboratory and simulation for SG2 .....	89
<b>Figure 61</b> Strain gauges signal from laboratory and simulation for accelerometer .....	89
<b>Figure 62</b> Temporal signal of the accelerometer for 0 rpm, 100 rpm and 200 rpm.....	91
<b>Figure 63</b> Influence of the rotation on the frequency in the laboratory and simulation for the 1ND .....	92
<b>Figure 64</b> Influence of the rotation on the frequency in the laboratory and simulation for the 2ND .....	92
<b>Figure 65</b> Influence of the rotation on the frequency in the laboratory and simulation for the 3ND .....	93
<b>Figure 66</b> Influence of the rotation on the frequency in the laboratory and simulation for the 4ND .....	93
<b>Figure 67</b> FFT obtained for the SG8 (real geometry) in water .....	96
<b>Figure 68</b> FFT obtained for the accelerometer (real geometry) in water .....	97
<b>Figure 69</b> First seven mode shapes of the disk in water .....	99
<b>Figure 70</b> Trends of natural frequencies in water obtained in laboratory and simulation where 1ND is the 1, ONC is the number 2 and so on, the 1NC1ND is the last (number 7).....	100
<b>Figure 71</b> Peaks of the amplitude for the SG2 in the range of frequency 0-100Hz .....	101
<b>Figure 72</b> Peaks of the amplitude for the SG2 in the range of frequency 0-100Hz .....	102
<b>Figure 73</b> Comparison between the modal shape in the air on the top and water on the bottom .....	103

<b>Figure 74</b> Trend lines of the frequency in air and in water for the laboratory test .....	105
<b>Figure 75</b> Trend lines of the frequency in air and in water for the simulation test .....	105
<b>Figure 76</b> Trend of FRR for both simulation and test.....	106
<b>Figure 77</b> Comparison between the strain peaks in water and in air.....	111
<b>Figure 78</b> Strain-charge form representation of a piezoelectric material. Image from [30] .....	122
<b>Figure 79</b> Stress-charge form representation of a piezoelectric material. Image from [30].....	123
<b>Figure 80</b> Composition of the piezoelectric patch from PI Ceramic, as well as the polarization direction of each model. Image from [31].....	124
<b>Figure 81</b> Composition of the piezoelectric patch, as well as the polarization direction of each model. Image from [31].....	125
<b>Figure 82</b> Specific parameters of the standard materials. Imagine from: [32] .....	126
<b>Figure 83</b> Directions of forces affecting a piezoelectric element. Image from [34].....	129
<b>Figure 84</b> Workbench main page.....	130
<b>Figure 85</b> New interface obtained from the model section .....	131
<b>Figure 86</b> Sequence to obtain the mode shapes from a total deformation simulation.....	132
<b>Figure 87</b> Rotational velocity in modal analysis.....	132
<b>Figure 88</b> Coupling between modal and harmonic analysis .....	133
<b>Figure 89</b> Adding a piezoelectric body in harmonic analysis .....	133
<b>Figure 90</b> Adding a strain frequency response.....	134
<b>Figure 91</b> Sections of the modal acoustic analysis.....	135
<b>Figure 92</b> Definition of a Physic region in modal analysis.....	135
<b>Figure 93</b> Interface of LabVIEW.....	137
<b>Figure 94</b> Peak of 1ND in Strain Frequency Response .....	138
<b>Figure 95</b> Peak of amplitude of 1ND analyzed by the SG3 along three directions.....	138
<b>Figure 96</b> Peak of the amplitude of 1ND analyzed by the SG4 along three directions.....	139
<b>Figure 97</b> Peak of the amplitude of 0NC analyzed by the SG4 along three directions .....	139
<b>Figure 98</b> Peak of the amplitude of 0NC analyzed by the SG3 along three directions .....	140
<b>Figure 99</b> Peak of the amplitude of 0NC analyzed by the SG4 along three directions .....	140
<b>Figure 100</b> Peak of the amplitude of 2ND analyzed by the SG2 along three directions.....	141
<b>Figure 101</b> Peak of the amplitude of 2ND analyzed by the SG2 along three directions.....	141
<b>Figure 102</b> Peak of the amplitude of 2ND analyzed by the SG3 along three directions.....	142
<b>Figure 103</b> Peak of the amplitude of 3ND analyzed by the SG2 along three directions.....	142
<b>Figure 104</b> Peak of the amplitude of 3ND analyzed by the SG3 along three directions.....	143
<b>Figure 105</b> Peak of the amplitude of 3ND analyzed by the SG4 along three directions.....	143
<b>Figure 106</b> Peak of the amplitude of 4ND analyzed by the SG2 along three directions.....	144
<b>Figure 107</b> Peak of the amplitude of 4ND analyzed by the SG3 along three directions.....	144
<b>Figure 108</b> Peak of the amplitude of 4ND analyzed by the SG4 along three directions.....	145
<b>Figure 109</b> Strain gauges signal from laboratory and simulation for SG3 .....	145
<b>Figure 110</b> Strain gauges signal from laboratory and simulation for SG4 .....	146
<b>Figure 111</b> Strain gauges signal from laboratory and simulation for SG3 .....	146
<b>Figure 112</b> Strain gauges signal from laboratory and simulation for SG4 .....	147



<b>Figure 113</b> Peaks of the amplitude for the SG3 in the range of frequency 0-100Hz .....	147
<b>Figure 114</b> Peaks of the amplitude for the SG4 in the range of frequency 0-100Hz .....	148
<b>Figure 115</b> Peaks of the amplitude for the SG3 in the range of frequency 100-200Hz .....	148
<b>Figure 116</b> Illustration of the three directions of the SG2 .....	149
<b>Figure 117</b> Position of the SG3 on the bottom and the three directions of analysis .....	149
<b>Figure 118</b> Position of the sg4 on the top of the disk and the three directions of analysis .....	150

## List of Tables

<b>Table 1</b> Properties of the structural material.....	46
<b>Table 2</b> Properties of “Piezo” material created in ANSYS .....	46
<b>Table 3</b> Properties of “Soft Layer” material created in ANSYS.....	47
<b>Table 4</b> Comparison between the mesh quality for different element size .....	48
<b>Table 5</b> Properties of the structural material.....	50
<b>Table 6</b> Comparison between the mesh quality for different element sizes.....	50
<b>Table 7</b> Error between the frequency in the laboratory and simulation.....	55
<b>Table 8</b> Comparison between the laboratory’s nodal lines and the simulation’s nodal lines for the 1ND.....	59
<b>Table 9</b> Comparison between the laboratory’s nodal lines and the simulation’s nodal lines for the 0NC.....	59
<b>Table 10</b> Comparison between the laboratory’s nodal lines and the simulation’s nodal lines for the 2ND .....	60
<b>Table 11</b> Comparison between the laboratory’s nodal lines and the simulation’s nodal lines for the 3ND .....	60
<b>Table 12</b> Comparison between the laboratory’s nodal lines and the simulation’s nodal lines for the 4ND .....	61
<b>Table 13</b> Comparison between the laboratory’s nodal lines and the simulation’s nodal lines for the 1NC.....	61
<b>Table 14</b> Comparison between the laboratory’s nodal lines and the simulation’s nodal lines for the 1ND 1NC....	62
<b>Table 15</b> Comparison between maximum e minimum value obtained by the normal strain for the three directions of SG1, SG2, and SG3. ....	66
<b>Table 16</b> Comparison between maximum e minimum value obtained by the normal strain for the three directions of the SG1, SG2, and SG3. ....	70
<b>Table 17</b> Comparison between maximum e minimum value obtained by the normal strain for the three directions of SG1, SG2, and SG3. ....	74
<b>Table 18</b> Comparison between maximum e minimum value obtained by the normal strain for the three directions of the SG1, SG2, SG3. ....	78
<b>Table 19</b> Comparison between maximum e minimum value obtained by the normal strain for the three directions of the SG1, SG2, SG3. ....	82
<b>Table 20</b> Increasing the frequency from 0 rpm to 300 rpm.....	94
<b>Table 21</b> Comparison between the natural frequencies found in air (modal analysis) or with surrounding water (modal acoustic). ....	95
<b>Table 22</b> FRR from laboratory results between air and water.....	98
<b>Table 23</b> Comparison between the natural frequencies in laboratory and in simulation .....	100
<b>Table 24</b> Comparison between the frequency in air in water.....	104

<b>Table 25</b> Comparison between the water simulation's nodal lines (left) and air simulation's nodal lines (right) for the 1ND.....	107
<b>Table 26</b> Comparison between the water simulation's nodal lines (left) and air simulation's nodal lines (right) for the 0NC.....	107
<b>Table 27</b> Comparison between the water simulation's nodal lines (left) and air simulation's nodal lines (right) for the 2ND.....	108
<b>Table 28</b> Comparison between the water simulation's nodal lines (left) and air simulation's nodal lines (right) for the 3ND.....	108
<b>Table 29</b> Comparison between the water simulation's nodal lines (left) and air simulation's nodal lines (right) for the 4ND.....	109
<b>Table 30</b> Comparison between the water simulation's nodal lines (left) and air simulation's nodal lines (right) for the 1NC.....	109
<b>Table 31</b> Comparison between the water simulation's nodal lines (left) and air simulation's nodal lines (right) for the 1ND1NC.....	110
<b>Table 32</b> Gantt diagram representing the project plan.....	112
<b>Table 33</b> Total Budget of project.....	113



# 1. Preface

In this Project, experimental tests have been analyzed and mathematical models have been developed to analyze the behavior of a circular disk subject to harmonic stress. The purpose is to create a mathematical model that can describe the modes of vibration in air and water, stationary and rotate of this simple structure and in the future can be used for simulation of more complex structures, such as hydraulic turbines.

The project is part of the EU-funded AFC4Hydro project that is developing a structural health monitoring system (SHM) to analyze the operating conditions of turbines under both nominal and off-design conditions. The overall objective of the AFC4Hydro research project is to design, implement and validate a full-scale water turbine active flow system that permits to increase efficiency and reducing the dynamics loads on the structure at any off-design operating conditions and during transient operations. Specifically, the system will modify the draft tube flow field to mitigate or suppress the pressure fluctuations induced by the vortical flow which limits the operation of actual hydraulic machines. Special attention will be given to the flow instability leading to the formation of the vortex rope in the draft tube.

This project represents a part of the work developed in UPC, that is centered on the study of the dynamic behavior of a rotating and submerged structure built in the laboratory by the IFLUIDS's research group.

## 2. INTRODUCTION

Complex systems submerged in water, such as hydraulic turbines, are subject to extreme and continuous forces that produce vibration during transient and off-design operations, which produces a decrease in efficiency and lifetime, in particular, the off-design conditions in hydraulic turbines are different from a design point, which is the set of operating conditions at which the turbine was optimized for maximum efficiency and performance. As part of an EU-funded AFC4Hydro project, the IFLUID's research group from UPC has built a test rig in the laboratory with a rotating and submerged disk to investigate the dynamic response of that structure. On the disk are present different types of sensors and actuators that extract information.

The structure that is analyzed during this project is simple geometry, a disk, and is investigated its behavior during the vibrations at different frequencies, moreover, this project aims to create a model for matching the data collected during the experiments and to find out how the water changes the natural frequencies and the mode shapes. To identify the structure response, a piezoelectric patch has been used to create and excitation, to measure the deformations several strain gauges are present on the bottom of the disk, while to measure the acceleration is present an accelerometer on the edge of the disk.

The structure of the thesis considers the following steps the first part is concentrated on the investigation of the vibration in the air using the Ansys environment *modal analysis* and *harmonic analysis*, and the second part analyzes the vibrations in water using different Ansys tools that permit define a solid-fluid interface, those tools are *modal acoustic* and *harmonic acoustic*. After these simulations, there will be a chapter in which is presented a comparison between the results in air and water to investigate the effect of the water on the structural response of the disk. The last chapter is dedicated to summarizing the results obtained.

Lastly, to validate the model all the results of the simulation are compared with the experimental data obtained in air and water, in particular, the focus is on the comparison between the strain frequency response curves and the peaks of it in the laboratory and simulation, to observe the presence of the mode shapes in the air and to investigate the effect of the water on them. In addition, for the simulation in the air, it is present an analysis and comparison of the effect of a rotational velocity on the natural frequencies.

## **2.1. Objectives**

In the frame of the AFC4Hydro project which is developing a monitoring system (SHM) to analyze the structural response of turbines under both nominal and off-design conditions, the objective of this project is to simulate correctly the structural response of a simpler structure, in particular a disk, in air and submerged in water. To complete the analysis in air, the influence of the rotation will also be investigated.

To do it, first It is necessary to obtain a numerical model of the system that represents its dynamic behavior under the same operating conditions as in the laboratory. Then, this model must be validated using experimental data to ensure that it represents the dynamic behavior of the tests. For that, piezoelectric actuators will be used to excite the structure, and strain gauges will be used to measure its response. In the end, this numerical model will be used to analyze the behavior of the structure in water and rotation.

## **2.2. Scope of the project**

During this project, several fields will be covered, starting with the analysis of the experimental tests performed in UPC's laboratory, and continuing with the investigation of the best way to obtain and develop a numerical model to perform accurate and reliable numerical simulations. The results of the present work should serve to validate a more complex mathematical model to analyze the structure response of an actual hydraulic turbine in water and rotating.

The IFLUIDS research group has already built and validated the test ring, as well as the installation of the sensors on the bottom of the disk and the acquisition of the experimental data. These measurements will be used to validate the models developed during this project.

## 2.3. Methodology

The model of the disk is done numerically, simulating the structure and obtaining the different natural frequencies, the modal properties, and the frequency response function, which is the structural response measures over a frequency range containing several resonance frequencies. The methodology that is followed during the project is consistent with the tests performed in the laboratory, firstly the model is validated in the air without and with a rotational velocity, secondly, it is added a tank full of water, and the disk is submerged in the fluid, finally, the structural response of the disk is analyzed and validated. The steps followed are listed below:

- Define all the relevant physical properties of the real structure needed to build a simplified numerical model in ANSYS.
- Add the piezoelectric patch to simulate the excitation.
- Obtain numerically the dynamic response of the system in air and water.
- Obtain the natural frequency and the corresponding mode shapes of the structure in air and water.
- Obtain numerically the frequency response of the system in air and water.
- Determine the influence of a rotational velocity on the frequency and the mode shapes.
- Validate the models through the experimental results.





### 3. BASIC CONCEPTS

Structural vibrations are defined as continuous cyclic motions that can be measured and observed in a structure due to excitation. When the structure is subjected to external forces, it tends to vibrate naturally at certain frequencies, known as the natural frequencies of the structure. These natural frequencies are dependent on the mass and stiffness of the structure, as well as its geometry. Due to those natural frequencies, when a structure is subject to a cyclic force whose frequency is equal or nearly equal to its natural frequency, it occurs a phenomenon called resonance. This resonance phenomenon makes the structure vibrate with a larger amplitude than when the same cyclic force is applied at other frequencies, producing different motion patterns, which are known as structural mode shapes.

The natural frequency changes due to the presence of fluid and this problem are known as the fluid-structure interaction problem, the frequency at which the natural frequency shows up decreased in base at how much mass is added. This influence of the fluid is interesting, especially for applications where the structure is submerged, like hydraulic turbines.

#### 3.1. Vibration

Vibrations are defined as continuous cyclic motions and they can be experienced by any system, living or not, from a person walking in a park to a steel structure oscillating because of vibrating machinery. Based on the excitation applied to the system, it could experience either *periodic vibrations*, such as the oscillatory motion of a vibrating feeder used in a mine, or *random vibrations*, such as the cyclic motion of a vehicle traveling on a rough, bumpy road. Vibrations happen literally everywhere. Drilling, blasting, construction or demolition work, jackhammers, piledrivers, heavy loaders, turbines, blowers, generators, transformers, and transportation are all great examples of activities and equipment that generate significant vibration levels for anyone or anything standing in their vicinity. Each human and structure exhibit individual vibration properties that depend on their mass and stiffness and are typically characterized using the frequency of vibration. The latter, measured in Hertz (Hz), is simply the number of cycles per second. In the field of vibration engineering, these frequencies are called natural frequencies because they are inherent to the system, in some way, like their mass or shape.

When a structure is subject to a cyclic force whose frequency is equal or nearly equal to its natural frequency, they start presenting a very important phenomenon in engineering called resonance. This phenomenon makes the structure vibrate with a larger amplitude than when the same cyclic force is applied at other frequencies. Resonance may cause violent swaying motions and even catastrophic failure in poorly designed structures including bridges, buildings, trains, and airplanes.

In structures, a high level of vibration can cause cracks, loose bolts, heavy noise, or even failure.

Vibrations can be classified into two main categories: free vibrations and forced vibrations. Free vibrations occur when a system is set into motion by an initial disturbance and then continues to oscillate without the presence of an external force. Forced vibration occurs when an external force is continuously applied to a system resulting in a steady-state motion.

Regarding, the natural frequency, which is set by the properties of the system, the easiest way to find the natural frequency of a system is to give the system a quick excitation and a look how its responses. For a system with a single natural frequency, the response will be at that natural frequency, if the system has a single natural frequency, it will respond by vibrating in a complex motion that includes many natural frequencies. The response of a system to a different input of different frequencies is called *frequency response*. It measures how much a system multiplies the amplitude of a given input at different frequencies, to represent it as a *frequency response curve*. A frequency response curve is characterized by the frequency along the x-axis and the gain along the y-axis. **Figure 1** below shows the frequency response of a system with just one natural frequency [1].

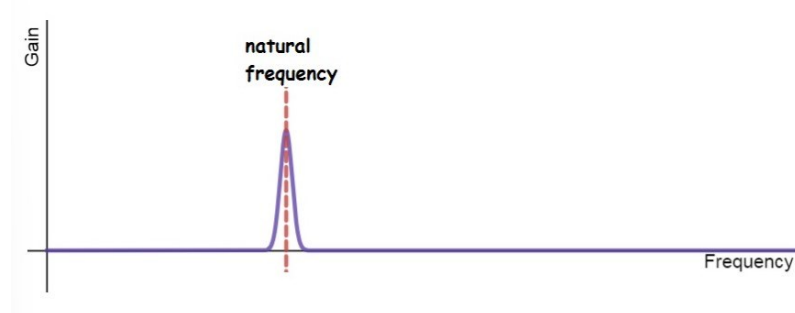


**Figure 1** Frequency response graph with just one natural frequency

When a structure reaches the natural frequency, it forms motion patterns called mode shapes, every mode shapes its characterized by zones with zero deformation and zones where the deformation is maximum. In a structure, in general, there are several mode shapes, higher is the number of the mode shape, and higher is the frequency at which it appears, and the more complex it will be.

To calculate the natural frequency the following formula is used:

$$f = \frac{\omega}{2\pi}$$

Where  $\omega$  is the angular frequency and it can be rewritten in the following way:

$$\omega = \sqrt{\frac{K}{m}} \quad 3.2$$

Where  $f$  is the natural frequency,  $k$  is the spring constant for the spring, and  $m$  is the mass of the ball.

To determine the mode shapes a modal analysis must be performed, in the general case with degrees of freedom the following equation is used:

$$[M]\{\ddot{u}\} + [C]\{\dot{u}\} + [K]\{u\} = \{f(t)\} \quad 3.3$$

Where  $M$  is the mass,  $C$  is the damping,  $K$  is the stiffness,  $\{\ddot{u}\}$  is the acceleration,  $\{\dot{u}\}$  is the velocity,  $\{u\}$  is the displacement, and  $f(t)$  is the load [2][3].

The steps to find the mode shapes are explained in chapter 3.5.1.

## 3.2. Mode shapes

When a structure reaches a natural frequency, it will vibrate in a mode shape. Mode shape, also known as natural mode or normal mode, is a pattern of vibration of a system when it is excited by an external force, it describes the shape and displacement of a system at a specific natural frequency of vibration. In mechanical systems, mode shapes are often represented graphically as displacement plots, showing the displacement of various points on the system as a function of time. It can also be represented mathematically as a set of coefficients that describe the amplitude and phase of the displacement at each point of the system. The number of mode shapes of a system has been determined by the number of degrees of freedom of the system. For example, a simple one-dimensional system such as a mass-spring system will have one mode shape, while a more complex three-dimensional system such as a building will have multiple mode shapes. It is important to note that the same system can have multiple mode shapes, each corresponding to a different natural frequency of vibration. The set of all mode shapes and the corresponding natural frequencies is called the system's modal pattern. In engineering and physics, mode shapes are important for predicting the behavior of a system under different loads, and for designing systems that are less susceptible to vibrations and resonances.

In the case of the project, the structure that is analyzed is a disk, the mode of a vibrating disk is determined by the numbers of NODE. A node is a place where the medium doesn't move opposed to

an anti-node which has maximum movement. There are two types of nodal lines for a disk, the diametric nodal lines or nodal diametric (ND) and the concentric nodal lines or nodal circle (NC), the first one is a line in space along which the displacement of the vibrating system is zero, the second one is a circle in which the displacement of the vibrating system is zero. The number of nodes defines the mode number, and each mode or pattern of vibration corresponds to a unique set of nodal lines or nodal circles, in addition, it is possible to have a composite mode, which is a combination of the two as it is shown in **Figure 3**. The position and the number of the nodal lines in a vibrating system can provide important information about the natural frequencies and mode of vibrations of the system, more nodal lines there are and higher the frequency will be [20].

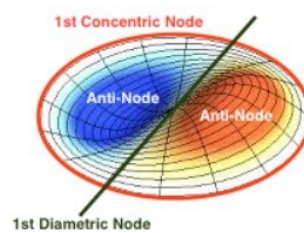


**Figure 2** Representation of node and anti-node for the 1ND. Image from [20]

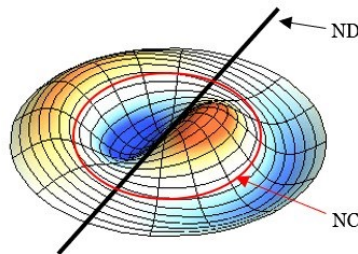


**Figure 3** Nodal lines of composite mode shapes. Image from [20]

### 3.3. The influence of the rotation on the vibration

A very interesting phenomenon is the influence of rotation on the vibrations of a structure, it has been studied hard in the last years due to its relevance in real engineering applications such as turbomachinery components.

The vibration of a non-rotating disk was fully discussed by Kirchhoff in two papers, and the other extreme where the disk is so thin and the rotation so rapid that the flexural forces are negligible, and the problem admits a simple solution. Regarding the rotation, the problem was analyzed by Lamb and Southwell [15][16][17].

The equation of the motion for the free transverse vibration of a rotating thin circular plate in space fixed coordinates is given by Wang:

$$D\nabla^4 w - \frac{h}{r} \left[ \frac{\partial}{\partial r} \left( \sigma^r r \frac{\partial w}{\partial r} \right) + \frac{\partial}{\partial \theta} \left( \sigma^\theta \frac{\partial w}{r \partial \theta} \right) \right] + \rho h \left[ \frac{\partial^2 w}{\partial t^2} \right] = 0 \quad 3.4$$

In this equation, the D is the bending stiffness of the plate, and it is defined in the following way:

$$D = \frac{Eh^3}{12(1-\nu^2)} \quad 3.5$$

There are other symbols to define  $\nabla^4$ , and  $\sigma^\theta(r, \Omega)$ ,  $\sigma^r(r, \Omega)$  that are stresses due to the centrifugal effect.

$$\sigma^r(r, \Omega) = \frac{3+\nu}{8} \rho \Omega^2 (a^2 - r^2) + \frac{\rho \Omega^2 b^2 (1-\nu^2) [a^2(3+\nu) - b^2(1+\nu)]}{8[b^2(1-\nu) + a^2(1+\nu)]} \left( \frac{a^2}{r^2} - 1 \right) \quad 3.6$$

$$\sigma^\theta(r, \Omega) = \frac{\rho \Omega^2}{8} [(3 + \nu)R^2 - (1 + 3\nu)r^2] - \frac{\rho \Omega^2 b^2 (1-\nu^2) [a^2(3+\nu) - b^2(1+\nu)]}{8[b^2(1-\nu) + a^2(1+\nu)]} \left( \frac{a^2}{r^2} - 1 \right) \quad 3.7$$

In those equations the  $w(r, \theta, t)$  denotes the transverse displacement concerning  $(r, \theta)$  frame,  $\rho$  is the density of the plate,  $\nu$  is the Poisson's ratio,  $\Omega$  is the angular speed of the plate and  $h$  is the thickness of the plate [6][7].

In the air and water, the rotation affects the natural frequencies of a vibrating system. In a system that is rotating at a constant angular velocity, the natural frequencies of the system will be shifted by an amount

proportional to the angular velocity. This is known as the centrifugal stiffening effect.

The results of the effect of the rotation are that the modal frequencies increase with a forward mode and decrease with a forward mode for all the modes due to the fact the rotation generates a centrifugal force field whose net effect is an apparent increase of the stiffness causing, in turn, an increase of the natural frequency with speed.

Moreover, in water, it is possible to observe the double modes phenomena for which for every mode shape there are two picks due to the asymmetry of the geometry, when the disk is rotating the center of these two peaks remains nearby constant and equal to the non-rotating case. The difference between them increases linearly with the rotating speed [8].

### 3.4. The influence of the water on the vibration

There are several applications with structures in fluid and it is important to know the effect of the water on the vibrations. It is well known that the natural frequencies of structures in a fluid are different from those in water due to the added virtual mass incremental (AVMI) that can be defined as the ratio between the Kinetic energy of the plate due to the motion of the plate over the kinetic energy of the circular plate itself.

#### 3.4.1. Mathematical formulation

To analyze the effect of a fluid over a structure a plate will be considered. Therefore, a circular plate is in contact with water and its dimensions are  $a$  (radius) and  $h$  (thickness) as is possible to see in **Figure 4**, moreover, it is defined as a Fluid domain  $F$ ,  $L_a$  is the surface between the fluid and the wall,  $L_b$  is the surface between the fluid and the plate and  $L_\infty$  is the surface at infinity [25][14].

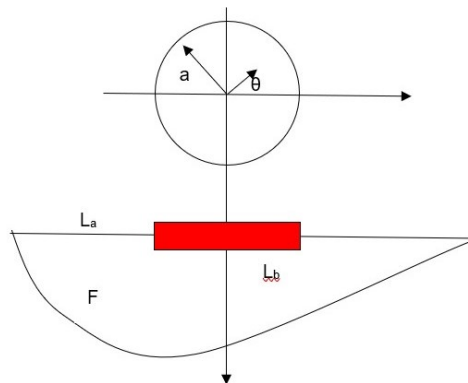


**Figure 4** Circular plate in contact with fluid. Image from [14]

The hypothesis on the fluid is that it is incompressible, inviscid, and irrotational, due to this last hypothesis there should be a velocity potential that can be represented throughout the following equation:

$$U(r,\theta,z,t)=\Phi(r,\theta,z)T(t)= \Phi(r,z)T(t) \quad 3. 8$$

The term  $\Phi(r,z)$  is the spatial velocity and it satisfies the Laplace equation in the domain F:

$$\nabla^2 \Phi = \frac{\partial^2 \Phi}{\partial r^2} + \frac{1}{r} \frac{\partial \Phi}{\partial r} + \frac{\partial^2 \Phi}{\partial z^2} \quad 3. 9$$

Adopting the infinitely rigid wall condition, that was adopted by Lamb and McLachlan, it is possible to write on  $L_a$ :

$$\frac{\partial \Phi(r,z)}{\partial z} = 0 \quad 3. 10$$

Furthermore, it is necessary to consider the interaction between the plate and the fluid. This condition can be present throughout the following equation, which is defined *on*  $L_b$ :

$$\frac{\partial \Phi(r,z)}{\partial n} = -W(r) \quad 3. 11$$

In this equation, the term  $W(r)$  is the mode shape of the plate vibrating in contact with the fluid.

Now, the radiation condition requires an attenuation of the disturbance when that distance from the plate becomes large. This condition implies the following effects on  $L_\infty$ :

$$\Phi, \frac{\partial \Phi}{\partial r}, \frac{\partial \Phi}{\partial z} \rightarrow 0 \text{ as } r, z \rightarrow \infty \quad 3. 12$$

All the boundary conditions are defined, to find the added virtual mass incremental factor (AVMI factor) it is necessary to start using Rayleigh's quotient:

$$f_a^2 \alpha \left( \frac{V_p}{T_p^*} \right)_{air} \quad and \quad f_l^2 \alpha \left( \frac{V_p}{T_p^*} + T_l^* \right)_{liquid} \quad 3. 13$$

The terms in the equations are  $f_a$  is the natural frequency of the plate,  $f_l$  is the natural frequency of the plate in contact with the fluid,  $T_p^*$  and  $V_p$  are respectively the reference Kinetic energy and the maximum potential energy of the plate,  $T_l^*$  is the reference Kinetic energy of the fluid due to the plate's movement.

It is possible to define a relation between reference and maximum kinetic energies in which  $\omega$  is the frequency in rad/s:

$$T_{max} = T^* \omega^2 \quad 3. 14$$

It is possible to obtain a relation from equation (3. 6) that draws a relationship between  $f_a$  and  $f_l$ , based on the assumption that the dynamic loading of the fluid as no effect on mode shapes.

$$f_l = \frac{f_a}{\sqrt{1+\beta}} \quad 3. 15$$

The term  $\beta$  is the AVMI, and, how it is possible to notice it defines a ratio of the kinetic energy of the plate due to the motion of the plate over the kinetic energy of the circular plate itself.

It can be defined in another way:

$$\beta = \frac{T_l^*}{T_p^*} \quad 3. 16$$

In conclusion, the natural frequency value of a body submerged in a fluid is lower than in the water due to the added mass ( $M_a$ ) and the AVMI can be expressed as the added mass over the modal mass:

$$\beta = \frac{M_a}{M} = \left( \frac{f_a}{f_l} \right)^2 - 1 \quad 3. 17$$



Where:

$$f_l = \frac{1}{2\pi} \sqrt{\frac{K}{M+M_a}} \quad \text{and} \quad f_a = \frac{1}{2\pi} \sqrt{\frac{K}{M}} \quad 3. 18$$

Where K is the spring constant

As it possible to ascertain from the equation

$$f_l = \frac{1}{2\pi} \sqrt{\frac{K}{M+M_a}} \quad \text{and} \quad f_a = 12\pi KM \quad 3. 18$$

The presence of water has a significant impact on the vibration of a system. In general, the addition of water to a system can increase its mass, which can result in a decrease in the natural frequencies of the system. When a system is submerged in water, it experiences added mass effect due to the water, which leads to a reduction in the natural frequencies of the system.

The presence of water can have a significant effect on the damping of the vibrations in a system, in fact when a structure is submerged in water, the water can act as a damper due to the viscous drag forces it exerts on the system. This can increase the damping ratio which can decrease the amplitude and decay rate of the vibrations.

### 3.5. Dynamic response of the structure

This chapter has described the equations used to investigate the mode shapes and the strain frequency response of a general structure, in particular, it will describe how to perform a modal analysis and a harmonic analysis.

#### 3.5.1. Modal analysis

First of all, it is important to determine the dynamic characteristics of the model and the vibration characteristics of the structure, such as natural frequencies, damping, mode shapes, the dynamic properties. The way to investigate those properties is the modal analysis which is a process whereby a structure is described in terms of its natural characteristics.

#### Governing equations of Modal Analysis in ANSYS

Modal analysis is a linear dynamics analysis, based on the general equation of motion, for solving the dynamic response of a structure. In the equation, the unknowns are acceleration, velocity, and displacement for all points over the structure.

$$[M]\{\ddot{u}\} + [C]\{\dot{u}\} + [K]\{u\} = \{f(t)\} \quad 3. 19$$

Where **M** is the mass, **C** is the damping, **K** is the stiffness,  $\ddot{u}$  is the acceleration,  $\dot{u}$  is the velocity,  $u$  is the displacement, and  $f(t)$  is the load. To simplify the equation is possible to do some assumptions, in particular, the external force is forced to be 0 and the damping effects are ignored. This is possible to do because natural frequencies and mode shapes are independent of loads. The matrix form of the equation used in ANSYS is represented by the equation 6. 2 where the unknowns are the acceleration vector  $\{\ddot{u}\}$  and the displacement vector  $\{u\}$ , to describe the motion of the free and undamped system are used only the mass matrix of the structure  $[M]$  and the stiffness matrix  $[K]$ .

$$[M]\{\ddot{u}\} + [K]\{u\} = 0 \quad 3. 20$$

Assuming that every point of the structure is withstanding a harmonic motion  $I$ , that equation is solved

as a frequency domain problem explained by an amplitude  $\{\Phi\}_i$ , an angular frequency  $\omega_i$ , and a phase angle  $\theta_i$ . It is possible to define the displacement and the acceleration with the following equations, where the acceleration is the second derivate of the displacement:

$$\{u\} = \{\Phi\}_i \sin(\omega_i t + \theta_i) \quad 3. 21$$

$$\{\ddot{u}\} = -\omega_i^2 \{\Phi\}_i \sin(\omega_i t + \theta_i) \quad 3. 22$$

To obtain the angular frequency  $\omega_i$ , called eigenvalue, and the mode shapes  $\Phi_i$ , called eigenvector, it is necessary to substitute the equations (3. 21) and (3. 20) into the equation (3. 18) to obtain the (3. 21), the typical eigenvalue problem solved by the Modal analysis of ANSYS:

$$([K] - \omega_i^2 [M]) \{\Phi\}_i = \{0\} \quad 3. 23$$

To obtain the frequency  $f_i$  for every desired mode  $i$ , it is necessary to use the equation (3. 22) once obtained  $\Phi_i$  and  $\omega_i$ :

$$f_i = \frac{\omega_i}{2\pi} = \frac{1}{2\pi} \sqrt{\frac{K}{M}} \quad 3. 24$$

These equations are used by Ansys to perform the simulation, in addition, to investigating vibrational modes, strain is also analyzed using three different analyses are used *equivalent (van-mises) Strain*, *Principal elastic strain*, *Normal elastic strain*, and *frequency response*.

Strain and stress are closely related properties of materials that describe how they deform and respond to applied forces. Strain is a measure of the deformation of a material in response to the applied force. It is usually expressed as a fraction or percentage of the original length of the material. Stress, on other hand, is a measure of the internal forces within a material caused by an applied force. It is usually expressed in units of forces per unit area. The equations used for this analysis are explained in the following part remembering that the relationship between stress and strain is given by Hooke's law, which states that the strain in a material is proportional to the stress applied to it, within the elastic limit of the material. Mathematically, it is represented as:

$$\text{Stress} = E \cdot \text{Strain}$$

3. 25

Where E is Young's modulus, the relationship is valid only for materials that are in the elastic range, when a material is under stress and strain, when it is under the elastic limit, and when the material returns to its original shape after the stress is removed.

### Equivalent (von-mises) Strain

To evaluate the strain using the equivalent Strain the software starts from the information that each material point has a strain state which is represented by a strain tensor, that has nine components, [22].

$$\begin{matrix} \varepsilon_{xx} & \varepsilon_{xy} & \varepsilon_{xz} \\ \varepsilon_{yx} & \varepsilon_{yy} & \varepsilon_{yz} \\ \varepsilon_{zx} & \varepsilon_{zy} & \varepsilon_{zz} \end{matrix} \quad \text{strain tensor}$$

From this tensor is possible to calculate the equivalent strain using the following equation:

$$\varepsilon_{equivalent} = \left( \frac{1}{1+\nu} \right) \sqrt{\frac{(\varepsilon_{xx}-\varepsilon_{yy})^2 + (\varepsilon_{yy}-\varepsilon_{zz})^2 + (\varepsilon_{zz}-\varepsilon_{xx})^2 + 6(\varepsilon_{xy}^2 + \varepsilon_{yz}^2 + \varepsilon_{zx}^2)}{2}} \quad 3. 26$$

The problem with this way is that the equivalent strain does not represent the complete information of the strain state.

### Maximum principal strain

Looking at the strain tensor, the nine values are not absolute, with a different coordinate system, the values are different, but they still can represent the same stress status.

The principal stresses are the component of the tensor when the shear stress components are zero, [23].

$$\begin{matrix} \varepsilon_1 & 0 & 0 \\ 0 & \varepsilon_2 & 0 \\ 0 & 0 & \varepsilon_3 \end{matrix}$$

## Normal principal

Normal strain is a term that describes the response of a solid to the application of a force. The strain can be defined by the equation below:

$$\varepsilon = \frac{\Delta L}{L} \quad 3. 27$$

The normal principal strain is defined along a specific direction, in Ansys is necessary to define an axis of a coordinate system to obtain the result.

Where  $\varepsilon$  is the normal strain,  $\Delta L$  is the change in length and  $L$  is the original length.

### 3.5.2. Harmonic analysis

As aforementioned, structures are subject to resonance, which can lead to structural problems due to excessive motion, stress, noise, vibrations, fatigue damage, and potential failure due to the cyclically repeating load. To analyze the response of the structure under a steady-state sinusoidal harmonic load excited at a given frequency, harmonic analysis is performed. This harmonic analysis will give an idea of the strain amplitude measured at each natural frequency obtained from the modal analysis.

In the harmonic analysis, there can be multiple loadings, but all are sinusoidal, and the excitation and response are steady-state oscillatory behavior.

#### Governing equation of the harmonic analysis

The most relevant assumptions made in an ANSYS harmonic analysis are that the entire structure has a constant or frequency-dependent stiffness, damping, and mass effects and that all loads and displacements vary sinusoidally at the same known frequency (but they can be in a different phase).

The general equation of motion, for solving the dynamic response of a structure. In the equation, the unknowns are acceleration, velocity, and displacement for all points over the structure.

$$[M]\{\ddot{u}\} + [C]\{\dot{u}\} + [K]\{u\} = \{F\} \quad 3. 28$$

where  $\{u\}$ ,  $\{\dot{u}\}$ ,  $\{\ddot{u}\}$  are the vectors of nodal displacement, velocity, and acceleration of the  $n$  discretized points in the time domain, respectively.  $[M]$  is the structural mass matrix,  $[C]$  is the structural damping matrix of the system,  $[K]$  is the stiffness matrix, and  $\{F\}$  is the force vector that expresses the force applied on each point in the time domain, which varies sinusoidally at a given frequency  $\Omega$ .

All the points in the structure are assumed to be oscillating at the same frequency, so the complex force and displacement vector can be defined as the sinusoidal signal of equation (3. 28), as a function of time  $t$  and a circular frequency  $\Omega$ :

$$\{F\} = F_{\max} e^{i\psi} e^{i\Omega t} = F_{\max} (\cos \psi + i \sin \psi) e^{i\Omega t} = (\{F_1\} + i\{F_2\}) e^{i\Omega t} \quad 3. 29$$

$$\{u\} = u_{\max} e^{i\psi} e^{i\Omega t} = u_{\max} (\cos \phi + i \sin \phi) e^{i\Omega t} = (\{u_1\} + i\{u_2\}) e^{i\Omega t} \quad 3. 30$$

where  $\Omega$  is the excitation frequency at which the loading occurs,  $\psi$  is the force phase shift that may be present if different loads are excited at different phases and  $\varphi$  is the displacement phase shift that may exist if damping or a force phase shift is present.

By substituting the expressions of equations (3. 29 and 3. 30) into the general equation of motion of (3. 28), and differentiating the displacements to get velocity and acceleration, it can be obtained the harmonic equation of motion:

$$(-\Omega^2[\mathbf{M}] + i\Omega[\mathbf{C}] + [\mathbf{K}])(\{u_1\} + i\{u_2\}) = (\{F_1\} + i\{F_2\}) \quad 3. 31$$

where  $\{u_1\} = \{u_{\max} \cos \varphi\}$  is the real displacement vector,  $\{u_2\} = \{u_{\max} \sin \varphi\}$  is the imaginary displacement vector,  $\{F_1\} = \{F_{\max} \cos \psi\}$  is the real force vector and  $\{F_2\} = \{F_{\max} \sin \psi\}$  is the imaginary force vector.

ANSYS has two ways of solving the harmonic equation of motion (3. 31), depending on the solution method selected, which can be either the Mode Superposition Method or the Full Method. The Mode Superposition Method solves the harmonic equation in modal coordinates, as shown in equation (3.32), where all the displacements are uncoupled and can be expressed as a linear combination of the mode shapes  $\phi_j$ .

$$y_j'' + 2\omega_j \xi_j y_j' + \omega_j^2 y_j = f_j \quad 3. 32$$

Therefore, it is first needed to perform a modal analysis to determine these mode shapes  $\phi_j$  and their corresponding natural frequency  $\omega_j$ . For each mode  $j$  it can also be extracted the modal coordinate  $y_j$  (together with its acceleration  $y_j''$  and velocity  $y_j'$ ), the fraction of critical damping  $\xi_j$ , and the force applied in modal coordinates  $f_j$ . However, the solution obtained is approximate, and it does not fully support nonzero displacements.

On the other hand, the Full Method solves the matrix equation (3. 31) directly in nodal coordinates, which is analogous to linear static analysis, except that complex numbers are used. Although this method is more computationally expensive, it computes an exact solution and supports all types of loads including nonzero displacements, including the possibility to define the voltage on each face of the piezoelectric element. Hence, a Full Method is used for solving the harmonic analysis, which does not rely on mode shapes information and natural frequency.

In addition, when is present a fluid the equation that must be considered is the following one:

$$[M + M_F]\{\ddot{u}\} + [C + C_F]\{\dot{u}\} + [K + K_F]\{u\} = \{F\} \quad 3. 33$$

Where is considered the effect of the added mass  $[M_F]$ , the damping effect of the fluid  $[C_F]$ , and the  $[K_F]$ .

The solution of the equation (3. 33) leads to modes shapes, natural frequencies, and damping ratio of the fluid-structure system. The equation used for calculating the frequencies is the following one that considers the added mass ( $M_F$ ), it is clear that the mass decreases the natural frequencies of the system submerged in water compared with the ones obtained in the air [33]:

$$f_i = \frac{1}{2\pi} \sqrt{\frac{K}{M + M_F}} \quad 3. 34$$



## 4. EXPERIMENTAL SETUP AND NUMERICAL MODEL

The following chapters are explained how is settled the experimental test and the numerical model. Firstly, it will be described how are the architecture of the structure and all the sensors present in the experimental test. Secondly, it will be described how the model in ANSYS has been created to match the experimental results, it will be described the geometry compared with the one in the experiments, the properties of the materials, the boundary conditions, and the quality of the mesh, moreover, in water and air it is necessary to define different boundary conditions even if the structure is the same.

### 4.1. Experimental setup

The simple structure that will be analyzed can rotate and be submerged in water, its purpose is to be part of the (SHM) system to analyze the condition and performance of turbines during steady and transient conditions.

The system considered in this project is a rotating structure built up in the laboratory of UPC, the structure is composed of a disk, a shaft, two bearings, a motor for the rotation, a tank that is added only for the test in water and several sensors to obtain the data. Regarding the sensors, there is one accelerometer at the edge of the disk, a piezoelectric patch for exciting the disk, and three strain gauges. The dimensions in mm of the shaft joined to the disk are illustrated in **Figure 5**, while **Figure 6** shows the laboratory of UPC with all the structures, it is possible to observe the motor for the rotation, the position of the two bearings, and the presence of the tank.

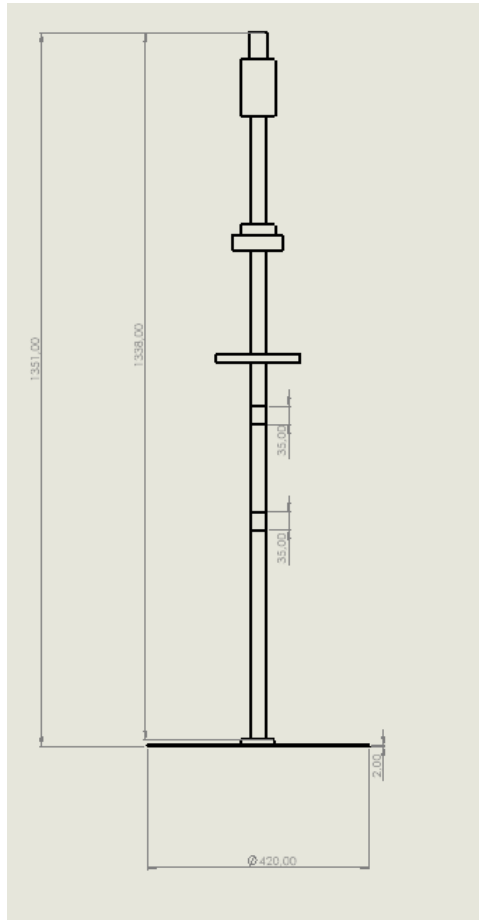


**Figure 5** CAD scheme of the structure without the tank



**Figure 6** Complete structure in UPC's laboratory

As aforementioned, the test rig is also equipped with systems to generate mechanical and fluid-dynamic excitations, together with measuring systems to check the deformation and vibration of the structure. The additional elements used in the disk are piezoelectric transducers, working as actuators, strain gauges, and an accelerometer, all the sensors are on the bottom of the disk as shown in **Figure 7**, in fact, on the top, there are no sensors.

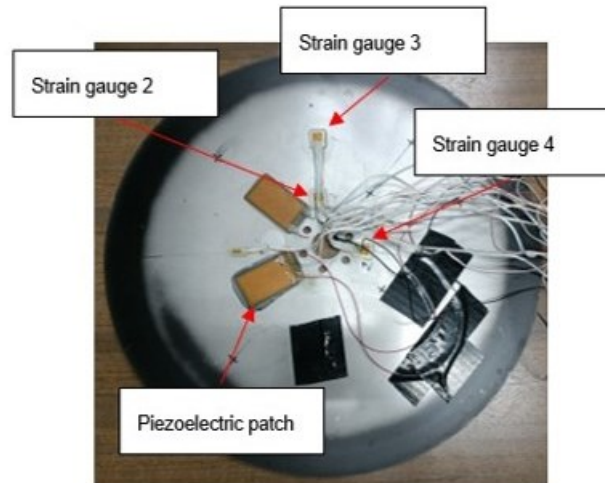


**Figure 7** Sensors on the bottom of the disk

To perform the analysis in water it is necessary to add a tank that is a cylinder of plexiglass with an internal diameter of 488mm and a height of 600mm. The disk is a thin circular plate of 420mm in diameter and a thickness of 2mm. The shaft that supports the disk has a length of 1350mm and it has two bearings of 35 mm in height each one, which enables the support of the shaft, and the structure of the test rig and allows the rotation of the structure. Finally, of great importance is the position of the bearings which is shown in **Figure 8**.

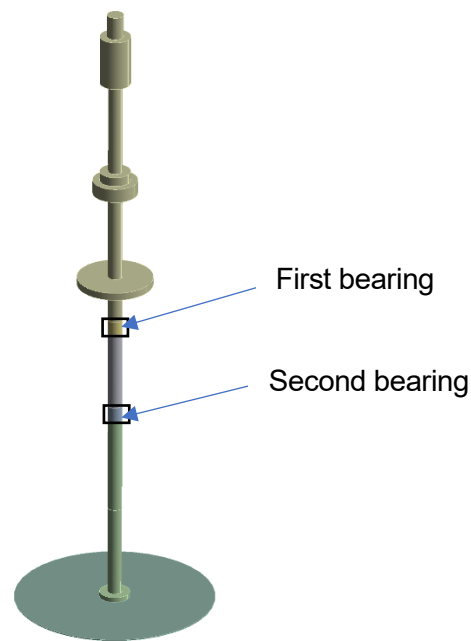


**Figure 8** Position of the bearings

During the water test, the disk is submerged 200mm inside the tank of water, so depending on the depth of the disk inside the water the relative position of the bearings will change accordingly, as well as the depth of the disk inside the tank. The coupling between the shaft and the disk is done using a set of bolts that are directly screwed to the shaft from the bottom of the disk. Therefore, instead of considering the complex geometry made of several bolts used in the real structure, the geometry is simplified considering that all the threads of the bolts form a cylinder of 63.60 mm in diameter and 11 mm in height.

The test rig is also equipped with systems to generate mechanical and fluid-dynamic excitations, together with measuring systems to check the deformation and vibration of the structure. As it is needed to collect the data from sensors in real-time, the disk and the shaft have a through a hole with a slip ring on the top of the shaft to allow the transmission of the power and electrical signals from the stationary data receiver device to the rotating structure of the disk. The additional elements used in the disk are piezoelectric transducers, working as actuators, and different sensors such as strain gauges, lasers, accelerometers, pressure sensors, and fiber optics.

The piezoelectric transducer used in the system is bonded to the disk surface using a water-resistant epoxy adhesive. The piezoelectric transducer used in the test rig is the P-876.A12, it is composed of a PIC255 active layer sandwiched between two soft, thin encapsulating polymer materials, together with Modelling and control of the vibration of a rotatory disk p. 23 two electrodes, as presented in **Figure 9**. This polymer coating serves as electrical insulation for the active layer and is used to apply prestress to

the active layer to avoid cracks, which increases the allowable curvature radius of the PZT ceramics. The overall dimensions of the P-876.A12 transducer (including the encapsulating material) are 61 mm x 35 mm x 0.5 mm, while the encapsulated active piezoceramic layer is 50 mm x 30 mm x 0.2 mm.

**Figure 9** it is shown the drawing of the P-876.A12 patch with the dimensions in mm, together with the tolerances provided by the manufacturer [10].

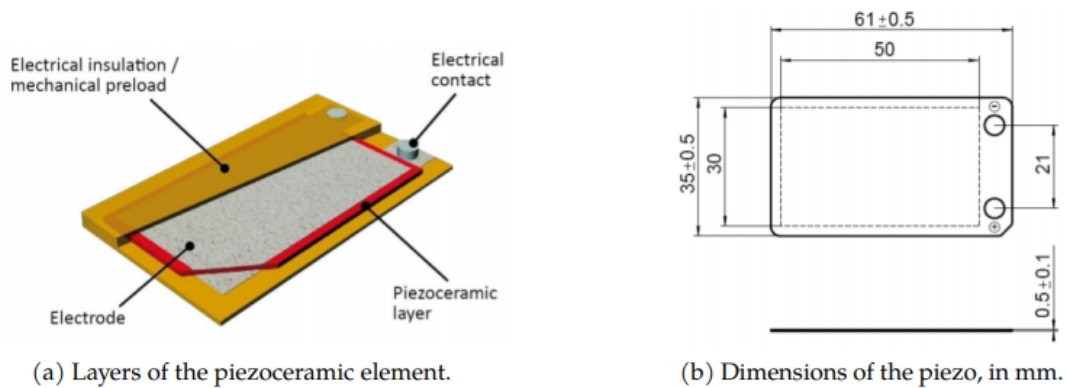


**Figure 9** Duract transducer P-876.A12 design, geometry, and dimensions. Image from [10]

The piezoelectric patch is composed of 5 sections Figure 9, considering also the glue with a thickness of 0,2 mm approximately. Starting from the top the first material is Kapton, which is a suitable coating material due to its good bonding properties and electrical insulation, it permits the patch to be submerged in water. The total thickness of the Kapton layer is 0,3 mm, there are two Kapton layers because it surrounds the active layer, which has a thickness of 0.2 mm. The combination of the bottom Kapton layer and the glue forms a soft layer between the active layer and the disk.

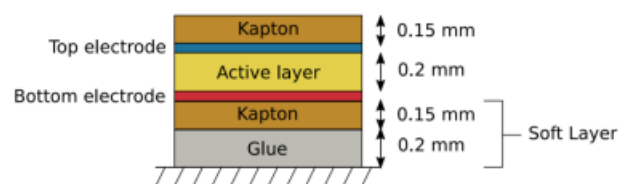


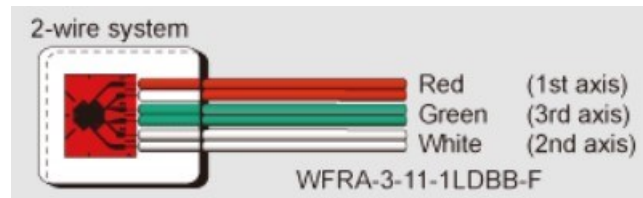
**Figure 10** Schematic of the section of a P-876.A12 patch Image from [10]

In addition to the piezoelectric patch strain gauges are used to measure the strain external forces applied to the disk cause a deformation. The strain gauges change in electric resistance proportionally to the deformation of the disk, measuring the strain means measuring changes in the electrical resistance.

On the disk are installed different strain gauges from Tokyo Measuring Instruments Lab (WF-series) [1]

with 1 and 3 axes on the bottom and the top of the disk, but only the 3 axes are used during this project.

This WF-series of strain gauges present a vinyl lead wire with an entire transparent coating of epoxy resin that ensures electrical insulation of the grid (Cu-Ni) and an easy installation of the gauge. In **Figure 11** a scheme and the properties of the “WFRA-3-11-1LDBB-F” with three axes are shown.



Type	Gauge		Backing			Resistance ( $\Omega$ )	Lead wire pre- attached	Type name of lead wire preattached
	length (mm)	width (mm)	length (mm)	width (mm)	thickness (mm)			
WFRA-3-11	3	1.7	19	16	1.5	120	Paralleled 1m	
WFRA-3-17							Paralleled 3m	-1LDBB
WFRA-3-23							Paralleled 5m	-3LDBB
							3-wire 3m	-5LDBB
							3-wire 5m	-3LDBTB
								-5LDBTB

**Figure 11** Scheme and properties of the strain gauge “WFRA-3-11-1LDBB-F” Image from [10]

The name indicates the property of being waterproof, the dimensions of the three strain gauges are 3mm in the length and 1.7mm in the width. The main body is protected from the water with an epoxy resin whose properties are illustrated in **Figure 12**, it has a length of 19mm, a width of 16mm, and a thickness of 1.5mm. To analyze the strain is necessary to know the resistance of the strain, in this case, it is 120  $\Omega$ .

Density	$\rho = 1100 \text{ kg/m}^3$
Young's Modulus	$Y = 4.3 \times 10^9 \text{ Pa}$
Poisson's Ratio	$\nu = 0.2$

**Figure 12** Properties of the epoxy resin material

The last sensor on the bottom of the disk is an accelerometer, which is a device used to measure acceleration or change in velocity. It can measure acceleration in one, two, or three directions depending

on the type of accelerometer, and it is commonly used to measure vibrations and motion in mechanical systems, such as machinery, vehicles, buildings, and bridges. There are several types of accelerometers: piezoelectric, capacitive, and MEMS. The type of use is the piezoelectric accelerometer SN LW333029 which uses the piezoelectric effect to convert mechanical motion into an electrical signal. A piezoelectric accelerometer consists of a piezoelectric element, typically a quartz crystal or ceramic material, that is attached to a mass. The mass is suspended on a spring, so when the accelerometer is subjected to acceleration, the mass moves and applies stress to the piezoelectric element generating an electrical charge [4]. The electrical charge generated by the piezoelectric element is proportional to the acceleration experienced by the accelerometer. This charge can be amplified and converted into a voltage, which can be measured and used to determine the acceleration of the accelerometer.

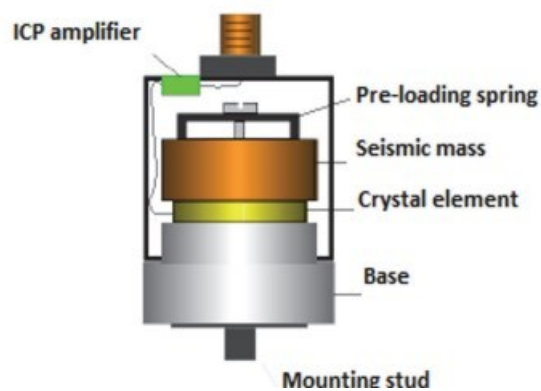


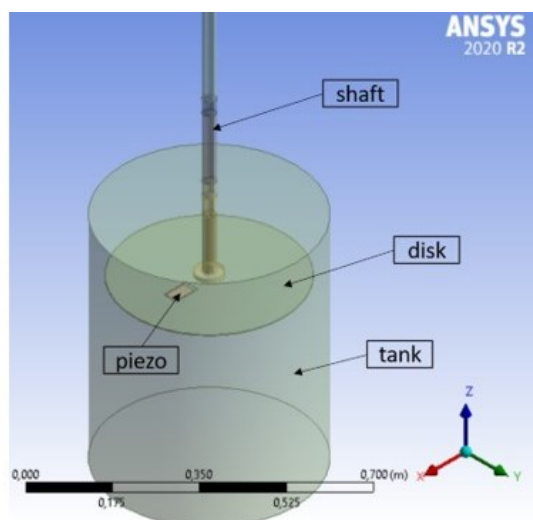
**Figure 13** Construction of a piezoelectric accelerometer. Image from [5]

## 4.2. Model setup

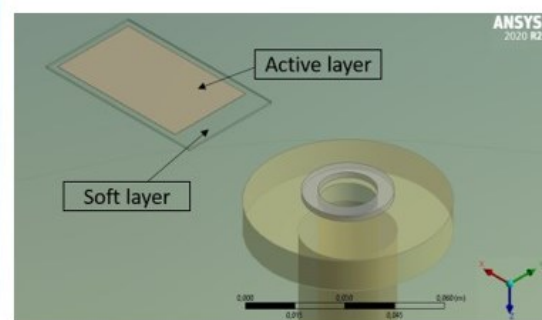
Regarding the model setup due to the different boundary conditions that are present in the air and water, there are different setups for the model in the air and water, but even if the conditions are different the structure is the same both for air and water, except for the presence of a tank full of water in the model in water.

Regarding the geometry, it was created using *Solidworks* and then imported into *Design modeler*, which is an application of ANSYS's workbench. It provides several modeling functions that include parametric geometry creation, concept model creation, and several custom tools designed for fluid flow, structural and other types of analysis. This geometry, used for Modal analysis, harmonic analysis, modal acoustic, and harmonica acoustic, is composed of a disk, a piezoelectric patch, a shaft, and a tank full of water.

The real geometry is different from the virtual geometry because it was necessary to simplify the computations and avoid extra computational burden in solving the system, therefore, the bearings that support the disk are not considered but they will be recreated using boundary conditions, and all the nuts and the bolts used for mechanical coupling between the shaft and the disk. To represent all these components around the disk using a cylinder around the shaft to simulate the volume occupied.



(a) Geometry of the system created in ANSYS.



(b) Closeup piezo geometry

**Figure 14** Geometry of the structure built in CAD

To obtain the same results in the laboratory it is mandatory to place the sensor in the same position as the laboratory setup. Starting from the patch the first sensor on the edge of the disk is the accelerometer which is  $15^\circ$  from the patch, the next ones are the strain gauges 2 and 3 whose position is  $125^\circ$  from the



patch and 5,5 cm from each other, the last sensor is located at 50° from the SG2 and SG3, on the top of the disk there are no sensors.

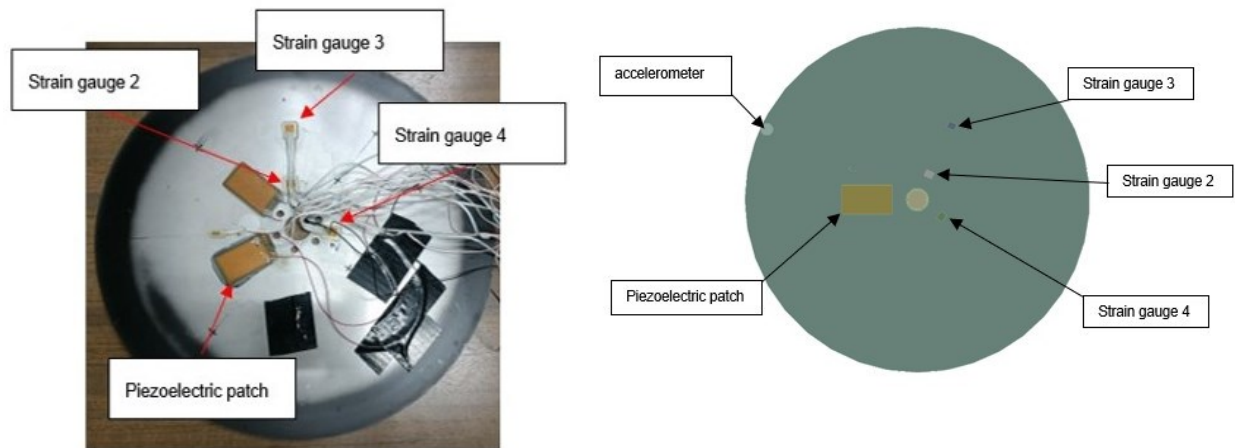


**Figure 15** Sensors on the bottom of the disk in virtual geometry(right) and laboratory (left)

Once obtained the geometry of the structure and the sensors, it is possible to perform further steps, modal analysis, harmonic analysis, modal acoustic, and harmonic acoustic.

#### 4.2.1. Set up in the air

The first step of the setup is to define the properties of the material; it is possible to define it from the section “Engineering Data” in the *workbench*. The system analyzed involved three different materials, one for the disk and two for the piezoelectric patch that is composed of an active and passive layer.

Firstly, the disk is composed of Stainless Steel, in this block of ANSYS it is possible to define and change the properties of the material or eventually add new material. Regarding the properties, the most important are the density, Young’s modulus, and Poisson’s ratio. The properties used for the main body of the structure are illustrated in **Table 1**.

P (density)	7900 Kg/m <sup>3</sup>
E (Young's modulus)	2,1*10 <sup>11</sup> Pa
N (Poisson's ratio)	0,3

**Table 1** Properties of the structural material

Secondly, on the bottom of the disk is present a sensor that can excite the structure, this component is a piezoelectric material. The one used is the commercial piezoelectric patch P-876.A12. The piezoelectric patch is composed of an active layer and a passive layer. The active layer is composed of a soft piezoelectric ceramic material PIC255, which is an orthogonal crystallographic system that involves the interaction between the electrical and mechanical behavior of the material. This piezoelectric ceramic material is not included in the “workbench library”, therefore It needed to create a new material using the properties that are given by the manufacturers. Once the properties were obtained, it can be possible to create a new “Piezo” material in the “engineering data” using the orthotropic linear elastic constants summarized in **Table 2** below.

Density	$\rho = 7.8 \text{ g/cm}^3$
Young's Modulus X direction	$Y_{11} = 6.2112 \times 10^{10} \text{ Pa}$
Young's Modulus Y direction	$Y_{22} = 6.2112 \times 10^{10} \text{ Pa}$
Young's Modulus Z direction	$Y_{33} = 4.8309 \times 10^{10} \text{ Pa}$
Poisson's Ratio XY	$\nu_{12} = 0.3608$
Poisson's Ratio YZ	$\nu_{23} = 0.45$
Poisson's Ratio XZ	$\nu_{13} = 0.45$
Shear Modulus XY	$G_{12} = 2.282 \times 10^{10} \text{ Pa}$
Shear Modulus YZ	$G_{23} = 2.231 \times 10^{10} \text{ Pa}$
Shear Modulus XZ	$G_{13} = 2.231 \times 10^{10} \text{ Pa}$

**Table 2** Properties of “Piezo” material created in ANSYS

Regarding the passive layer which surrounds the active layer, it is responsible for pasting the active layer to the disk and protecting it. It is composed of epoxy glue and the Kapton shell used respectively to attach the patch to the disk and to cover the active layer. The mechanical properties of the epoxy glue and the Kapton shell are presented in **Table 3** and they were added as a new material in the “workbench library”.

Density	$\rho=1420 \text{ Kg/m}^3$
Young's Modulus	$E= 2.8 \cdot 10^9 \text{ Pa}$
Poisson's Ratio	$V=0,3$

**Table 3** Properties of “Soft Layer” material created in ANSYS

All the materials are defined and inserted in the Ansys library, the next step is to define the boundary condition of the bearing. The fastest way would be to create two fixed bearings but it would not recreate the reality, in fact, this type of boundary conditions don't permit any movement of the shaft where the bearings are located, thus it is necessary to define a bushing joint condition that permits to fix a stiffness. Fixing a stiffness brings the model closer to reality by allowing relative movement between bearings and shaft. The value of the stiffness coefficients in the different directions is shown in **Figure 16**. The coefficients are the same for the two bearings that are located in two different positions, as it is possible to see in **Figure 8**.

Stiffness	Per Unit X (m)	Per Unit Y (m)	Per Unit Z (m)	Per Unit $\theta_x$ (°)	Per Unit $\theta_y$ (°)	Per Unit $\theta_z$ (°)
$\Delta$ Force X (N)	1000,					
$\Delta$ Force Y (N)	0,	100,				
$\Delta$ Force Z (N)	0,	0,	100,			
$\Delta$ Moment X (N·m)	0,	0,	0,	100,		
$\Delta$ Moment Y (N·m)	0,	0,	0,	0,	100,	
$\Delta$ Moment Z (N·m)	0,	0,	0,	0,	0,	100,

**Figure 16** Stiffness coefficients defined for the bearings

After the definition of the stiffness coefficients, the following step is to create a good mesh that must have good accuracy, more elements of the mesh are present, and more accuracy will have the result, but also more time steps will be necessary. Regarding this, for choosing the right dimension the time step for different dimensions is analyzed. In the following **Table 4** the different values of the mode shapes for different qualities of the mesh are listed.

SIZE [mm]	1ND	0NC	2ND	3ND	4ND	SOLUTION TIME [s]
0,01	38,341	60,761	70,453	142,95	250,7	14
0,008	37,762	58,366	68,464	141,49	247,17	18
0,005	37,445	57,141	67,249	140,79	246,58	24
0,004	37,348	56,811	66,964	140,55	245,82	35

**Table 4** Comparison between the mesh quality for different element size

From the table is possible to notice that from 0,01 mm to 0,005 mm there is a huge increase in the quality of the mesh while the rise of the time is constant, from 0,005 to 0,004 the increase in mesh quality is not as significant as in previous cases even though time has a greater increase. For those reasons the size of the mesh selected is 0,005 mm. The numbers of an element obtained are 43826 and 88796.

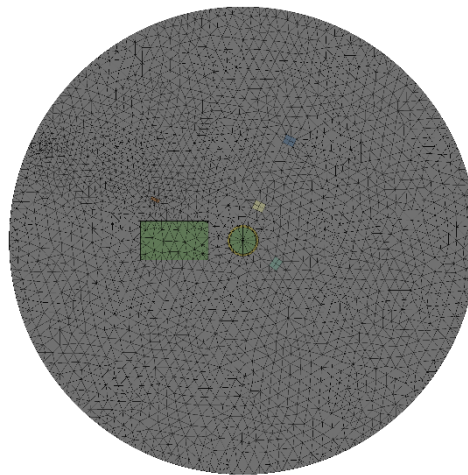


**Figure 17** quality of the mesh

In conclusion, every strain gauge analyses the strain in three different directions: a radial direction ( $0^\circ$ ) and two directions at  $45^\circ$  and  $-45^\circ$  concerning the radial direction. To obtain the same behavior three coordinate systems must be defined for every strain gauge so that it is possible to analyze the strain

along a specific direction, in **Figure 18** it is shown the coordinate systems for SG2, in appendix [E] are presented all the coordinate systems.

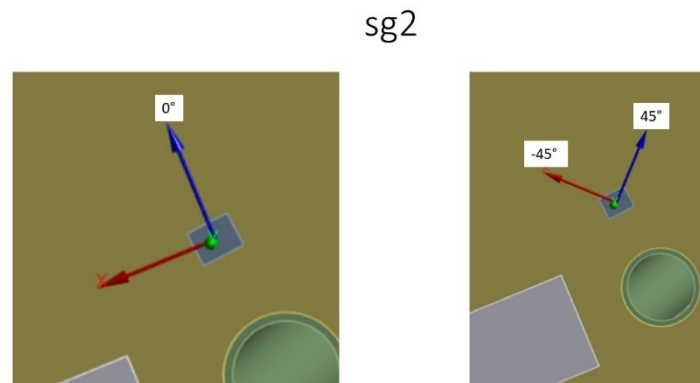


**Figure 18** Illustration of the three directions of the SG2

#### 4.2.2. Set up in the water

In water, the structure and the sensors are the same as in air, but it is characterized by the presence of a fluid, in particular a tank full of water, it is possible to add it from the program SOLIDWORKS. The main difference with the water test is that during the installation of the tank, the position of the bearing with respect to the disk is changed probably, this fact implies the need to set new boundary conditions for the bearing and the material to obtain the same frequencies and the same mode shape. Looking at **Figure 8** is fixed a bushing joint condition with the stiffness coefficients illustrated in **Figure 19** for the second bearing, while the first bearing has a fixed joint condition without a stiffness coefficient.

**Stiffness Coefficients**

Stiffness	Per Unit X (m)	Per Unit Y (m)	Per Unit Z (m)	Per Unit $\theta_x$ (°)	Per Unit $\theta_y$ (°)	Per Unit $\theta_z$ (°)
$\Delta$ Force X (N)	1000,					
$\Delta$ Force Y (N)	0,	0,				
$\Delta$ Force Z (N)	0,	0,	100,			
$\Delta$ Moment X (N·m)	0,	0,	0,	100,		
$\Delta$ Moment Y (N·m)	0,	0,	0,	0,	100,	
$\Delta$ Moment Z (N·m)	0,	0,	0,	0,	0,	100,

**Figure 19** New boundary conditions for the second bearings

The natural frequencies are affected by the E of the material, so other to the boundary conditions of the bearings varied the E of the material. The new properties are illustrated in the following table.

P (density)	7900 Kg/m <sup>3</sup>
E (Young's modulus)	1,5*10 <sup>11</sup> Pa
N (Poisson's ratio)	0,3

**Table 5** Properties of the structural material

The simulation in water is more complex than in air which means that the mesh calls for greater accuracy. The method used to choose the size of the mesh is the same as in air, the results are summarized in **Table 6**.

Element size [m]	1ND	0NC	2ND	3ND	4ND	Solution time (min)
0,006	13,320	13,500	24,730	56,300	150,350	7,58
0,005	13,100	13,230	24,5	56,050	105,140	9,31
0,004	12,919	13,023	24,29	55,839	104,94	14,5
0,003	12,700	12,900	24,15	55,670	104,780	35,4
0,0025						Too much time >90

**Table 6** Comparison between the mesh quality for different element sizes

As in air with the decrease of the size the quality and the time increase. In this case, the choice is to use the 0,004 mm, which is lower than in air, because after that the time step starts to increase exponentially and for 0,0025 mm the time step is more than 90 minutes, the numbers of elements obtained are 508426 with 844641 nodes, the presence of the tank increases significantly the numbers of element respect to the air mesh.

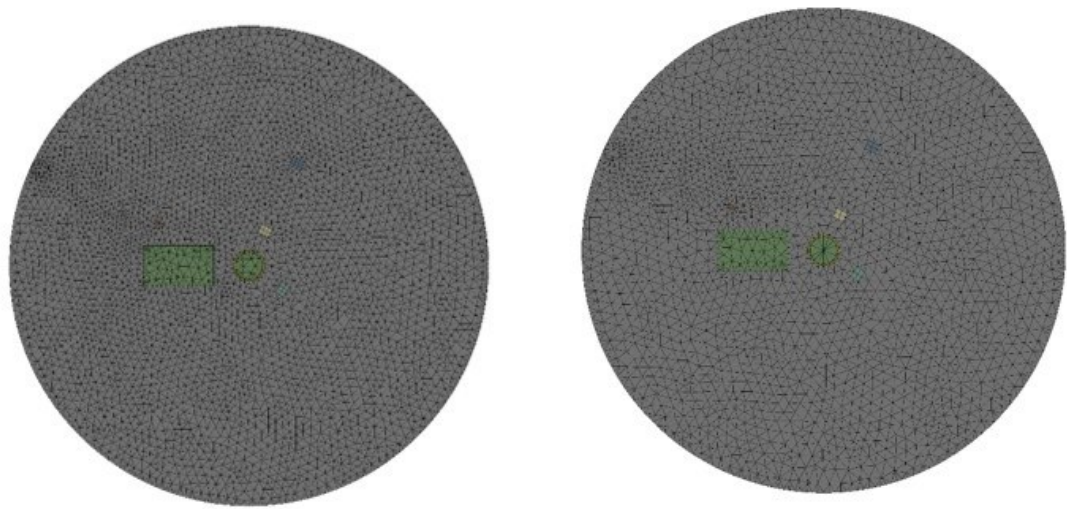


**Figure 20** Comparison between mesh in water (left) and air (right)

The rest of the conditions are the same as in the air.

## 5. SIMULATION IN AIR

The structure that is studied is composed of a disk connected to a shaft using bolts, the shaft is fixed to a supporting structure by two bearings. A motor is coupled to the shaft to rotate the disk at different speeds. The first part of the experiment is carried out in the air.

Moreover, some sensors have been attached to the top of the disk: a piezoelectric, three strain gauges, and an accelerometer. Regarding the piezoelectric patch, it is possible to induce an excitation to the disk by changing the voltage applied to the electrodes. The voltage produces a deformation to the patch and, due to the fact that the patch is glued to the disk, mechanical stress is transmitted to the disk. Secondly, the strain gauges have the purpose to analyze the strain along three specific directions, the signal obtained is different from an accelerometer that analyzes the acceleration of the disk along the orthogonal direction.

In order to model numerically the response of the disk in air, it is needed to use the program ANSYS Workbench performs a Finite Element Analysis (FEA) to calculate the mechanical behavior in terms of strain and deformation of the disk, moreover, because ANSYS does not have a package for piezoelectric analysis, it is necessary to add an extension which contains information about the material properties of the piezoelectric material. The extension is called "**Piezo and MEMS**" and it is used to provide compatibilities into ANSYS.

The goal is to match the results obtained in the laboratory with the results of the simulation. The chapter is structured so to follow the steps of the laboratory's analysis. Firstly, the fluid is air, and the simulation is focused on the research of the mode shapes in modal analysis. Here the goal is to fix the boundary conditions to find the mode shapes at the right frequencies. Secondly, a harmonic analysis is performed to analyze the pick of the strain response, to close the analysis in the air it is fundamental to add a rotational velocity and to study its influence on the mode shapes.

The first part is focused on fixing the boundary condition to investigate the vibration characteristics of the structure, such as natural frequencies, damping and mode shapes, and the dynamic properties using the modal analysis environment in ANSYS. To perform the simulation of the model in the air it is necessary to obtain the mode shapes with their respective frequencies and the FRF to compare the with the laboratory results.

Firstly, to get these results it is necessary to import the geometry inside the ANSYS and define the material, for the shaft and the disk the material is used in a STAINLESS STEEL, for the patch, there are two different materials: a piezoelectric material for the active part and a soft layer for the passive layer, all the materials properties are described in the chapter 4.2.1. Regarding the boundary conditions, it is



necessary to define a stiffness for the bearing, while the loads such as the piezoelectric patch are all set to 0 because they do not influence the mode shapes inside the modal analysis, as it is possible to observe in the equation 4.2 . All the boundary conditions used in the air are illustrated in chapter 4.2.1.

For the harmonic analysis, there are the same boundary conditions as in the modal analysis, but with the presence of an external load produced by the piezoelectric patch. Regarding the excitation induced by the piezoelectric patch, the voltage set is 400V for the positive layer and -100V for the negative layer, the virtual geometry of the piezoelectric patch is illustrated in **Figure 21**. The boundary conditions are the same for the bearings, in addition, a damping control of 0,02 is stetted inside the *ANALYSIS SETTING*.

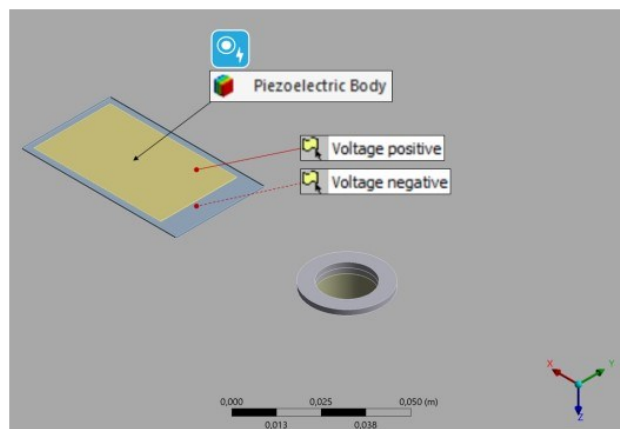


**Figure 21** Virtual piezoelectric patch on the bottom of the disk

## 5.1. Modal analysis simulation

From the modal analysis, the natural frequencies shown in **Figure 23** are obtained using equation 3.18. The simulation is focused on the structural response of the disk and not on the shaft, because of that in this project are represented only the mode shapes linked with the vibration of the disk, in fact, the mode shapes produced by the bending of the shaft and by the torsion are not visible in the figure, to be clearer the torsional mode shape and the shaft bending are shown in **Figure 22**.

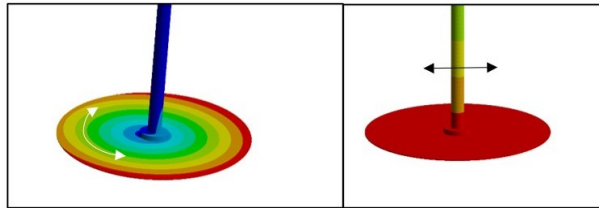


**Figure 22** On the left the torsional mode shapes, on the right the shaft bending

Moreover, every mode shapes have an equal mode shape only rotated by a certain angle; this could be traced back to the phenomenon called “**double modes**”. Regarding these double modes, all the asymmetric modes ( $n \neq 0$ ) are expected to have a double eigenvalue, corresponding to two orthogonal eigenvectors with identical mode shapes but with angularity shift of  $\frac{\pi}{2n}$ , the difference in the natural frequency between a pair of asymmetric modes is generally small [42], thus to simplify the analysis it will be treated like one mode using a mean value because due to a slight asymmetry of the disk does not have the same value. As it is possible to observe in the picture below there are 7 mode shapes, the labels assigned to each mode shapes consider the number of nodal diameter (ND) and nodal circle (NC). ND and NC refer to the straight or circumferential lines where the displacement of the disk structure remains at zero during the vibration cycle of a mode shape, corresponding to the blue zones of the

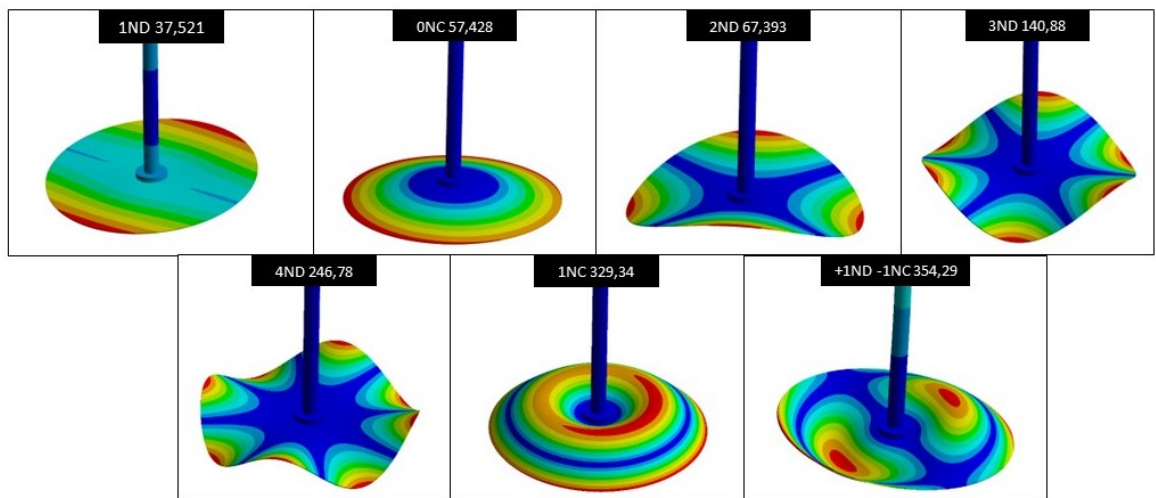


**Figure 23** The first seven mode shapes of the disk

deformed mode shape of the figure, the red color represents the maximum deformation of the disk [29].

There are more mode shapes at higher frequencies especially mix mode shapes, but to simplify the treatment are not analyzed in this simulation.

To summarize, seven mode shapes are represented, the nodal diameters are **1ND**, **2ND**, **3ND**, and **4ND**, the nodal circles are the **0NC** and the **1NC**, and lastly, there is a mode shape that is a mix between the nodal diameter and the nodal circle, and it is the **+1ND-1NC**.

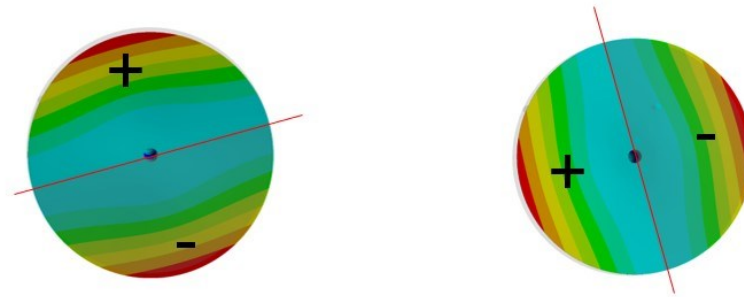
The following **Table 7** shows the mode shapes frequencies obtained in modal analysis and the ones obtained in the laboratory with the respective errors. As possible to notice all ND modes are well detected with errors under 5,5%, instead for the NC the errors are 28,02% for the 0NC and 15,87% for the 1NC. This difference between the ND's error and the NC's error could be linked to the complex behavior of the disk that it is not influenced only by the disk but also by all the components of the supporting structure such as bearings and bolts.

Mode shape	air simulation [Hz]	air laboratory [Hz]	error [%]
1ND	37,5	39,82	5,83
0NC	57,3	41,24	28,02
2ND	67,3	69,12	2,63
3ND	140,78	147,06	4,27
4ND	246,2	246,47	0,11
1NC	329,34	277,05	15,88
1NC1ND	354,29	292,27	17,51

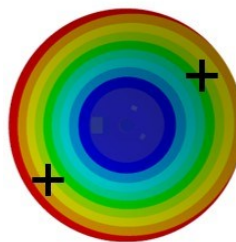
**Table 7** Error between the frequency in the laboratory and simulation

As aforementioned modal frequencies occur in pairs with the same values, but even if they have the same value the angular position of the nodal lines changes. The first seven mode shapes are illustrated in the figures below. The first mode shape is represented in **Figure 24** it is characterized by the presence of a nodal line of a nodal diameter through which the relative phase of displacement changes by about 180°, the symbols (+) and (–) indicate the position of the antinode concerning the zero-deformation position. As it is possible to notice the +1ND and the -1ND present the same mode shape but rotated, the maximum deformation is located at the edge of the disk, the red zone, while along the nodal line,

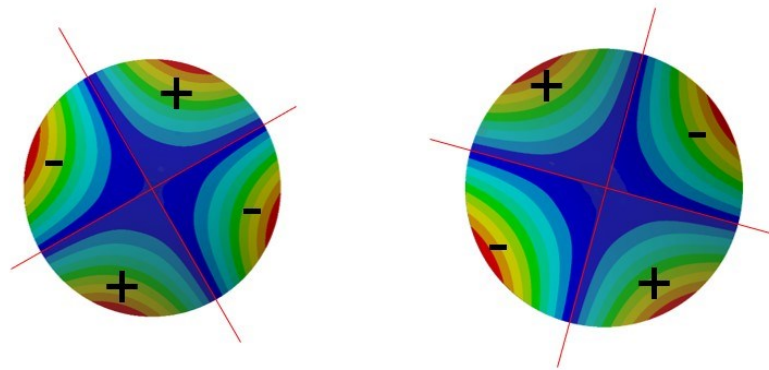
there is no deformation. **Figure 25** represents the mode shape 0NC, it is characterized by the presence of a nodal point in the center of the disk where it is fixed to the shaft, and the movement of the rest of the disk is in phase. The mode shape +2ND and -2ND present four zones of maximum that are always located on the periphery of the disk, those four points of maximum curvature have a  $90^\circ$  phase displacement. Moreover, there are two nodal lines placed at  $90^\circ$  to each other, **Figure 26**. Regarding the number of nodal lines, as expected, the number of them increases with the increase of the value of frequency of the natural frequency. Continuing with the analysis of the figures there is the 3ND in **Figure 27**, in this mode, there are six points of maximum curvature on the circumference of the disk. The next mode, illustrated in **Figure 28**, presents a nodal ring. The regions of maximum deformation are composed of two circular rings. The last mode shape, **Figure 29** is a mix of a nodal circular and a nodal diameter, this mix gives life to a complex deformation in which is possible to find a nodal ring and a nodal line.



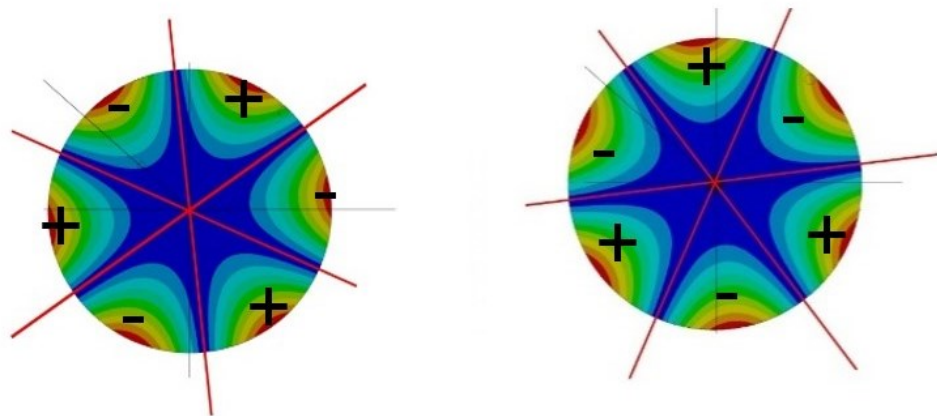
**Figure 24** Representation of the nodal line (red line) of the +1ND on the left and -1ND on the right



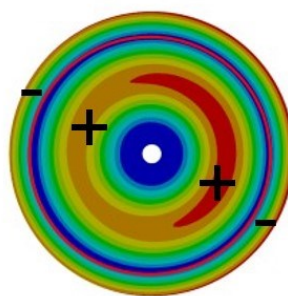
**Figure 25** Representation of the nodal line of the 0NC



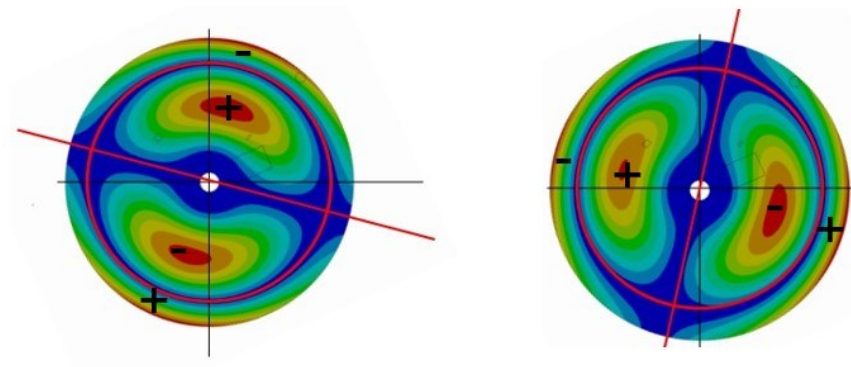
**Figure 26** Representation of the nodal line of the -2ND on the left and +2ND on the right



**Figure 27** Representation of the nodal lines (red lines) of the +3ND on the left and -3ND on the right

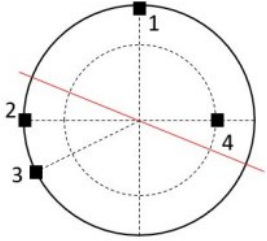
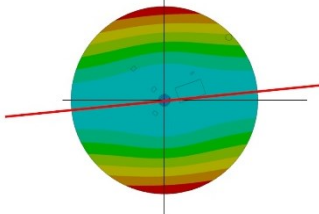
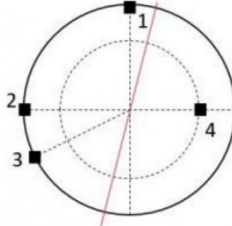
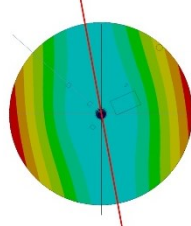


**Figure 28** Representation of the nodal line (red circle) of the 1NC

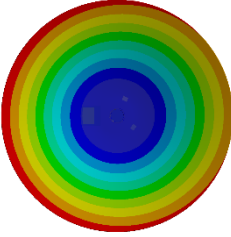


**Figure 29** Representation of the nodal line (red line and red circle) of the +1ND-1NC on the left and -1ND+1NC on the right

For concluding the validation of the modal analysis, it is fundamental to compare the value of the frequency and the direction of the mode shapes with the ones obtained in the laboratory. In the following tables, the nodal lines found in the laboratory and simulation are compared. In this case, the double modes are compared except for the 2ND. The 0NC is not analyzed because its NC is a point in the center of the disk. In the figures below, the blue zones have zero deformation, and they are the nodal lines zone highlighted by a red line, instead, the red zones have maximum deformation and for that, they represent the anti-node zone.

+1ND	
	
-1ND	
	

**Table 8** Comparison between the laboratory’s nodal lines and the simulation’s nodal lines for the 1ND

0NC	
Not available	

**Table 9** Comparison between the laboratory’s nodal lines and the simulation’s nodal lines for the 0NC

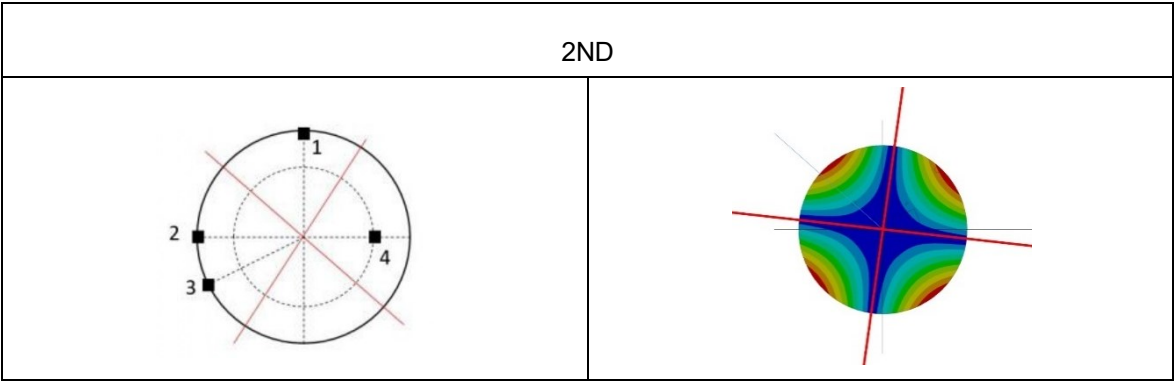


**Table 10** Comparison between the laboratory's nodal lines and the simulation's nodal lines for the 2ND

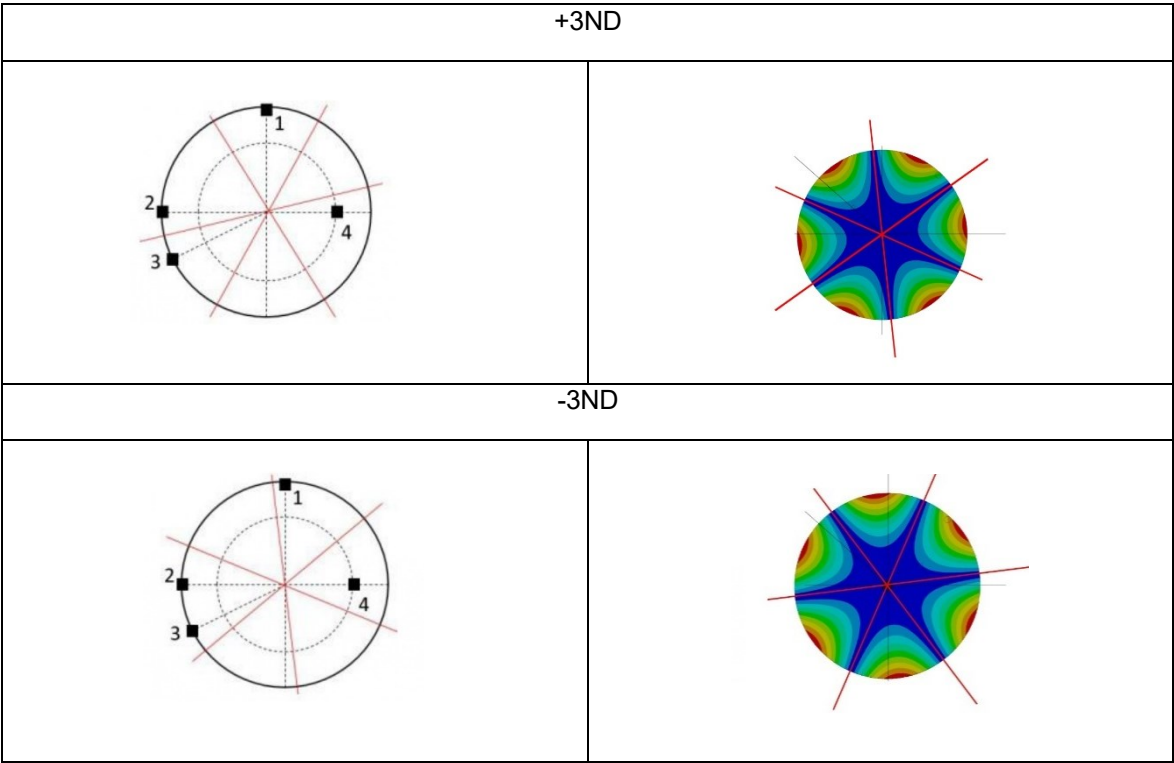


**Table 11** Comparison between the laboratory's nodal lines and the simulation's nodal lines for the 3ND



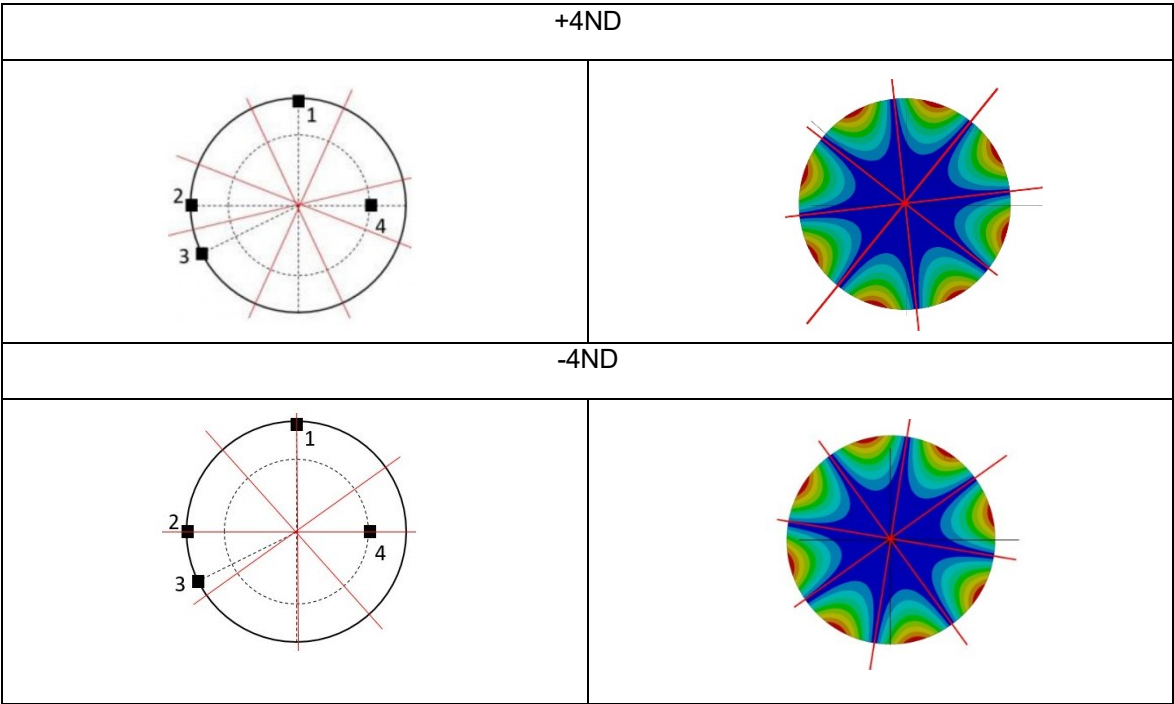


**Table 12** Comparison between the laboratory's nodal lines and the simulation's nodal lines for the 4ND

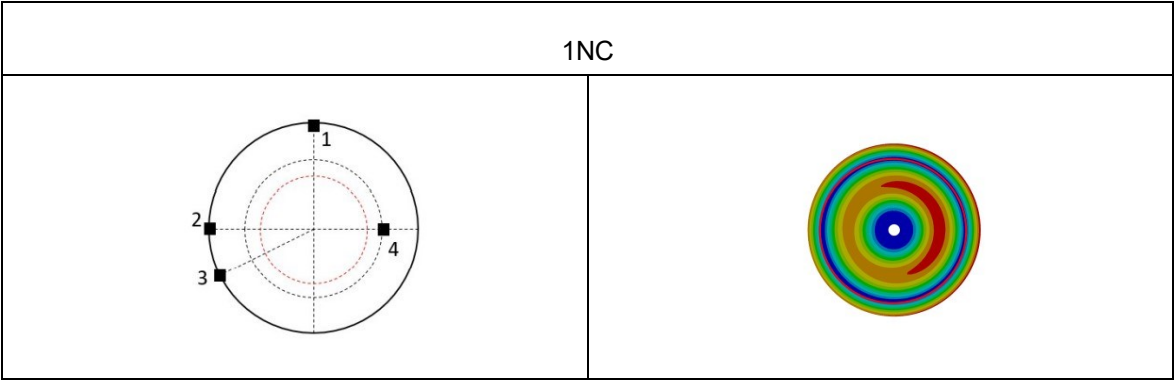


**Table 13** Comparison between the laboratory's nodal lines and the simulation's nodal lines for the 1NC

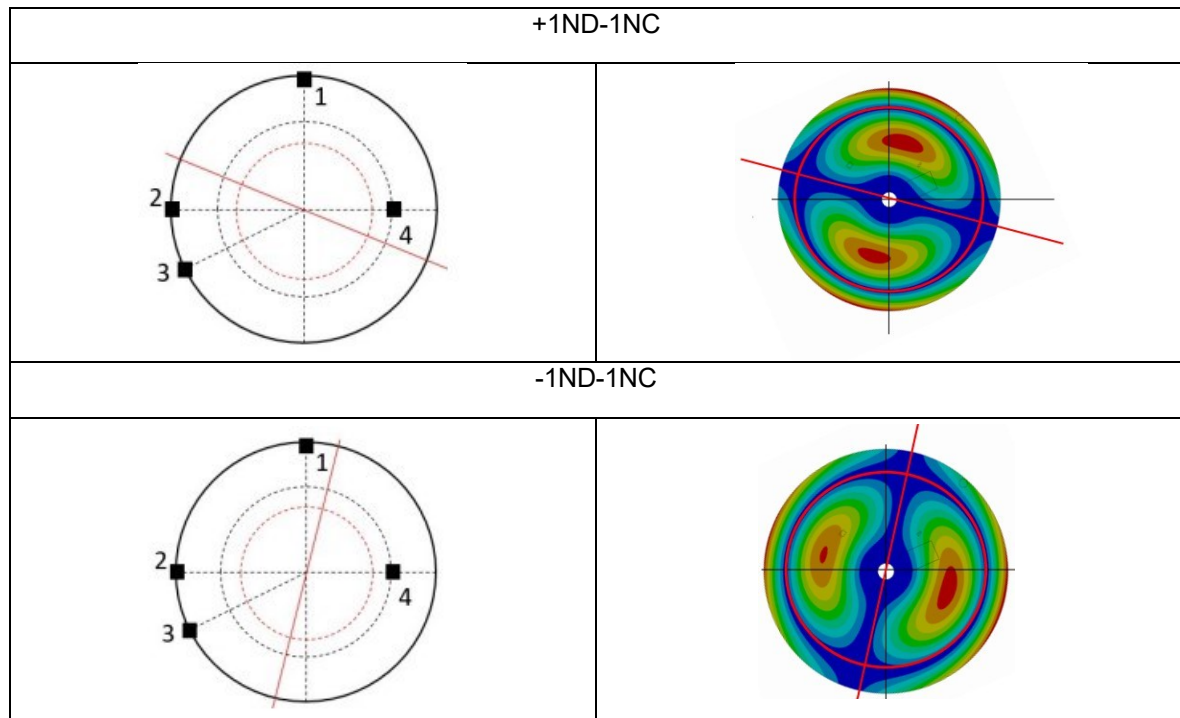


**Table 14** Comparison between the laboratory's nodal lines and the simulation's nodal lines for the 1ND 1NC

From the comparison it is possible to notice that all nodal lines in the simulation present a rotation compared to the laboratory ones, however, the angle between the nodal lines is not constant for every mode shape, it decreases progressively when the frequency increases, until the last mode shape 1ND 1NC, where the nodal lines match perfectly.

The different positions of the nodal lines could relate to the difference between the virtual geometry used during the simulation and the real geometry and also to some simplification made on the geometry as the absence of the bolts and the bearings, moreover, this incongruence could affect also the peaks of amplitude obtained from the harmonic simulation because the position of the strain gauges is the same of the laboratory but the rotation of the mode shapes could create a different signal emitted by the strain gauges a strain gauge could analyze a different signal because of its position.

## 5.2. Harmonic analysis validation

For the harmonic analysis in ANSYS is necessary to use the block “Harmonic Analysis”, using the same geometry and materials as in modal analysis. The boundary conditions used are the same as in modal analysis, in fact, the same values of stiffness are used for the bearings. The main difference is the addition of the piezoelectric patch defined using a “PiezoAndMems” extension. To obtain an excitation from the patch it is necessary to define a volta for both the POSITIVE and NEGATIVE layers, in particular -100V for the NEGATIVE layer and 400 V for the POSITIVE layer. To obtain data about the strain there are three strain gauges and one accelerometer as in the real geometry and the same position, it is possible to observe the position in **Figure 15**.

The solution of that analysis contains a graphical solution of the frequency response and the corresponding tabular data of the strain amplitude (m/m) and a phase angle associated with each frequency.

To obtain information about the strain there are different ways in ANSYS, during this project three different analyses are used **equivalent (von-mises) Strain, Principal elastic strain, Normal elastic strain, and frequency response**. The equations of those analyses are explained in chapter 3.5.2

To have a better view of the deformation and the strain the following part is divided into chapters, and every chapter will be dedicated to a single mode shape. Inside the single chapter, every sensor will be investigated separately and at the end of the chapter, the conclusion will summarize all the results. In order not to make the discussion too thoughtful only the first five modes shape will be analyzed.

### 5.2.1. 1ND

#### SG2



**Figure 30** Strain obtained for Equivalent von mises on the left and Maximum principal on the right for 1ND (SG2)

#### SG2

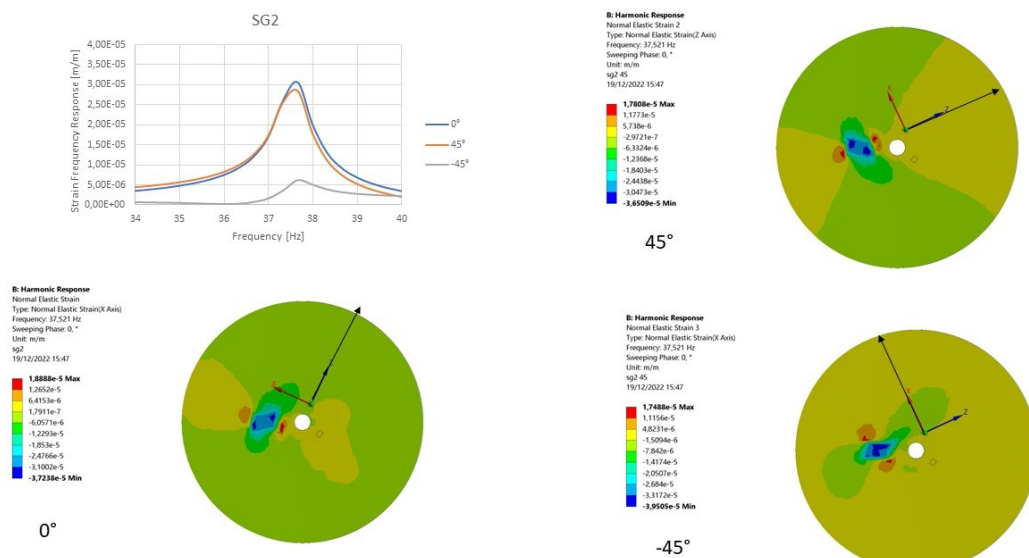


**Figure 31** Comparison between the Normal elastic Strain for the three directions of SG2 for the 1ND

## SG3

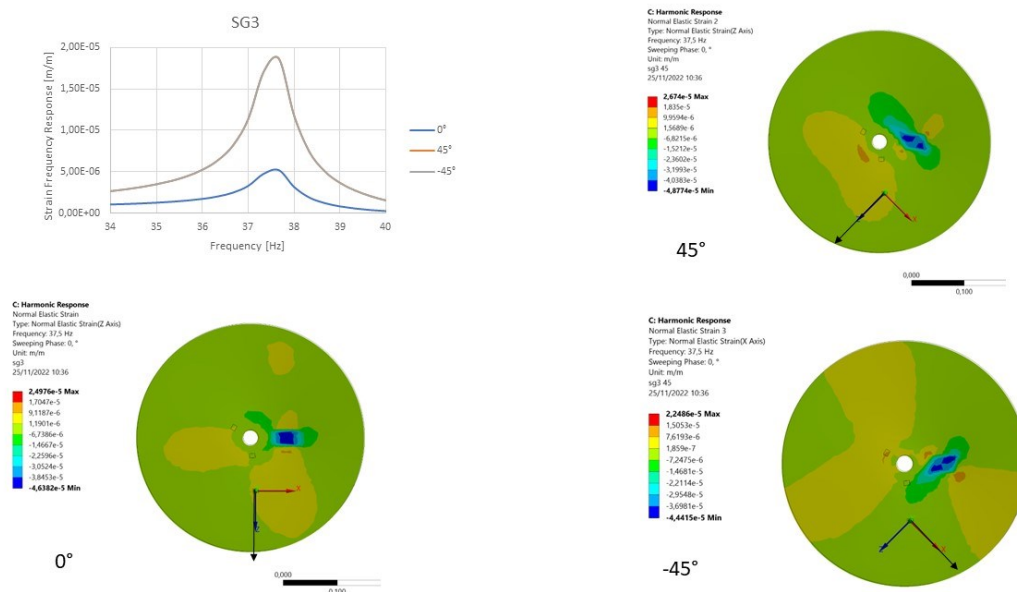


**Figure 32** Comparison between the Normal elastic Strain for the three directions of SG3 for the 1ND

## SG4

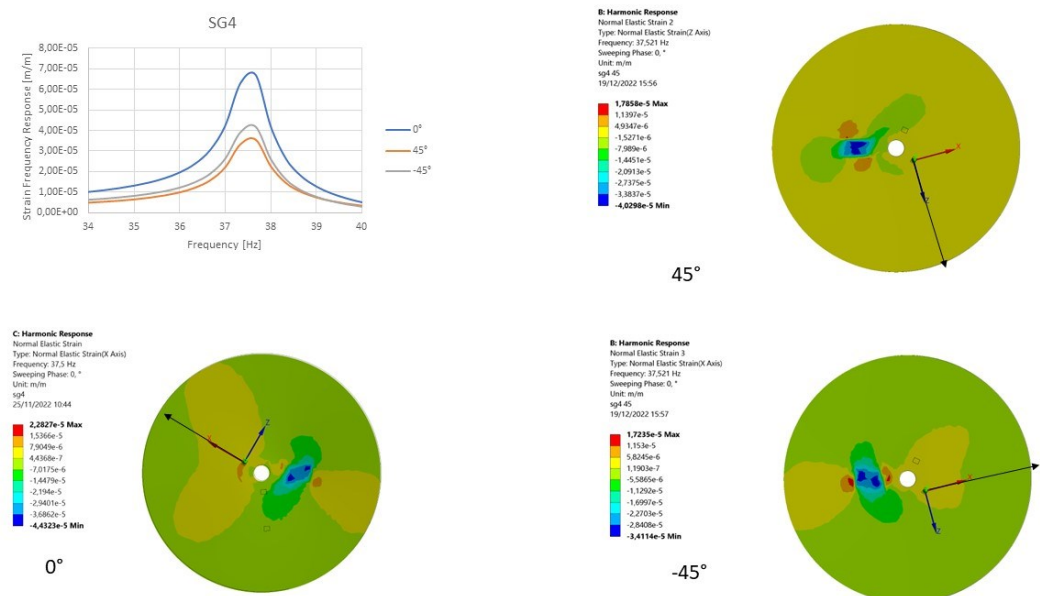


**Figure 33** Comparison between the Normal elastic Strain for the three directions of SG4 for the 1ND

## ACCELEROMETER

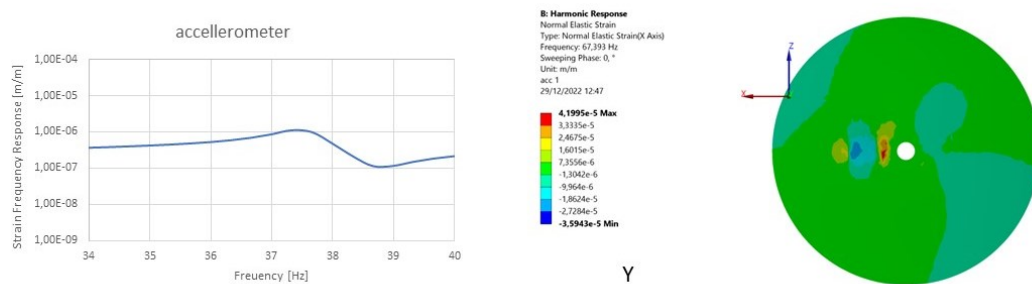


**Figure 34** Peak of the strain on the left and the normal strain on the right

## CONCLUSION

1ND 0°		
	maximum	minimum
Sg2	1,88e-5	-3,72e-5
Sg3	2,49e-5	-4,63e-5
Sg4	2,28e-5	-4,43e-5
1ND 45°		
Sg2	1,78e-5	-3,65e-5
Sg3	2,26e-5	-4,87e-5
Sg4	1,78e-5	-4,02e-5
1ND -45°		
Sg2	1,74e-5	-3,95e-5
Sg3	2,24e-5	-4,44e-5
Sg4	1,72e-5	-3,41e-5

**Table 15** Comparison between maximum e minimum value obtained by the normal strain for the three directions of SG1, SG2, and SG3.

The 1ND is the first mode shape at the lowest frequency, it is characterized by a single node line and two antinodes.

All the strain gauges present a peak of strain for the 1ND at 37,52 Hz which means the correct analysis was performed in modal acoustic. Regarding the Equivalent Strain and maximum strain, in **Figure 30**, it is clear that the maximum strain is located in the anti-node points of the 1ND as it must be.

The Normal elastic strain shows different values of strain following the direction of the strain gauges, the values are summarized in **Table 15**. The results confirm the strain frequency response, in fact, in every strain gauge the trend of the strain frequency response confirms the results of the normal strain, for example looking at the SG2 in **Figure 31** the maximum strain is expressed by the  $0^\circ$ , and the minimum value is by  $-45^\circ$  as it is the trend of the curves. The presence of the mode shape is also confirmed by the accelerometer which shows a flat curve and a peak at 37,52 Hz.

### 5.2.2. 0NC

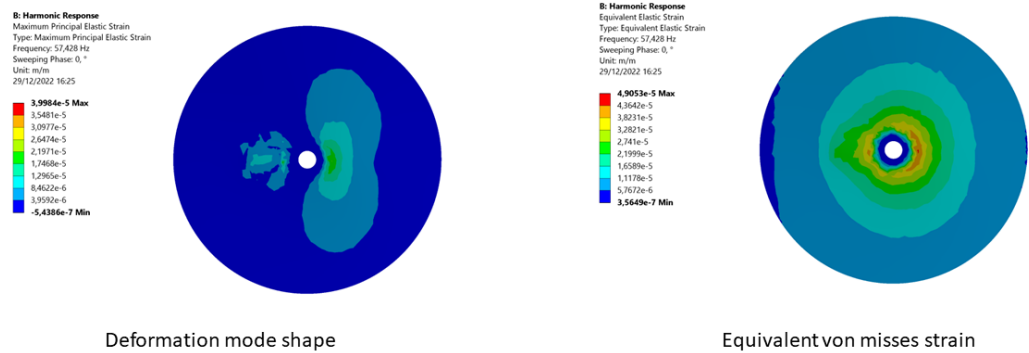


**Figure 35** Strain obtained for Equivalent von mises on the right and Maximum principal on the left for 0NC

### SG2

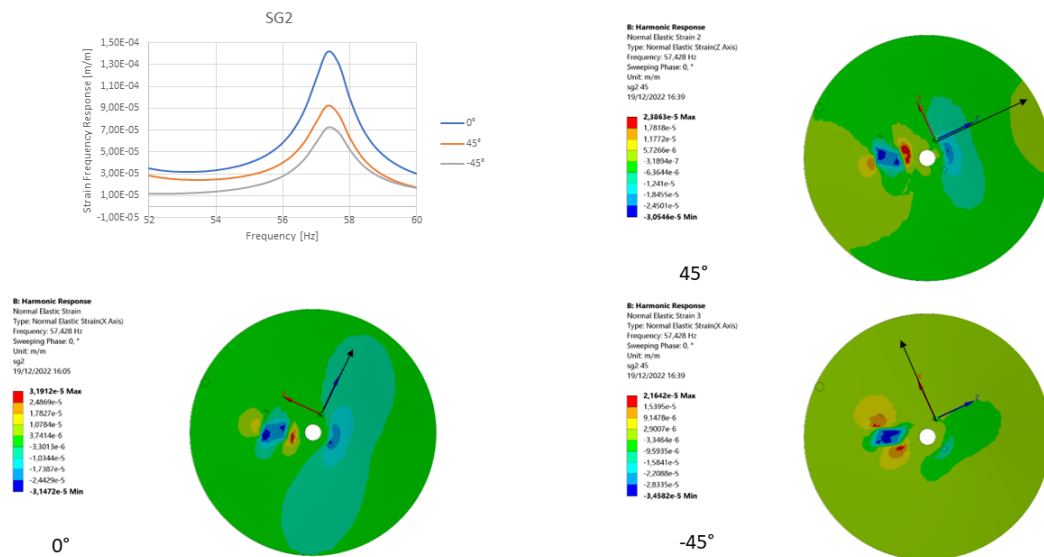


**Figure 36** Comparison between the Normal elastic Strain for the three directions of SG2 for the 0NC



## SG3

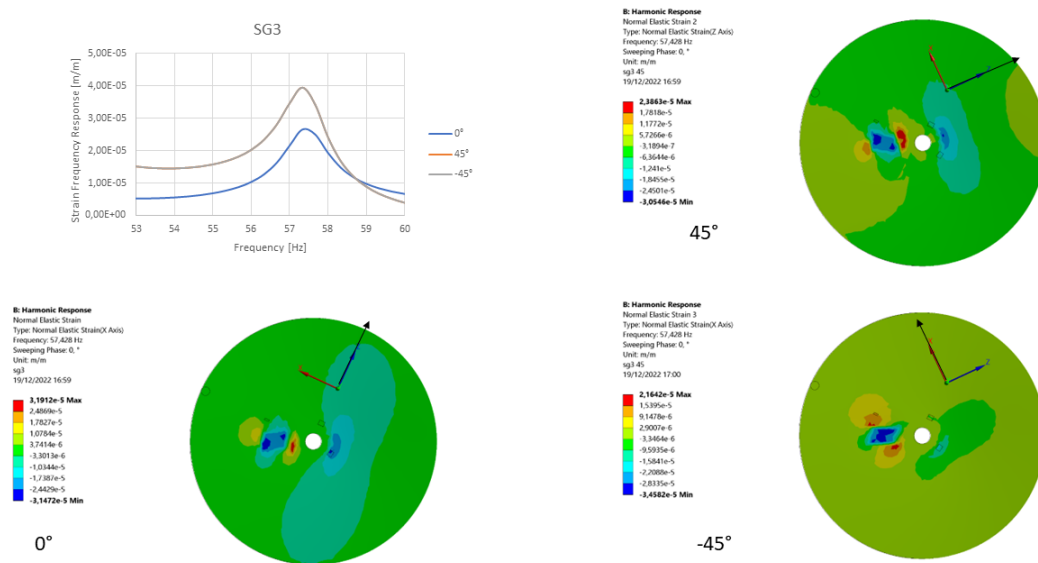


Figure 37 Comparison between the Normal elastic Strain for the three directions of SG3 for the 0NC

## SG4

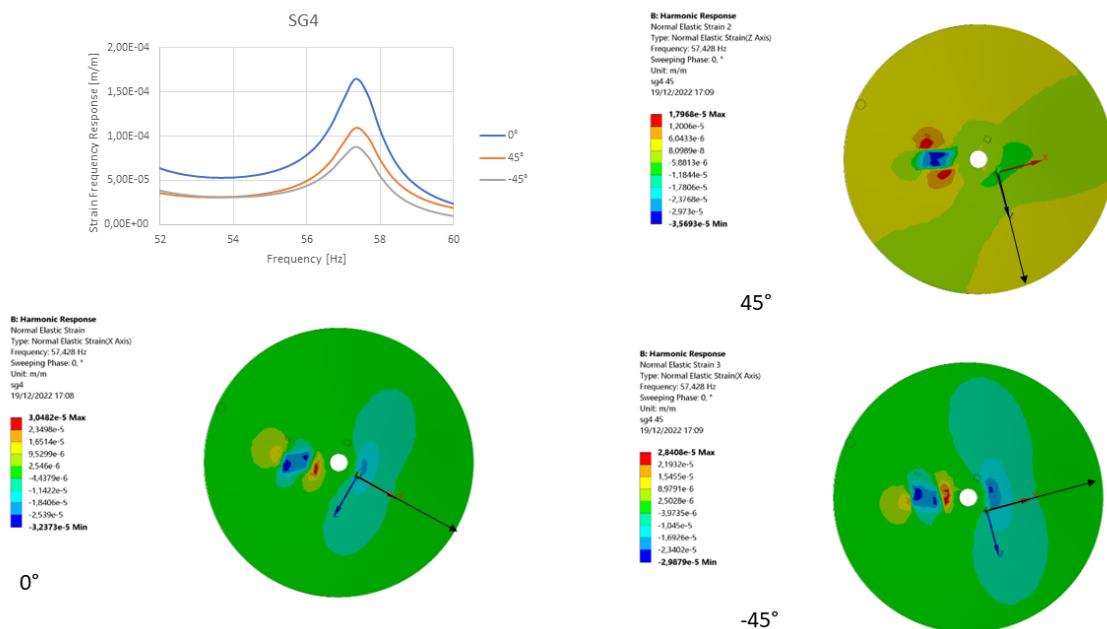
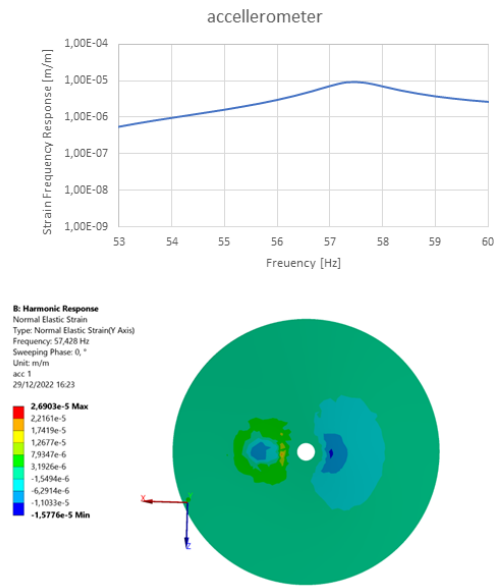


Figure 38 Comparison between the Normal elastic Strain for the three directions of SG4 for the 0NC

## ACCELEROMETER



**Figure 39** Peak of the strain on the left and the normal strain on the right

## CONCLUSION

0NC 0°		
	maximum	minimum
Sg2	3,1e-5	-3,1e-5
Sg3	3,1e-5	-3,1e-5
Sg4	3,0e-5	-3,2e-5
0NC 45°		
Sg2	2,3e-5	-3,0e-5
Sg3	2,3e-5	-3,0e-5
Sg4	1,7e-5	-3,5e-5
0NC -45°		
Sg2	2,1e-5	-3,4e-5
Sg3	3,1e-5	-3,4e-5
Sg4	2,8e-5	-2,9e-5

**Table 16** Comparison between maximum e minimum value obtained by the normal strain for the three directions of SG1, SG2, and SG3.

The 0NC is the second mode shape and the first of the 0NC mode shape group. All the strain gauges and the accelerometer present a peak of the amplitude at 57,2 Hz that confirms the presence of a natural frequency for that value. Regarding the Equivalent Strain and maximum strain, **Figure 35**, shows the presence of a maximum strain near the shaft where this mode shape presents the minimum deformation and the lowest strain on the edge of the disk. Looking at the zone where the maximum strain is concentrated and at the zone where the minimum strain is located it is clear that the mode shape is a 0NC.

The Normal elastic strain shows different values of strain in accordance with the direction of the strain gauges, the values are summarized in **Table 16**. Looking at SG2 and SG3 it is possible to notice that they present the same values of strain along all three directions, which confirms the presence of this mode shape that has no nodal lines the values are similar because the strain is almost the same along the disk. The results confirm the strain frequency response, in fact, in every strain gauge the trend of the strain frequency response confirms the results of the normal strain, for example looking at the SG2 in **Figure 36** the maximum strain is expressed by the  $0^\circ$ , and the minimum value is by  $-45^\circ$  as it is the trend of the curves, even if the difference between the three directions is less intense than the 1ND.

### 5.2.3. 2ND

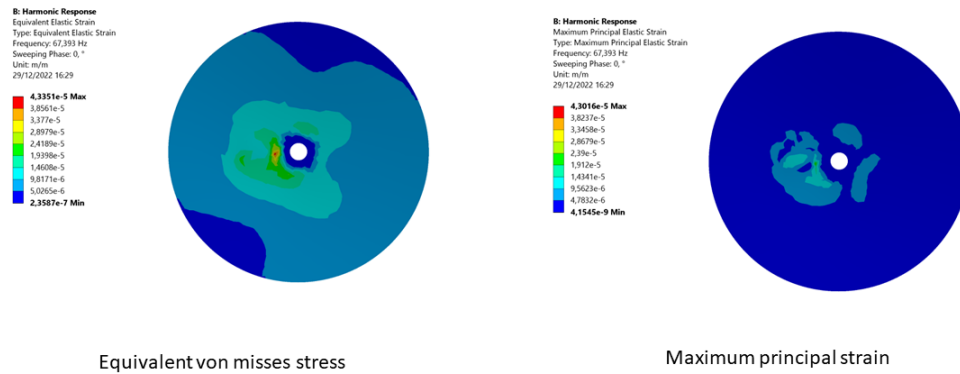


**Figure 40** Strain obtained for Equivalent von mises on the left and Maximum principal on the right for 2ND

### SG2

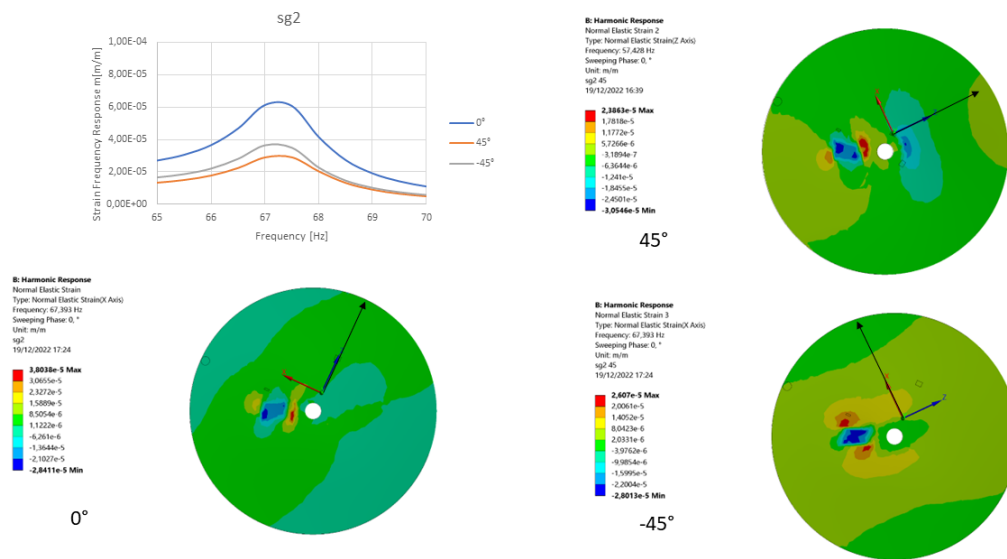


**Figure 41** Comparison between the Normal elastic Strain for the three directions of SG2 for the 2ND

## SG3

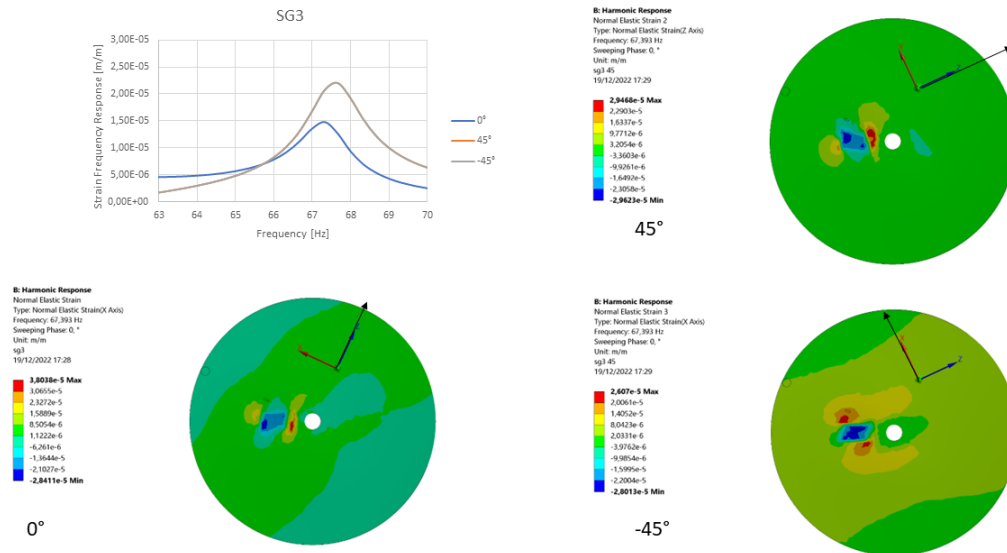


Figure 42 Comparison between the Normal elastic Strain for the three directions of SG3 for the 2ND

## SG4

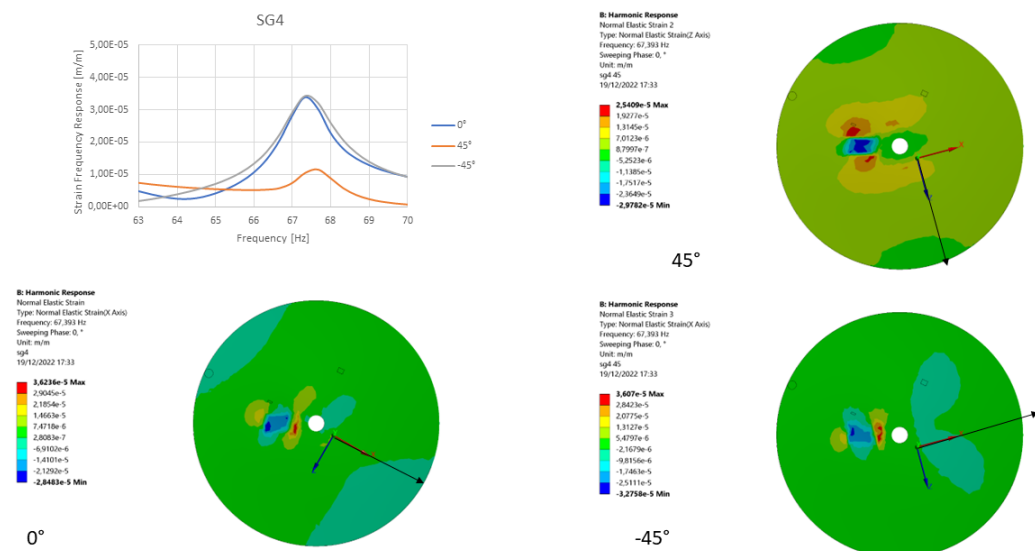
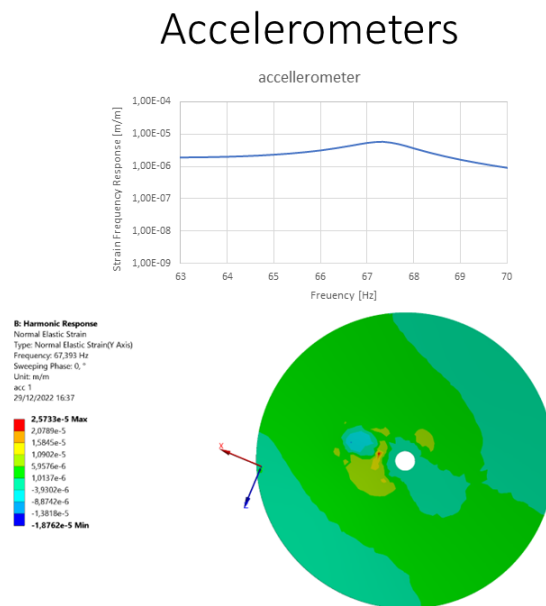


Figure 43 Comparison between the Normal elastic Strain for the three directions of SG4 for the 2ND

## ACCELEROMETER



**Figure 44** Peak in the strain frequency response on the top and normal strain along the orthogonal direction on the bottom

## CONCLUSION

2ND 0°		
	maximum	minimum
Sg2	3,8e-5	-2,8e-5
Sg3	3,8e-5	-2,8e-5
Sg4	3,6e-5	-2,8e-5
2ND 45°		
Sg2	2,3e-5	-3,0e-5
Sg3	2,9e-5	-2,9e-5
Sg4	2,5e-5	-2,9e-5
2ND -45°		
Sg2	2,6e-5	-2,8e-5
Sg3	2,6e-5	-2,8e-5
Sg4	3,6e-5	-3,2e-5

**Table 17** Comparison between maximum e minimum value obtained by the normal strain for the three directions of SG1, SG2, and SG3.

The 2ND is the second mode shape, it is characterized by two node lines and four antinodes.

All the strain gauges present a peak of strain for the 2ND at 67,39 Hz which means the correct analysis performed in modal acoustic and the correct position of the sensors that can detect the mode shape, regarding this even if all the sensors detect the mode shape the signal emitted by the accelerometer is less intense than the strain gauges, that means that the position of the accelerometer is near a nodal line. Regarding the Equivalent Strain and maximum strain, **Figure 40**, it is difficult to have clear information because the strain creates by the piezoelectric patch is higher than the strain produced by the deformation of the disk, however, from the equivalent strain it is possible to notice a strain zone that is similar to the deformation created by the mode shape.

Once again, the Normal elastic strain shows different values of strain according to the direction of the strain gauges, the values are summarized in **Table 17**. The results confirm the strain frequency response, in fact, in every strain gauge the trend of the strain frequency response confirms the results of the normal strain, looking at the SG4 in **Figure 44**, the maximum strain is expressed by the  $0^\circ$  and by the  $45^\circ$ , and the minimum value is by  $-45^\circ$  as it is the trend of the curves, the situation changes for the SG3 where the maximum strain is expressed by  $45^\circ$  and  $-45^\circ$  and the lower strain is shown by the  $0^\circ$ , **Figure 43**.

5.2.4. 3ND

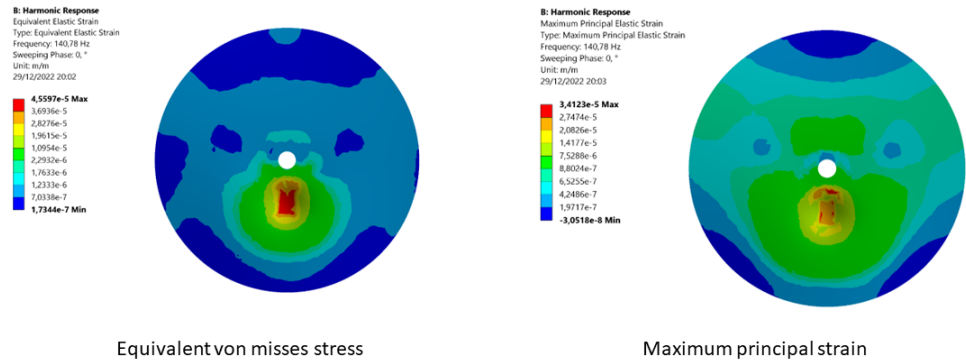


Figure 45 Strain obtained for Equivalent von mises on the left and Maximum principal on the right for 3ND

SG2

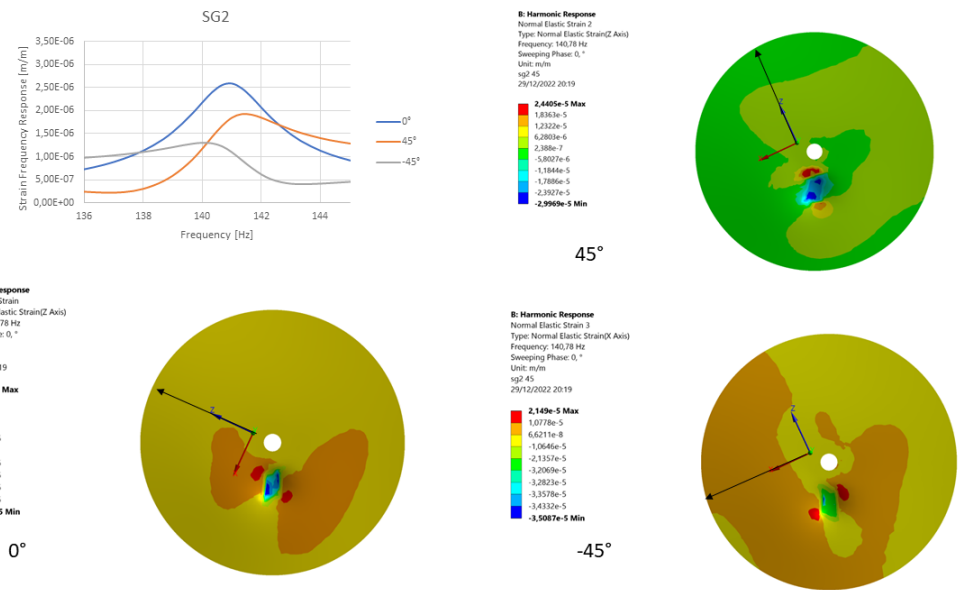


Figure 46 Comparison between the Normal elastic Strain for the three directions of SG2 for the 3ND



SG3

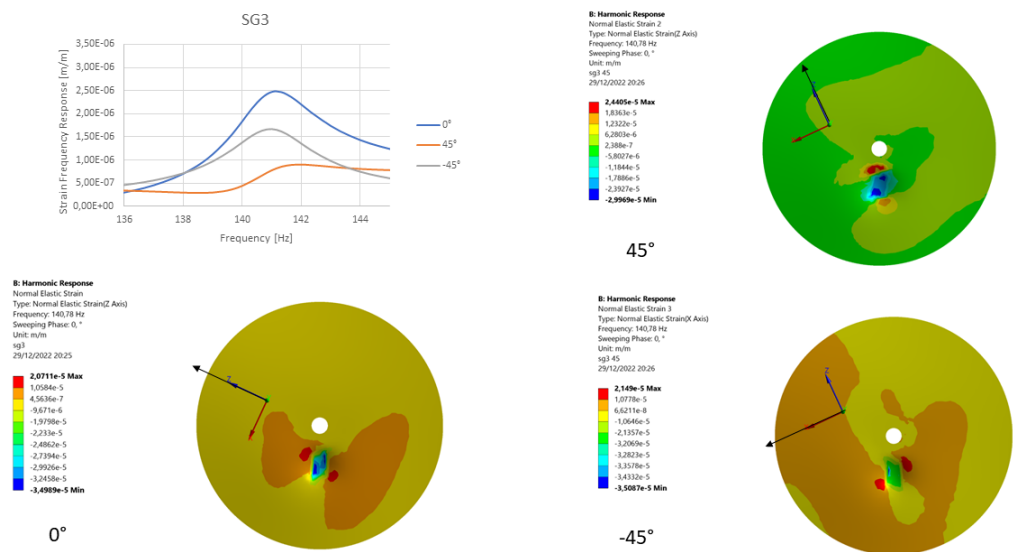


Figure 47 Comparison between the Normal elastic Strain for the three directions of SG3 for the 3ND

SG4

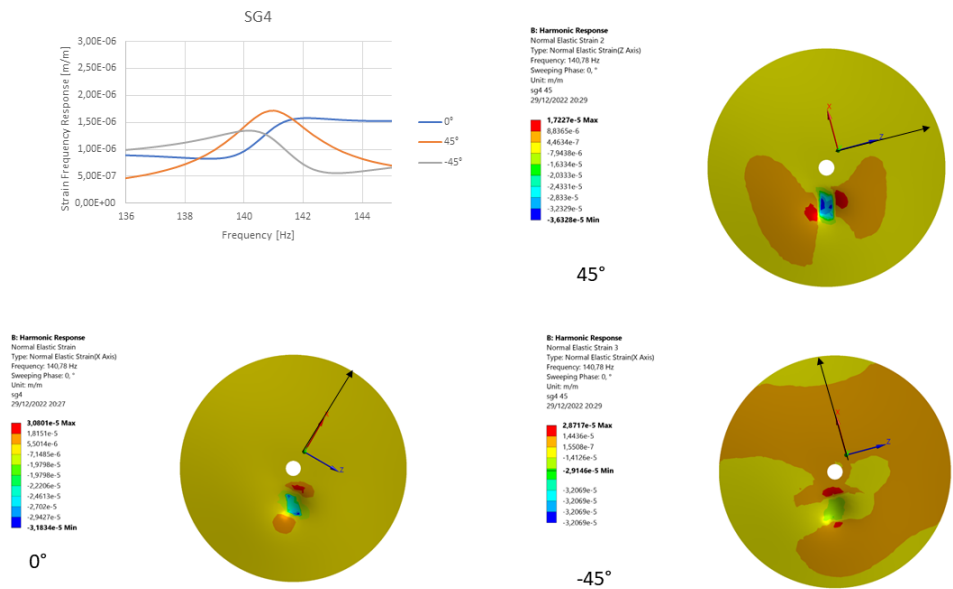
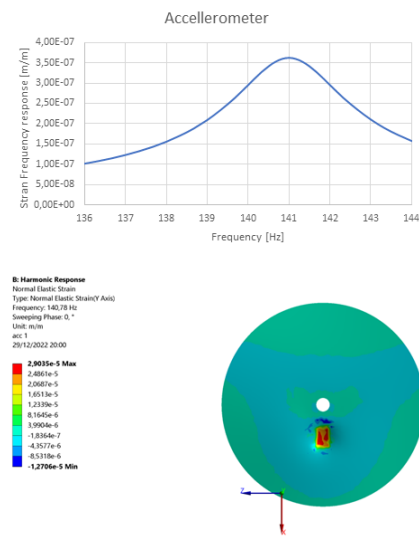


Figure 48 Comparison between the Normal elastic Strain for the three directions of SG4 for the 3ND

## ACCELEROMETER



**Figure 49** Peak in the strain frequency response on the top and normal strain along the orthogonal direction on the bottom

## CONCLUSION

3ND 0°		
	maximum	minimum
Sg2	2,0e-5	-3,4e-5
sg3	2,0e-5	-3,4e-5
sg4	3,0e-5	-3,1e-5
3ND 45°		
Sg2	2,4e-5	-2,9e-5
Sg3	2,4e-5	-2,9e-5
Sg4	1,7e-5	-3,6e-5
3ND -45°		
Sg2	2,1e-5	-3,5e-5
Sg3	2,1e-5	-3,5e-5
Sg4	2,8e-5	-3,2e-5

**Table 18** Comparison between maximum e minimum value obtained by the normal strain for the three directions of the SG1, SG2, SG3.

The 3ND is the third mode shape and looking at the value of the strain it is clear that the values of the strain are lower than the ones of the 2ND higher is the frequency and lower the movement of the disk, despite this fact, all the strain gauges and the accelerometer present a peak of the amplitude at 140,78 Hz that confirm the presence of a natural frequency for that value, the main difference is that the strain gauges show a higher amplitude than the accelerometer. Regarding the Equivalent Strain and maximum strain, Figure 45, shows the presence of a maximum strain where the patch is located, which means that the strain produced by the patch overlooked the strain produced by the movement of the disk, thus the analysis of the equivalent strain and maximum strain is difficult to interpret.

The Normal elastic strain shows different values of strain according to the direction of the strain gauges, the values are summarized in **Table 18**, the main thing of note is that in every strain gauge, there is a direction where the peak is not clear, the reason could be due to the position and the direction of analysis this mode shape presents three nodal lines that could affect the position of the strain gauge.

5.2.5. 4ND

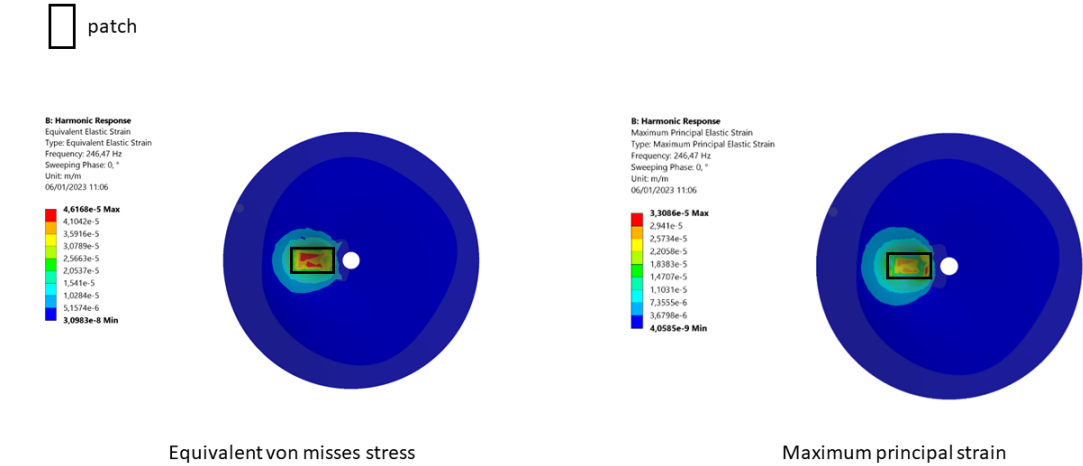


**Figure 50** Strain obtained for Equivalent von mises on the left and Maximum principal on the right for 4ND

SG2

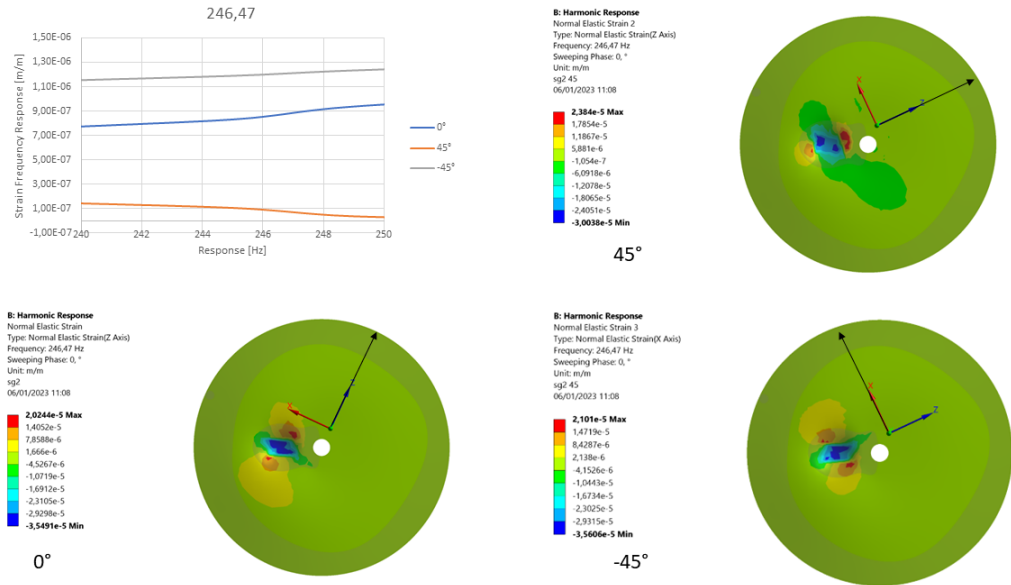


**Figure 51** Comparison between the Normal elastic Strain for the three directions of SG2 for the 4ND

SG3

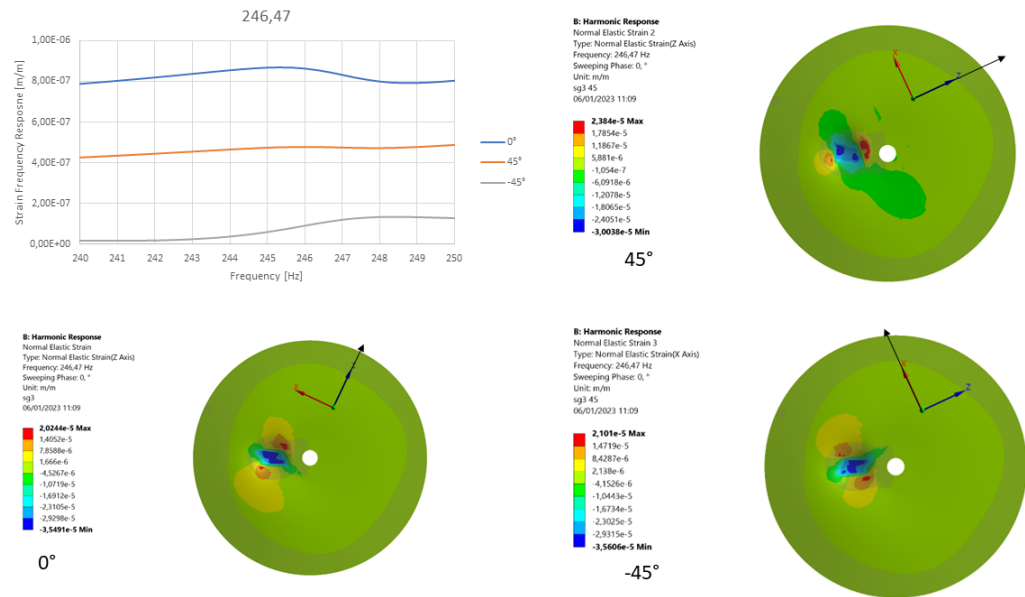


Figure 52 Comparison between the Normal elastic Strain for the three directions of SG3 for the 4ND

SG4

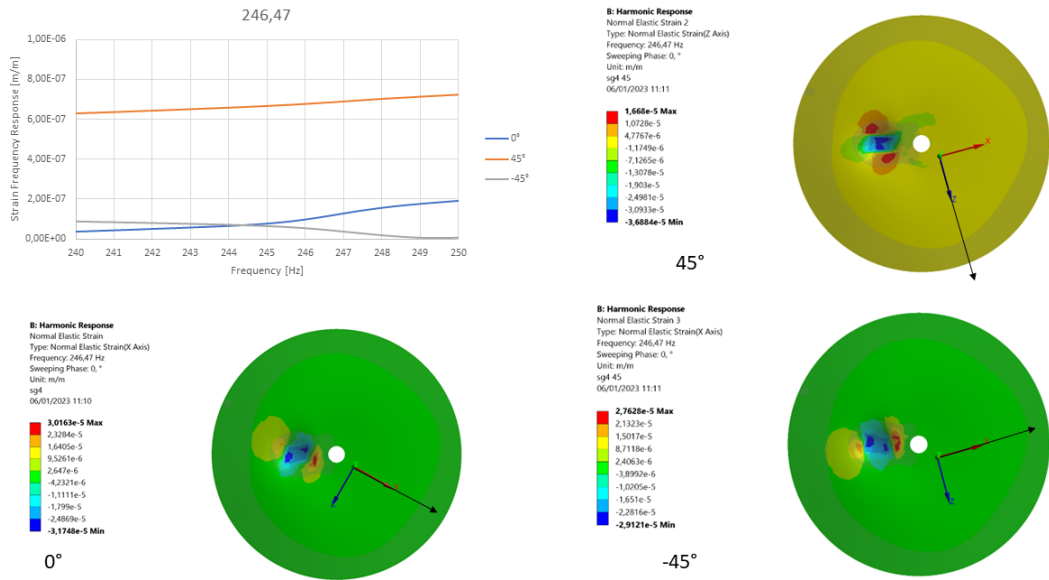
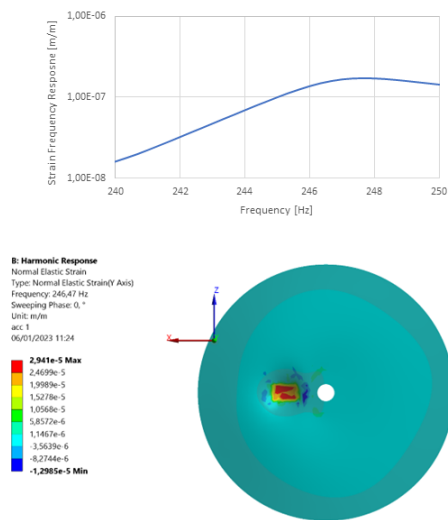


Figure 53 Comparison between the Normal elastic Strain for the three directions of SG3 for the 4ND

## ACCELEROMETER



**Figure 54** Peak in the strain frequency response on the top and normal strain along the orthogonal direction on the bottom

## CONCLUSION

4ND 0°		
	maximum	minimum
Sg2	3,19e-5	-3,14e-5
Sg3	3,19e-5	-3,14e-5
Sg4	3,04e-5	-3,23e-5
4ND 45°		
Sg2	2,38e-5	-3,05e-5
Sg3	2,38e-5	-3,05e-5
Sg4	1,79e-5	-3,56e-5
4° -45°		
Sg2	2,16e-5	-3,45e-5
Sg3	3,16e-5	-3,45e-5
Sg4	2,84e-5	-2,98e-5

**Table 19** Comparison between maximum e minimum value obtained by the normal strain for the three directions of the SG1, SG2, and SG3.

The 4ND is the last mode shape of the first seven mode shapes that belongs to the ND shape group. Analyzing the maximum value it is clear that the amplitude is lower than the 1ND, this fact creates some problems for the strain gauges, in fact from the strain frequency response it is not clear the presence of a peak at 246,47Hz if not for the SG3 in 0° direction, looking at the SG2 and SG4 they present a flat curve except for a slight increase around 246 Hz for all the three directions, those results don't give enough information to declare the presence of a mode shape, but the accelerometer presents a peak for the 4ND that permits to confirm the presence of a natural frequency, although with low amplitude to the mode shape. Therefore, in this case, the position of the strain gauges is not optimized to detect the 4ND due to the low movement of the disk, the accelerometer has a good position, and it can detect it. Also, the *Equivalent Strain* and *Maximum strain*, **Figure 50**, show the presence of a difficult analyze the strain of this mode, is clear the presence of a spot with a higher value, this spot is characterized by the presence of the patch whose movement prevails over the movement of the disk, for this reason, those simulations give results difficult to comment.

Regarding the Normal elastic strain, the situation is similar to what happened for the *Equivalent Strain*, it shows almost the same values of strain for all the strain gauges, and the values are summarized in **Table 19**.

### 5.2.6. Strain Frequency Response

The following part of the project is focused on the signal emitted by the strain gauges, to find if there is a similarity between the laboratory's signal and the simulation's signal. The object is to find the peaks of the mode shapes and analyze the trend of the signal.

The signal obtained by the harmonic analysis and by the test is in the form of Strain Frequency Response (SFR). The SFR is a method used to measure and analyze the dynamic behavior of a material or structure under varying frequency excitation. It is similar to the frequency response function (FRF), but instead of measuring the response of a system in terms of displacement or velocity, it measures the response in terms of strain. The SFR can be determined experimentally using techniques such as strain gauge testing or dynamic mechanical analysis (DMA), where a strain gauge or other transducer is used to measure the strain in a material or structure as a function of frequency. The SFR can also be determined theoretically using finite element analysis (FEA) or other numerical methods. The equation of the SFR depends on the method used to measure the strain in a material or structure, as in the case of the project using a strain gauge the SFR can be represented by the equation:

$$SFR(j\omega) = \frac{\frac{\Delta R}{R}}{\frac{F(j\omega)}{A}} \quad 5.1$$

Where,  $SFR(j\omega)$  is the strain frequency response, which is the ratio of the change in resistance  $\Delta R$  to the initial resistance  $R$  of the strain gauge,  $F(j\omega)$  is the input force,  $A$  is the cross-sectional area of the gauge,  $\omega$  is the angular frequency and  $j$  is the imaginary unit.

Another possibility is the following equation:

$$SFR(j\omega) = \tan(\delta) * e^{(j*\varphi)} \quad 5.2$$

Where  $SFR(j\omega)$  is the complex modulus,  $\delta$  is the loss angle,  $\varphi$  is the phase angle and  $\omega$  is the angular frequency and  $j$  is the imaginary unit.

Before starting to look at the graph it is important to summarize the information found until now, firstly, between the nodal lines found in the laboratory and the nodal lines found in the simulation there is a discrepancy, this could affect the signal in the simulation because the strain gauge will receive different excitation than the ones in the laboratory.



Secondly, there is an error between the frequencies found in the laboratory and the simulation, which means that the peaks will be not at the same frequency.

The following graph is divided into three groups based on the frequency range 20-80 Hz, 120-170Hz and 230-300 Hz, there are some holes between the groups because to obtain more accuracy in the signal the frequency where there are no peaks are ignored, in fact in the harmonic analysis to obtain the SFR is necessary to define a range and several points where the SFR is analyzed, but higher is the number of points and higher will be the time to solve the simulation, thus to obtain a good accuracy but with lower time it is necessary to reduce the range of frequency. The sensors used to perform this simulation are always the strain gauges 2, 3, 4, and the accelerometer.

To compare the simulation with the laboratory results was necessary to extract the data, and for doing this used the program LabVIEW. The chirp signal has been tested when the structure was in the air, the FFT has been analyzed using the program LabVIEW which stores the data in a Technical Data Management Streaming (TDMS) file. Regarding the FFT, it is an algorithm used to perform a mathematical operation called a Fourier transformation, which is a mathematical technique that can be used to decompose a signal into its frequency components. The FFT algorithm takes a discrete signal as input, such as time series of measurements, and converts it into a representation in the frequency domain, this representation shows the relative amplitudes of the different frequency components present in the signal. LabVIEW has been set up to read the file TDMS and to perform the FFT which is the spectrum of the signals obtained to find the peaks and the amplitude.

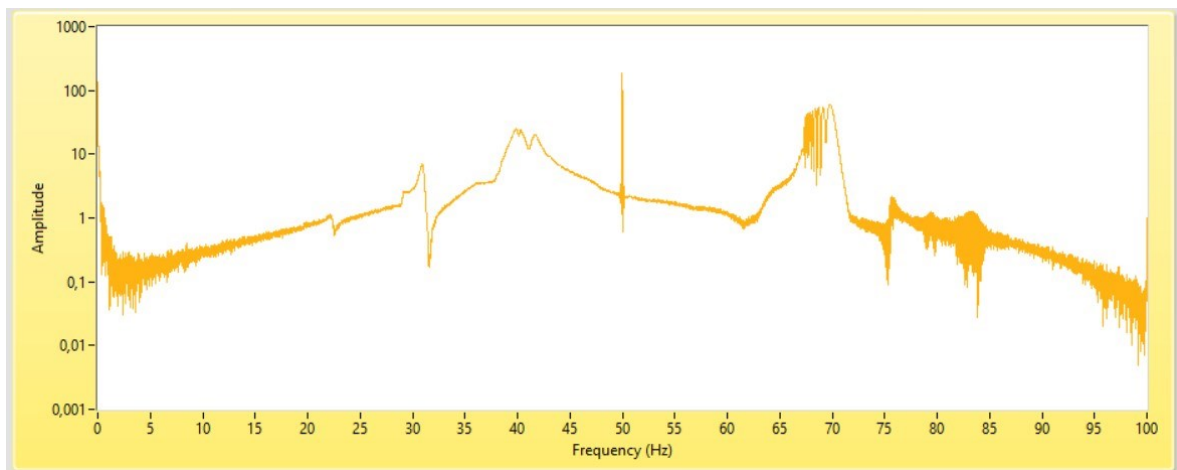


**Figure 55** FFT of the strain obtained from the chirp 0-100 Hz in air

The illustration is very easy, there are two axis Amplitude and Frequency, as it is possible to notice that around a natural frequency, there is an increase in the amplitude. The LabView analysis has been performed for three ranges 0-100 Hz, 100-200 Hz, and 200-300 Hz, and the SFR was obtained.

Regarding the simulation, the harmonic analysis is the way to obtain the SFR for three different ranges: 20-80Hz, 120-170Hz, and 230-300Hz. For each range, it was used 400 points to reach a good accuracy in the curves and the peaks.

The following part will present a comparison between the SFR in simulation and laboratory, the curves present a lot of peaks because the system analyzed is complex and in addition to the mode shapes of the disk there are also the mode shapes of the shaft that are present in the curves.

In this graph, only the 1ND, 0NC, 2ND, 3ND, and 4ND are analyzed to simplify the treatment. Regarding the nomenclature it is necessary to clarify: the SG2, SG3, and SG4 are the strain gauges of the model while in the simulation the sg1, sg2, and sg3 are the three directions at  $-45^\circ$ ,  $0^\circ$  and  $45^\circ$  of the strain gauges corresponding to the SG2 in simulation; the sg4, sg5, and sg6 are the three direction at  $-45^\circ$ ,  $0^\circ$  and  $45^\circ$  of the strain gauges corresponding to the SG3 in simulation, and lastly the sg7, sg8, and sg9 are the three direction at  $-45^\circ$ ,  $0^\circ$  and  $45^\circ$  of the strain gauges corresponding to the SG4 in simulation.

## 20-80 Hz

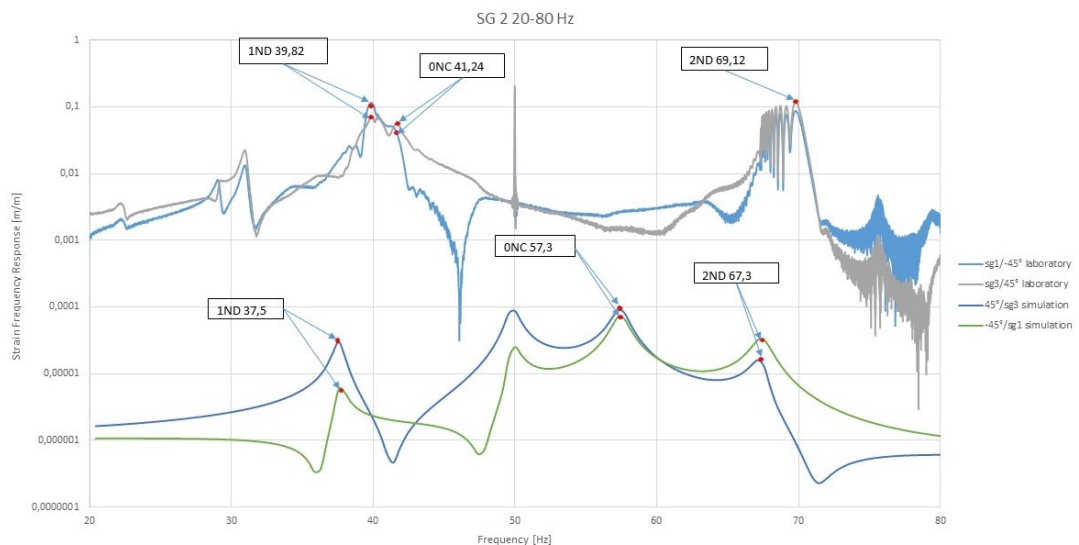


**Figure 56** Strain gauges signal from laboratory and simulation for SG2

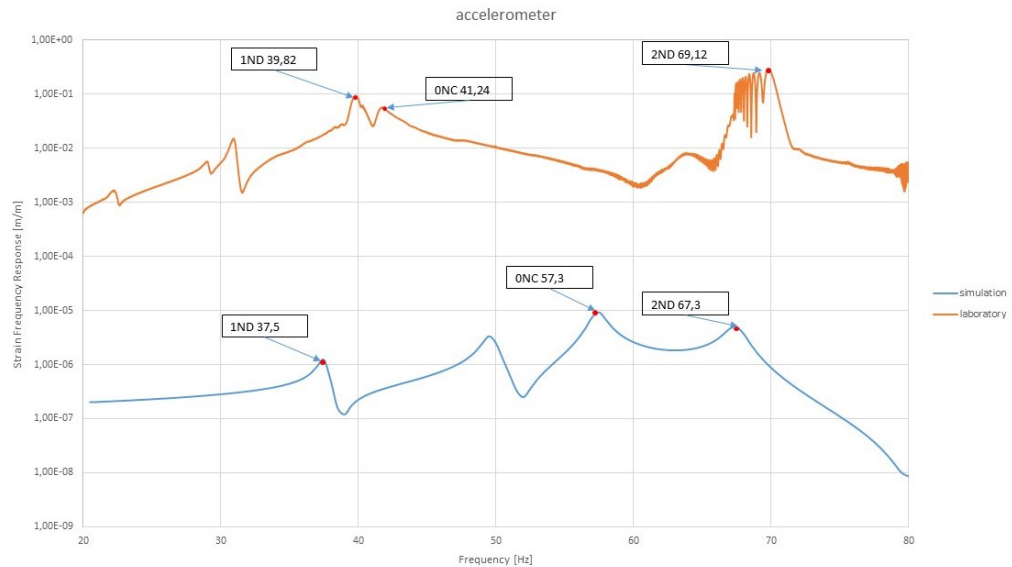


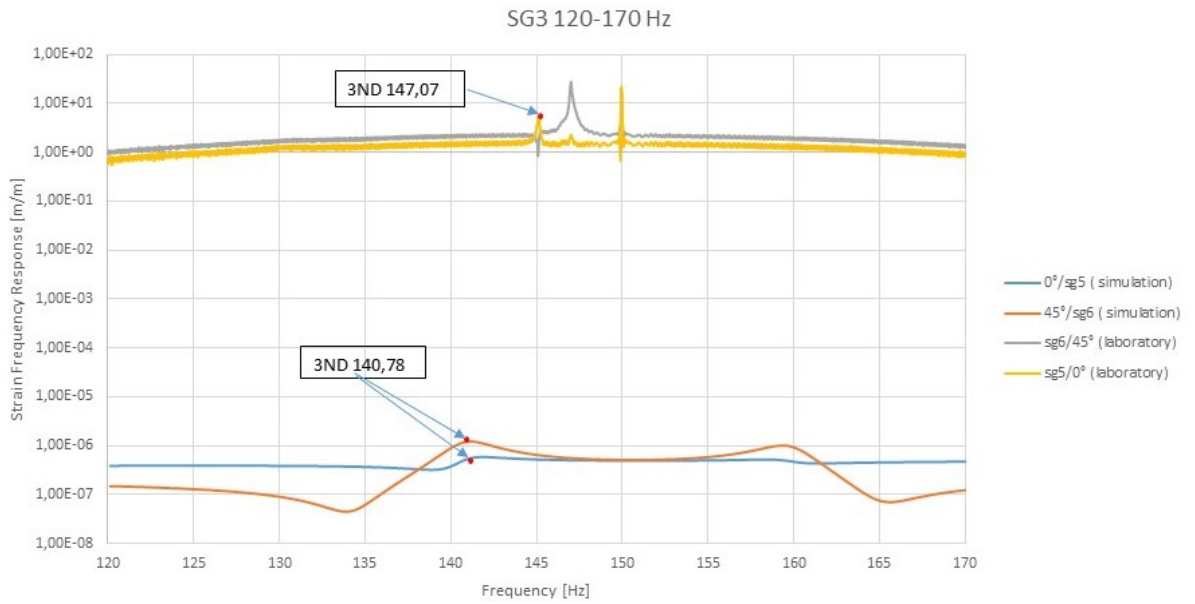
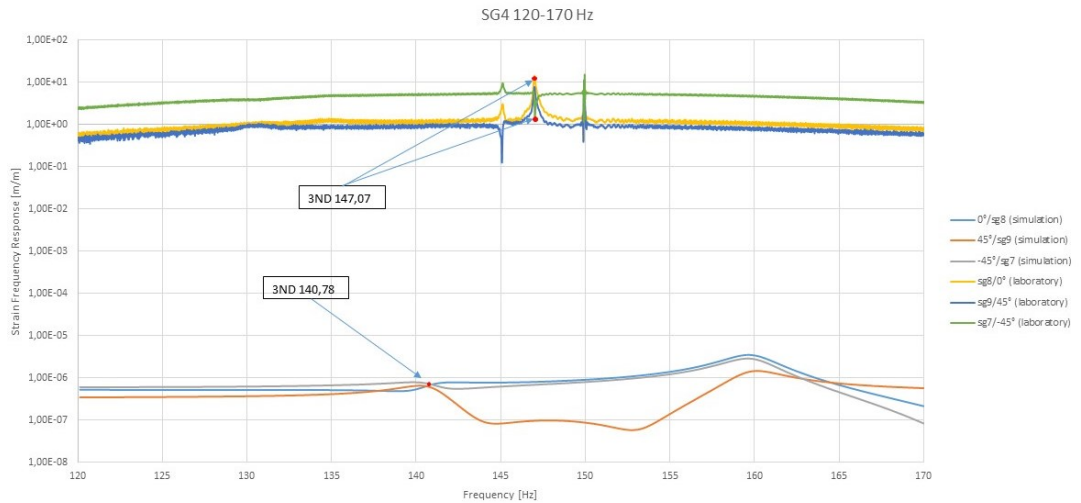
**Figure 57** Strain gauges signal from laboratory and simulation for accelerometer

The first range of frequency goes from 20 to 80 Hz, for the SFR obtained by the strain gauges, it is possible to notice a well-correlation between the laboratory and simulation, for the 1ND the signal emitted by the strain gauge at  $45^\circ$  In simulation is above the one at  $-45^\circ$  as in the laboratory, instead for the 2ND there is an inversion as in the laboratory, also the 0NC is similar but due to of the huge error in the frequency value, they are very far away.

The signal emitted by the SG3 it is very similar to the SG2, and it presents a good correlation with the laboratory curves trend. To lighten the content, the graph of the SG3 and SG4 are in **Appendix D**.

The signal from the accelerometer is clearer without all the fluctuations present in the strain gauges, it confirms the presence of the peaks for the 1ND, 1NC, and 2ND and a good representation of reality.

From the analysis of the first range of frequency, it is possible to confirm that the model in the air is well-matched with the laboratory test the peaks of the amplitude are the same as the laboratory SFR, which confirms the presence of the mode shapes found in the modal analysis and the other of the natural frequency. Moreover, the trend of the curves for the strain gauges is the same in the laboratory and simulation, which means that the simulation is correct and that strain gauges can detect the same signal confirming the correct positioning for the detection of these mode shapes.

**120-170 HZ****Figure 58** Strain gauges signal from laboratory and simulation for SG3**Figure 59** Strain gauges signal from laboratory and simulation for accelerometer

In the second range which goes from 120-170 Hz, it is possible to analyze only SG3 and SG4 because there was too much noise in the laboratory's data, moreover, in this range, there is only one mode shape. For the SG3 the signal is well-correlated with the laboratory, in fact, for the peak, the 45° signal is above

the 0° signal as in the laboratory. The main problem is that the signal in the simulation is almost flat, making it difficult to see the peak that is instead very clear in the SFR of the test.

As in SG3, for the SG4 there is a very low peak while in the laboratory the peak is clear **Figure 59**, so it is difficult to have a clear analysis for these strain gauges. These flat curves are probably related to the fact that the positions of the strain gauges are not correct to detect this mode shape that presents many nodal lines. Another problem is the noise of the laboratory results the accelerometer and the SG2 are not considered because the signal is too noisy.

## 230-300 Hz

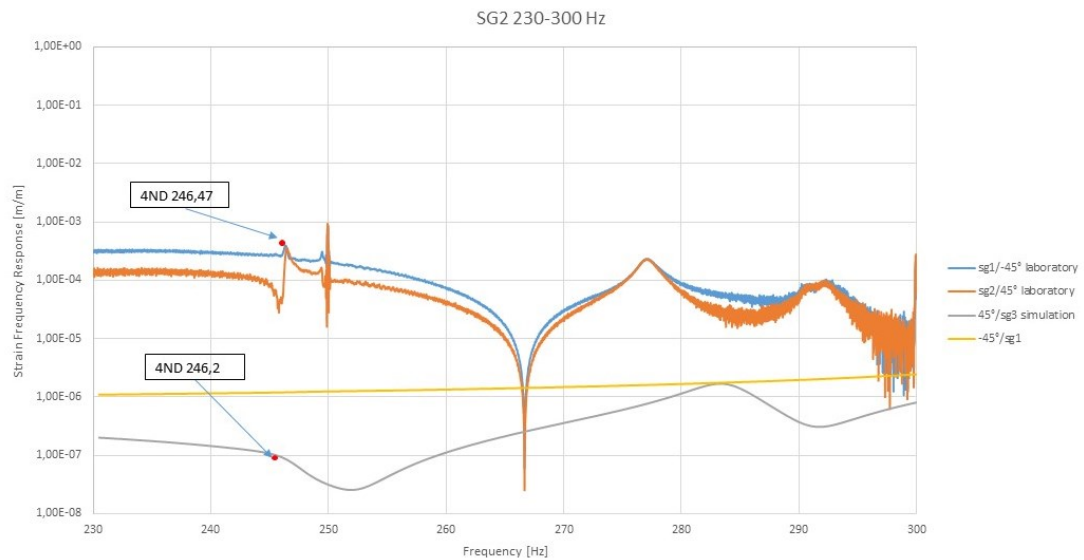


**Figure 60** Strain gauges signal from laboratory and simulation for SG2

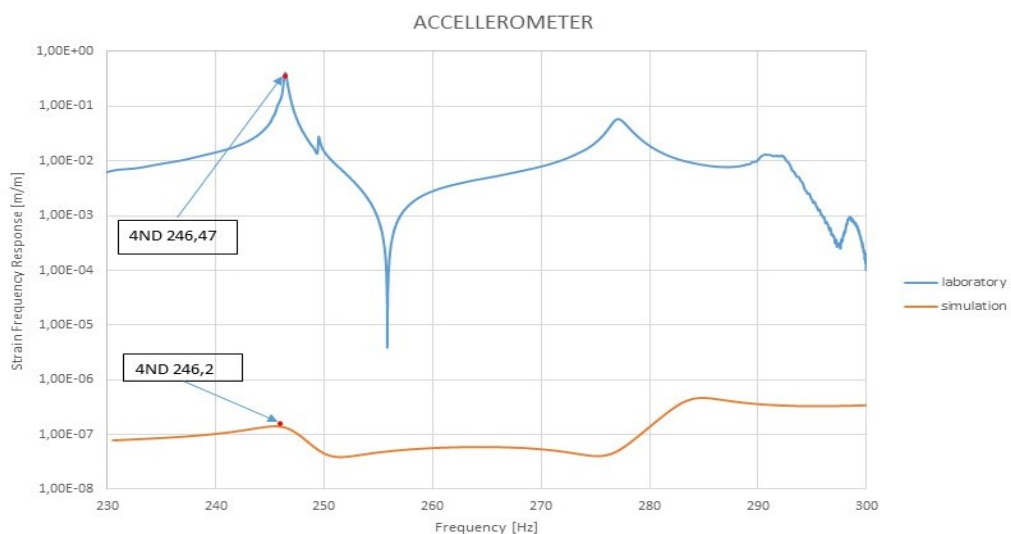


**Figure 61** Strain gauges signal from laboratory and simulation for accelerometer

The final range goes from 230-300 Hz, in this case, the noise is reduced and for this reason, it is possible to analyze all the sensors, the problem is the same as the previous range, in fact also, in this case, the 3ND is not well-detected by the strain gauges and it is difficult to analyze it, however, the signal from the accelerometer is clearer and it is possible to notice the presence of a peak at the frequency of the 4ND.

To conclude this part of the project and summarize the results, the signals from the laboratory and simulation are very similar in all the mode shapes. As expected the peaks are not in the same positions due to the presence of errors between the laboratory's frequencies and the simulation's frequencies. Moreover, because there is a different angular position between the nodal lines found in the simulation and the ones found in the laboratory there is an effect on the position of the strain gauges, this effect creates a not well-detected signal for the 3ND and 4ND because the strain gauge is in a zone where the strain is low, probably they are on a nodal line.

Finally, this part concludes the validation of the model in the air without the rotation, all the experiments carried out gave good results that matched with the experimental ones. It is possible to end up concluding that the behavior in the air is similar to the experimental data, so it is possible to confirm that the model can reproduce the structural response of the disk.

However, the location of the strain gauges affects the signal obtained, in fact, in some cases, it may not produce any peak in the strain response.

### 5.3. Influence of the rotation

The previous simulation has been performed in the air but without the influence of a rotational velocity, this part of the project aims to add a rotational velocity to analyze its impact of it on the mode shapes.

To check the rotational effect, during the experiments in the laboratory was added a rotational velocity for different values to analyze the dynamic response of the system in terms of changing the frequency of mode shapes. The experiment was carried out at 50 rpm, 100 rpm, 150 rpm, 200 rpm, 250 rpm, and 300 rpm. The duration of the chirp excitations is 120 seconds for each rotating speed using three different ranges of frequencies: 0-100 Hz, 100-200Hz, and 200-300Hz. To extract the signal and value of the frequency for the mode shapes LabVIEW is used. **Figure 62** is shown the temporal signal of the accelerometer for 0 rpm, 100 rpm, and 200 rpm, it is clear that with the increasing of the velocity, there is a variation of the frequency, in this case, a drop.

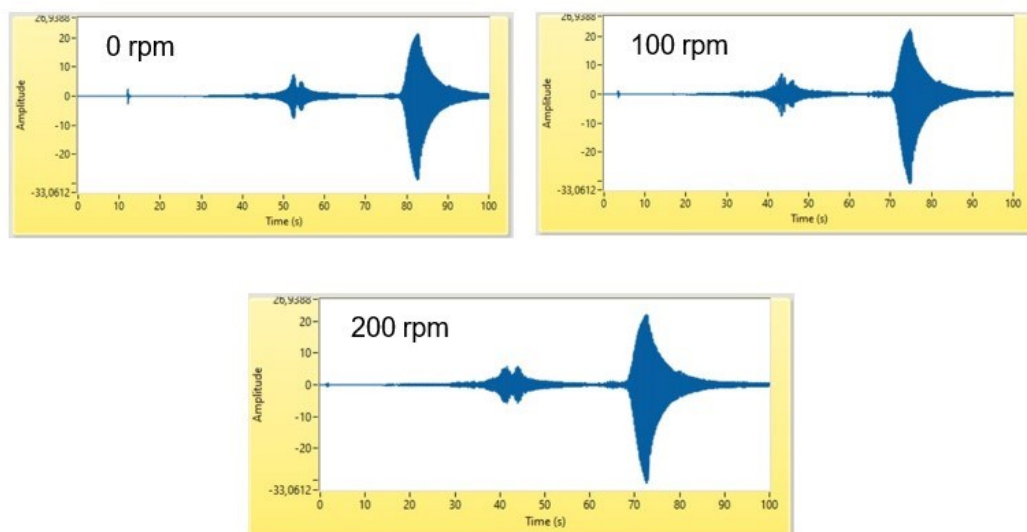


**Figure 62** Temporal signal of the accelerometer for 0 rpm, 100 rpm and 200 rpm

From a theoretical approach, the rotational velocity must influence the natural frequencies of the disk, in particular, a forward mode increases the natural frequency instead a backward mode decreases the natural frequencies for each mode, remembering that every mode presents two modes with the same value and each one undergoes the same influence. In the figures below the (+) is the forward mode that increases the value with the increase of the velocity while the (-) in the backward mode decreases the value. From the previous analysis in LabVIEW, it is possible to confirm that the rotation affects the frequency at least in the laboratory.

As aforementioned, to compare the laboratory test and the simulation it is necessary to add a rotational velocity inside the corresponding tool in Ansys and define the components of the rotational velocity for each value.

The values of the frequency obtained for each modes shape are compared in the figures below.

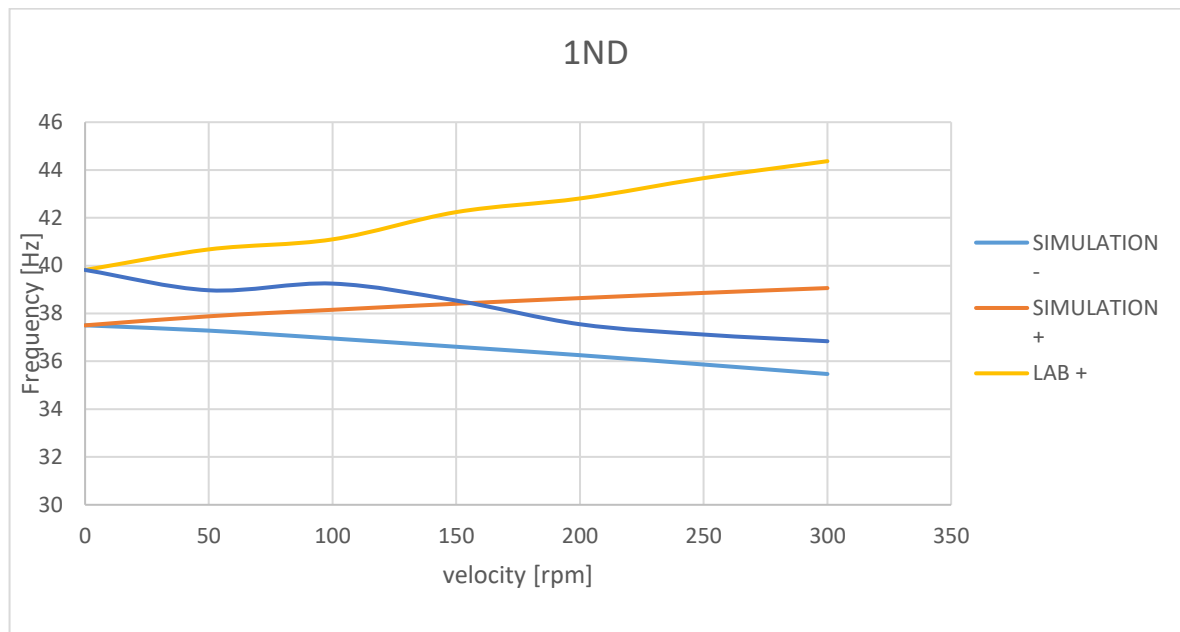


**Figure 63** Influence of the rotation on the frequency in the laboratory and simulation for the 1ND

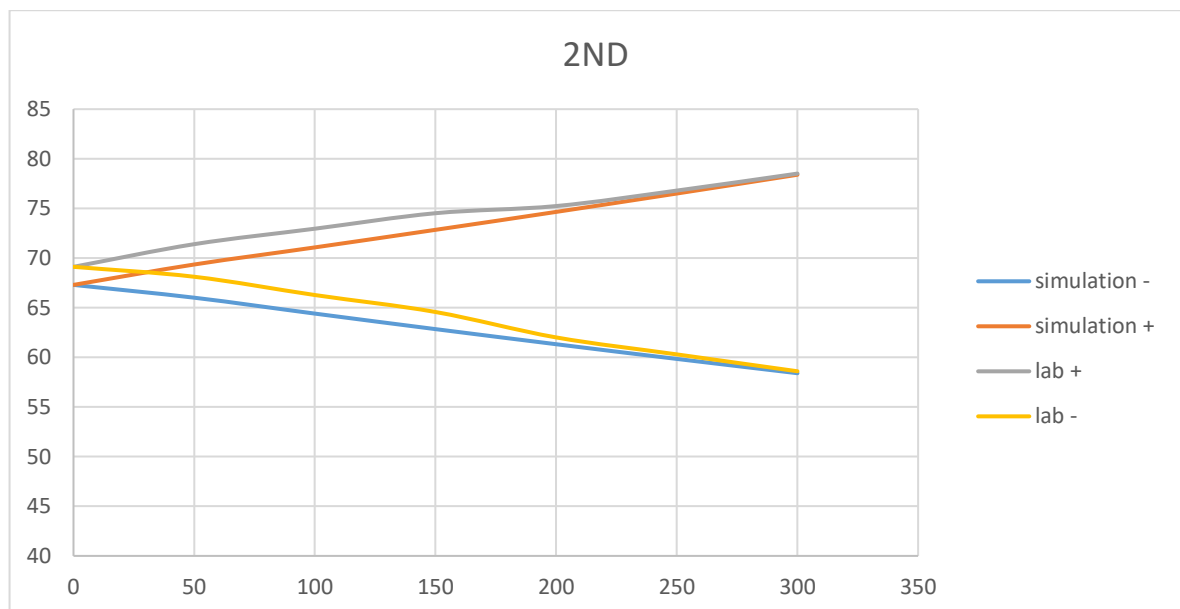


**Figure 64** Influence of the rotation on the frequency in the laboratory and simulation for the 2ND



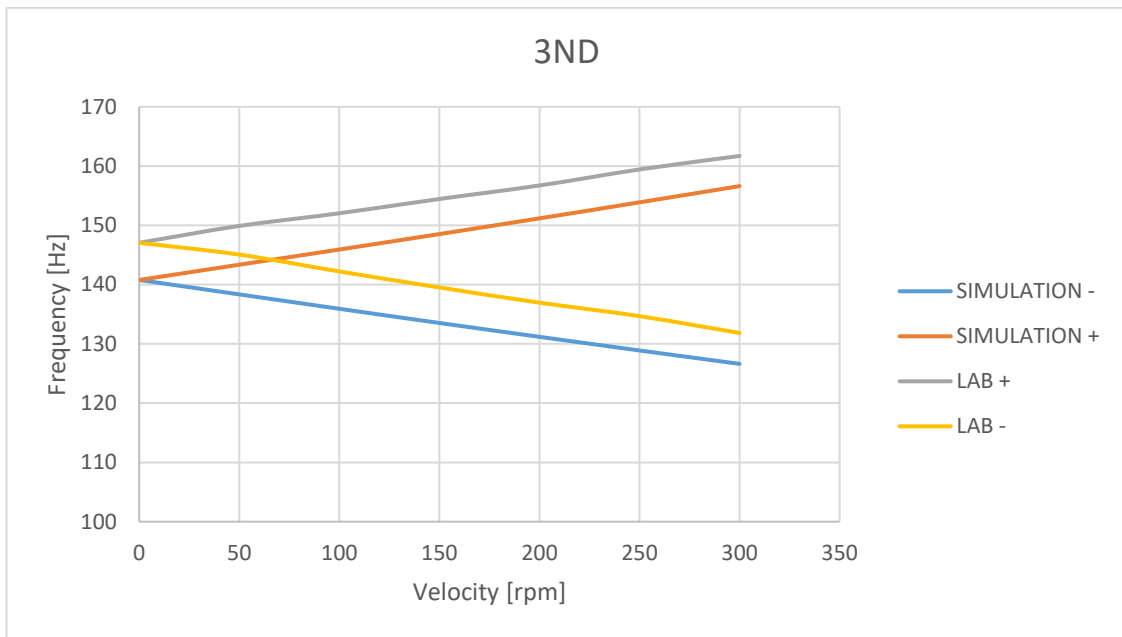


**Figure 65** Influence of the rotation on the frequency in the laboratory and simulation for the 3ND

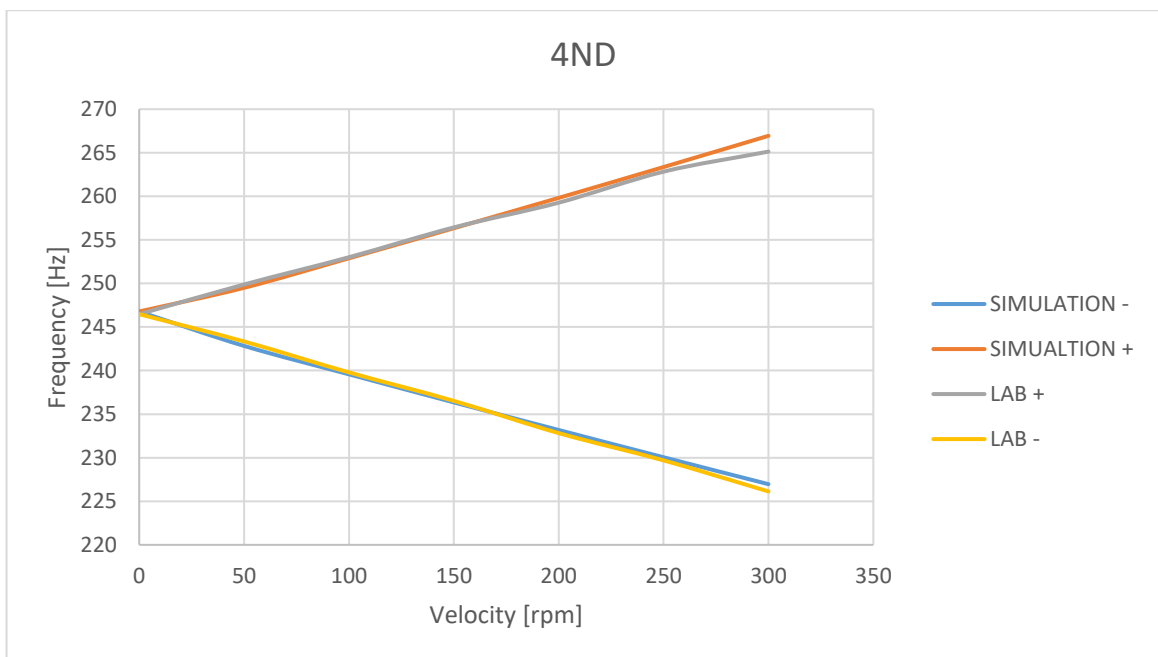


**Figure 66** Influence of the rotation on the frequency in the laboratory and simulation for the 4ND

As it is possible to notice from the previous graph the rotational velocity has an influence on the frequency both in the laboratory and in the simulation, moreover, the trend lines in the laboratory and simulation are similar we have the same growth of the frequency with the increasing of the velocity, except form

some fluctuation in laboratory's data. This effect is given by the fact that the rotation generates a centrifugal force field whose net effect is an apparent increase in stiffness causing in turn an increase of the natural frequency with speed.

In particular, the higher the frequency and the more accurate the simulation and the correlation with the test results the 4ND shows the same evolution both for simulation and laboratory. The effect is the same both for a forward mode and for a backward mode.

An interesting phenomenon is that the increasing or decreasing of the frequency is higher at a higher speed with a linear trend. This phenomenon indicates that disk stiffening is more significant at higher speeds.

	LABORATORY				SIMULATION		
	0rpm	300rpm	DIFFERENCE [%]		0RPM	300RPM	DIFFERENCE [%]
1ND	39,82	44,37	4,55		37,5	39,06	1,56
2ND	69,12	78,52	9,4		67,3	78,39	11,09
3ND	147,06	161,71	14,65		140,78	156,62	15,84
4ND	246,47	265,13	18,66		246,78	266,64	19,86

**Table 20** Increasing the frequency from 0 rpm to 300 rpm

As possible to observe in **Table 20**, the increase of the frequencies is higher when higher is the natural frequencies, which means that the effect of the velocity is much more intense at high frequencies. Moreover, except for the 1ND, the other mode shapes present almost the same increase both for laboratory and simulation.

This part concludes all the experiments on the disk in air, the model is well-modeled, and it can detect all the frequencies as in the laboratory, moreover, the influence of the rotation has the same effect both in the laboratory and in simulation, with the same linear increase. To conclude this part, it is confirmed that the simulation of the model is in the air without and with the rotation.

In the next step, water is added to analyze its effect on the frequency and mode shapes.

## 6. SIMULATION IN WATER

The model has been simulated in air, now the project is focused on the effect of the water on the natural frequencies and the mode shapes. The water must theoretically have an effect due to the added mass effect explained in chapter 3.4. To sum up, the added mass effect is a phenomenon that occurs when a fluid is in contact with a vibrating structure, the effect is that the structure behaves as if it has a larger mass than it does due to the presence of the fluid. This additional “added mass” results from the inertia of the fluid that is in motion relative to the structure.

To calculate the effect of the water it is necessary to add a tank full of water in which the disk is submerged for 20 cm under the free surface of the liquid. The dimensions of the tank are 600 mm in height and an internal diameter of 488 mm. The main structure remains the same as in the air and the sensors are in the same positions, the only difference is that the piezoelectric patch needs to be insulated from the water. Regarding the accelerometer and the strain gauges, both are designed to work submerged.

Once added the tank is sure that the model is the same as the one without the tank a fluid air is assigned to the surrounding acoustic elements and using the same boundary condition as in air are defined. The natural frequencies that are found are illustrated in the following table:

Mode shape (air)	Modal analysis	Modal acoustic	error
1ND	37,5	37,364	0,3%
0NC	57,3	56,751	0,95%
2ND	67,3	67,012	0,3%
3ND	140,78	140,44	0,24%
4ND	246,2	246,17	0,012%
1NC	329,34	325,89	1%
+1ND-1NC	354,29	351,31	0,84%

**Table 21** Comparison between the natural frequencies found in air (modal analysis) or with surrounding water (modal acoustic).

As it is possible to notice from the table, the natural frequencies of the mode shapes are the same in modal acoustic and modal analysis, which confirms that the acoustic-structural model is correct.

This analysis was performed to correlate the results found with the model in the air with the new model in water, but for matching the laboratory results in water with the simulation it is necessary to define new boundary conditions because the condition, such as the position of the bearings, are changed compared with the ones in the air, the new parameters defined are described in chapter 4.2.2.

As aforementioned, the disk is submerged for 20cm under the water, and the resulting FRF extract from LabVIEW is performed for different ranges of frequency 100-200Hz and 200-300 Hz applying a chirp voltage with a maximum amplitude ranging that goes from 400V to -100V. In this case, is used the FRF because the signal is clearer than the FFT, the FRF is defined as the ratio of the complex output amplitude to the complex input amplitude for a steady-state sinusoidal input, for obtaining the SFR has to be normalized considering the input voltage of the system (V) in the frequency domain. The equation of the FRF is the following one:

$$FRF = Magnitude * e^{j*Phase} = \frac{Amplitude_{strain} * e^{j*Phase_{strain}}}{Amplitude_{voltage} * e^{j*Phase_{voltage}}} \quad 6.1$$

The results are presented in **Figure 67** and **Figure 68** where it is possible to compare the signal obtained from the accelerometer and strain gauges. It is clear in this case that the strain gauge is more accurate being able to detect all the mode shapes inside the range 0-100Hz, instead, the accelerometer does not detect the mode shapes. The accelerometer shows two peaks determined by the noise of the signal; they are not mode shapes.

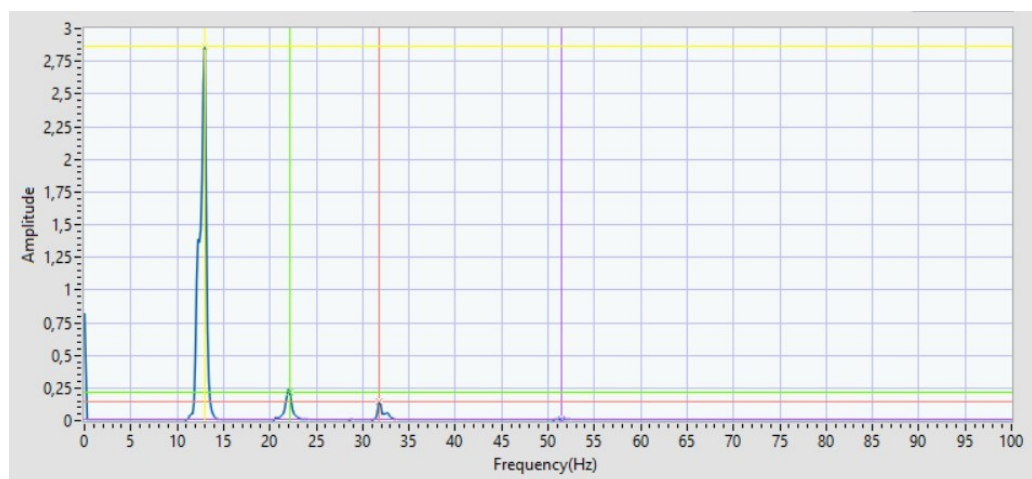


**Figure 67** FFT obtained for the SG8 (real geometry) in water

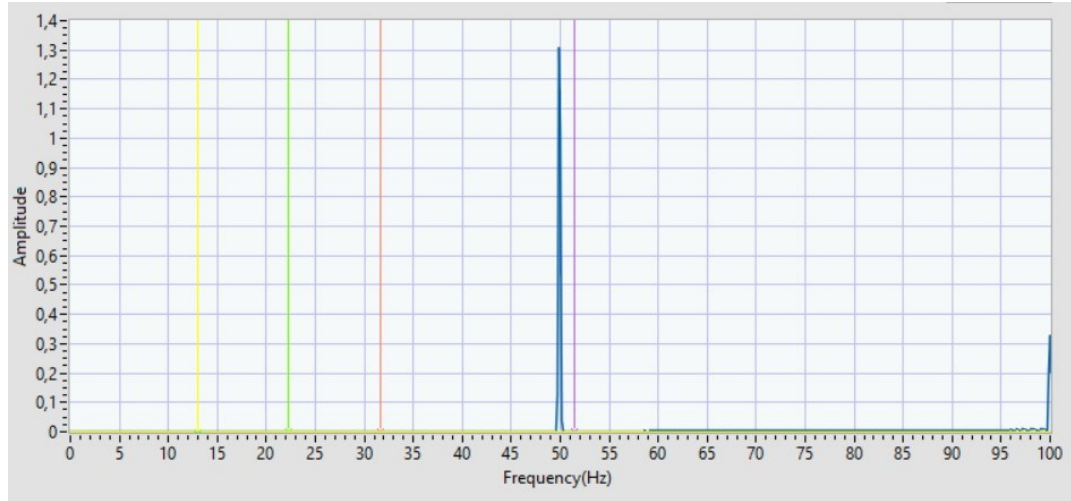


**Figure 68** FFT obtained for the accelerometer (real geometry) in water

Collecting the data using the chirp signals of different frequencies, the natural frequencies for the experimental test are obtained and compared with the simulation results. During the next steps, the simulation is performed using modal acoustic analysis to find the mode shapes and the natural frequencies and harmonic acoustic analysis to obtain the strain frequency response.

To highlight the drop of the frequency from air to water and to quantify the added mass effect induced by the water it is calculated the FRR, that is the percentage of frequency reduction from air to water, the equation is the following one where  $f$  is the value of the natural frequency :

$$FRR = \frac{f_{air} - f_{water}}{f_{air}} * 100 \quad 6.2$$

The results for the first seven mode shapes in the simulation are listed in the following **Table 22**, it is presented a range of FRR that goes from a minimum of 47,42% to a maximum of 70,66%. Regarding the FRR it is possible to notice that it decreases as the number of the nodal diameters increases, this phenomenon is produced because the deformation of the mode shapes moves less water than before, in fact increasing the frequency the deformation of the disk is less intense than the first mode shapes. Moreover, the FRR in the NC is higher than the ND, for example, the FRR of the 0NC is the highest while the FRR of the 1NC is higher than the FRR of the 4ND, which could be related to the fact that the added masse effect affects the most the NC mode shapes due to a higher axial movement of the disk.

Mode Shape	AIR_Laboratory [Hz]	WATER_Laboratory [Hz]	FRR [Hz]
1ND	39,82	13,1	67,10%
0NC	41,24	12,1	70,66%
2ND	69,12	22,04	68,11%
3ND	147,06	51,77	64,80%
4ND	246,47	128,85	47,72%
1NC	277,05	136,82	50,62%
1NC1ND	292,27	122,60	58,05%

**Table 22 FRR from laboratory results between air and water**

### 6.1.1. Modal acoustic

Like the first step performed in the air, it is necessary to determine the natural frequencies of the system and the corresponding mode shapes. In this case, the problem is the presence of water which calls for the definition of a fluid zone to take the water into account in the simulation. From a theoretical approach, a drop in the frequencies must be found due to the AVMI.

As in the simulation in the air, the mode shapes produced by the torsion and by the bending of the shaft are not considered to focus the analysis on the structural response of the disk, moreover, only the first seven mode shapes are analyzed to reduce the time of analysis. As in the air, every mode shape is composed of two identical mode shapes but with an angularity shift of  $\frac{\pi}{2n}$ , to simplify the analysis they will be treated like one mode using a mean value.

The mode shapes obtained, and the corresponding frequencies are in the following figure:

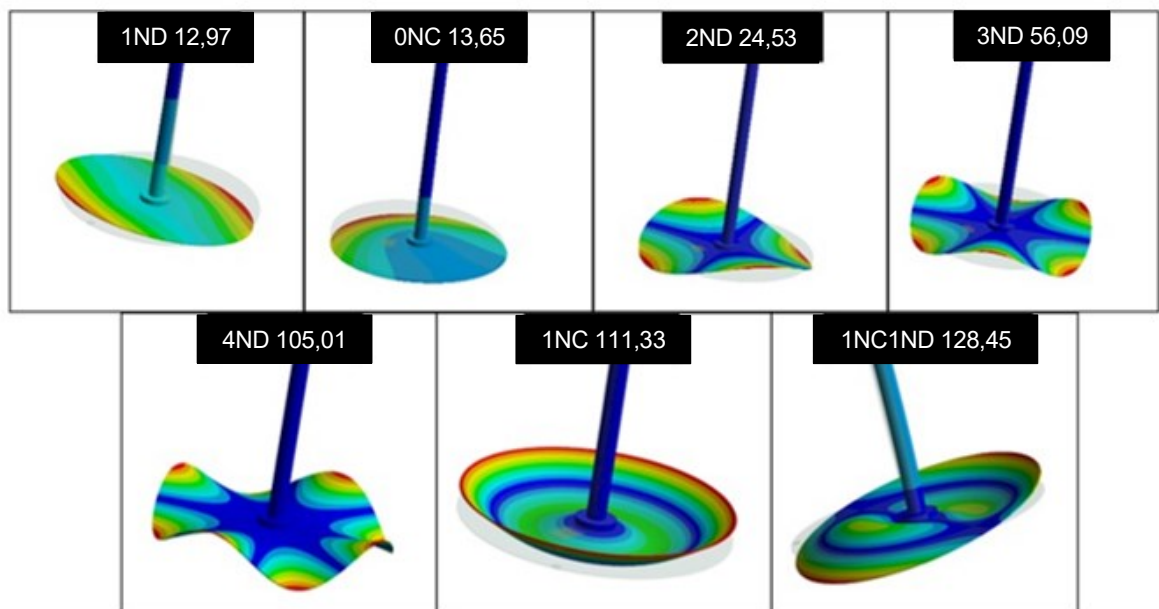


**Figure 69** First seven mode shapes of the disk in water

The first seven mode shapes illustrated in **Figure 69** are in order from the first to the sixth from top to bottom: 1ND, 1NC, 2ND, 3ND, 4ND, 1NC1ND. The table below it is compared the frequency measured in the laboratory and the frequency obtained in the simulation and it also calculated the differences between these two frequencies. The differences are around 10% for the 0NC and 2ND, while for the 1ND, 3ND, and 1ND1NC it is under 10% which means that they are well-modeled by the simulation, while the differences for the 4ND and 1NC are bigger than 20%. Regarding this huge deviation probably it is linked to the fact that the boundary conditions defined are correct for the mode shapes whose error is under 10% but not for these two modes, in fact probably because the distance between the bearings and the disk has been changed during the test compared with the one in air. This

new configuration in the test could not match exactly the new boundary conditions that are fixed. Moreover, the complex pattern of vibration belonging to the disk could affect the value of the deviation.

mode shape	Simulaiton [Hz]	Laboratory [Hz]	ERROR [%]
1ND	12,97	13,1	0,99%
0NC	13,628	12,1	11,21%
2ND	24,533	22,0444	10,14%
3ND	56,093	51,77	7,71%
4ND	105,01	128,85	18,50%
1NcC	111,33	136,82	18,63%
1NC1ND	128,45	122,60	4,55%

**Table 23** Comparison between the natural frequencies in laboratory and in simulation

To emphasize the low deviation obtained and the similarity of the trends, a graph was created in which the natural frequencies are compared as the mode shape increases. The mode shapes are in order as in

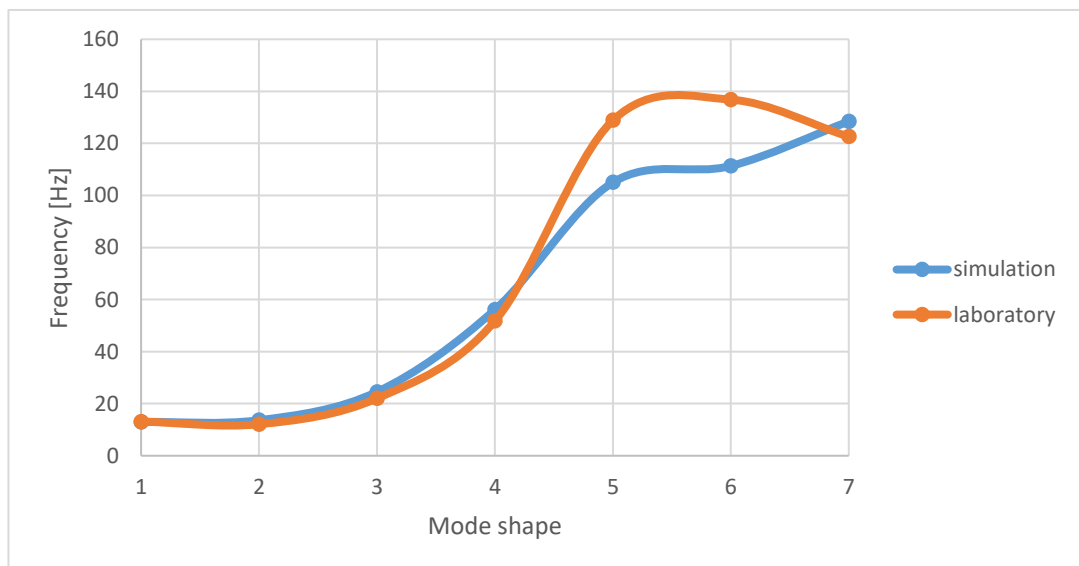


**Figure 70** Trends of natural frequencies in water obtained in laboratory and simulation where 1ND is the 1, 0NC is the number 2 and so on, the 1NC1ND is the last (number 7).

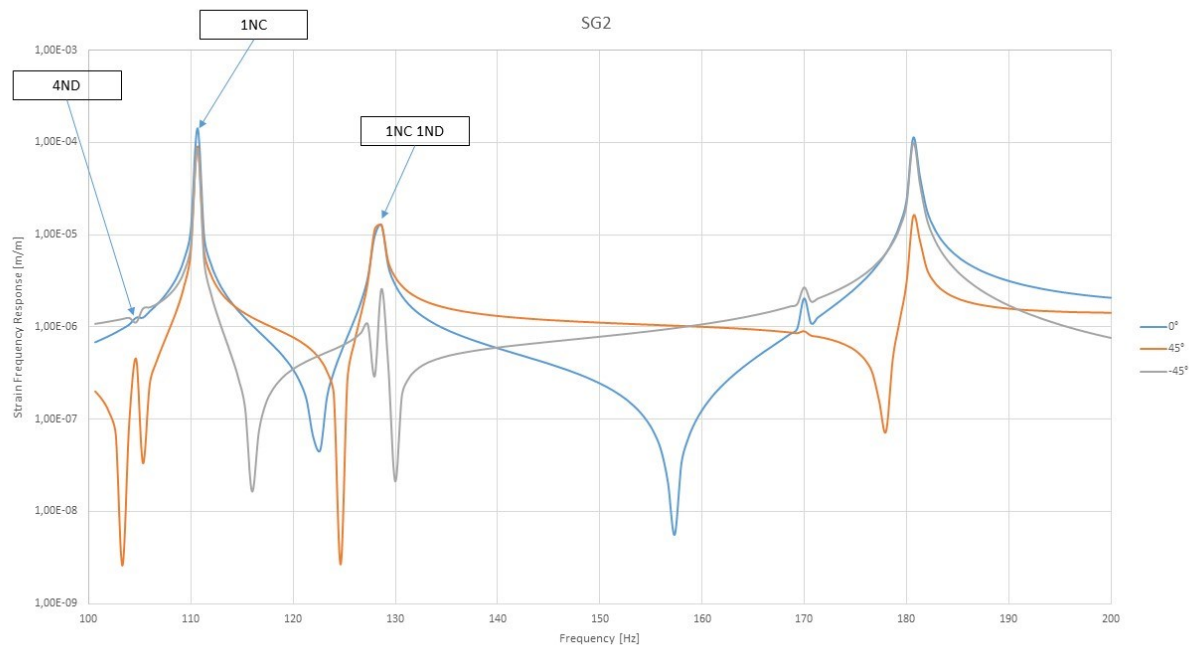


### 6.1.2. Harmonic analysis

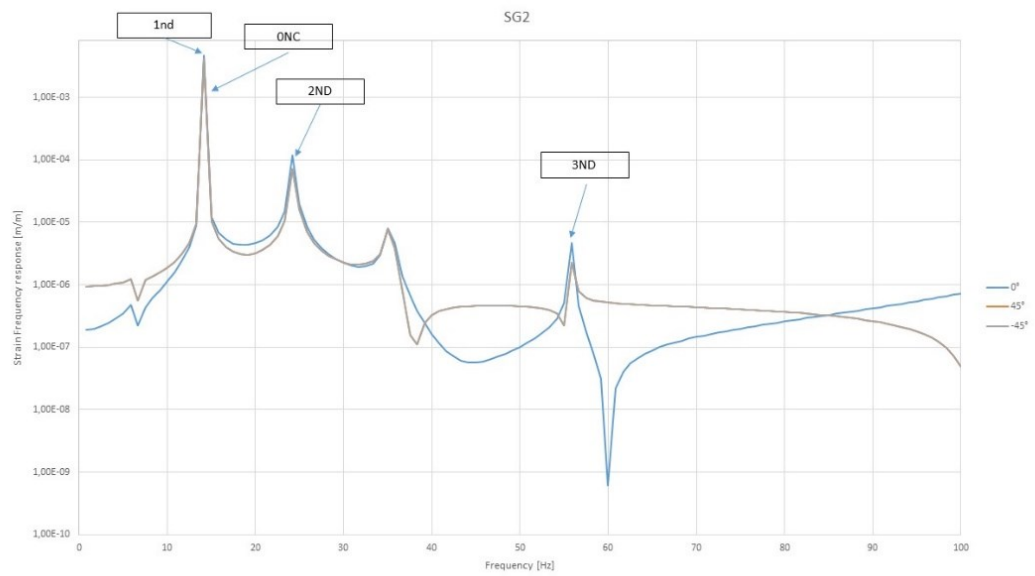
To obtain the frequency response of the strain gauges when the structure is submerged in water, Ansys's environment that must be used is the *Acoustic Harmonic Analysis*. The governing equation is the same as in the Harmonic analysis (3.5.2) but because there is an added mass effect ( $M_F$ ), the general equation is modified by adding a term, the added mass. The new equation that considers the added mass effect is (3.33).

The curves are illustrated in **Errore. L'origine riferimento non è stata trovata.** for the range 0-100Hz and **Figure 72** for the range of 100-200 Hz, in these figures are shown only the SG2 while the graph of the other sensors are located in the Appendix D. The strain gauge can detect all the peaks corresponding to the natural frequencies found in the modal analysis and all the directions show almost the same amplitude, there are more peaks than the natural frequencies of the disk because, in addition to the disk mode shape, there are also the torsional mode and the mode related to the bending of the shaft that is not analyzed in this project. Additionally, the 1ND and the 0NC are very near the strain gauge is not able to separate the peaks of the two modes, while the signal obtained for the 4ND is lower than the other peaks. The signal obtained from the other Sg is similar to the one acquired by the SG2 there are the same peaks, and also the signal is similar in all three directions.

#### RANGE 0-100Hz



**Figure 71** Peaks of the amplitude for the SG2 in the range of frequency 0-100Hz

**RANGE 100-200Hz**

**Figure 72** Peaks of the amplitude for the SG2 in the range of frequency 0-100Hz

## 7. COMPARISON BETWEEN THE STRUCTURAL RESPONSE IN AIR AND WATER

In the following chapter, the results collected from the simulation in air and water are compared there must be a difference between these two simulations, in particular, the natural frequencies in water must be decreased due to the added mass effect.

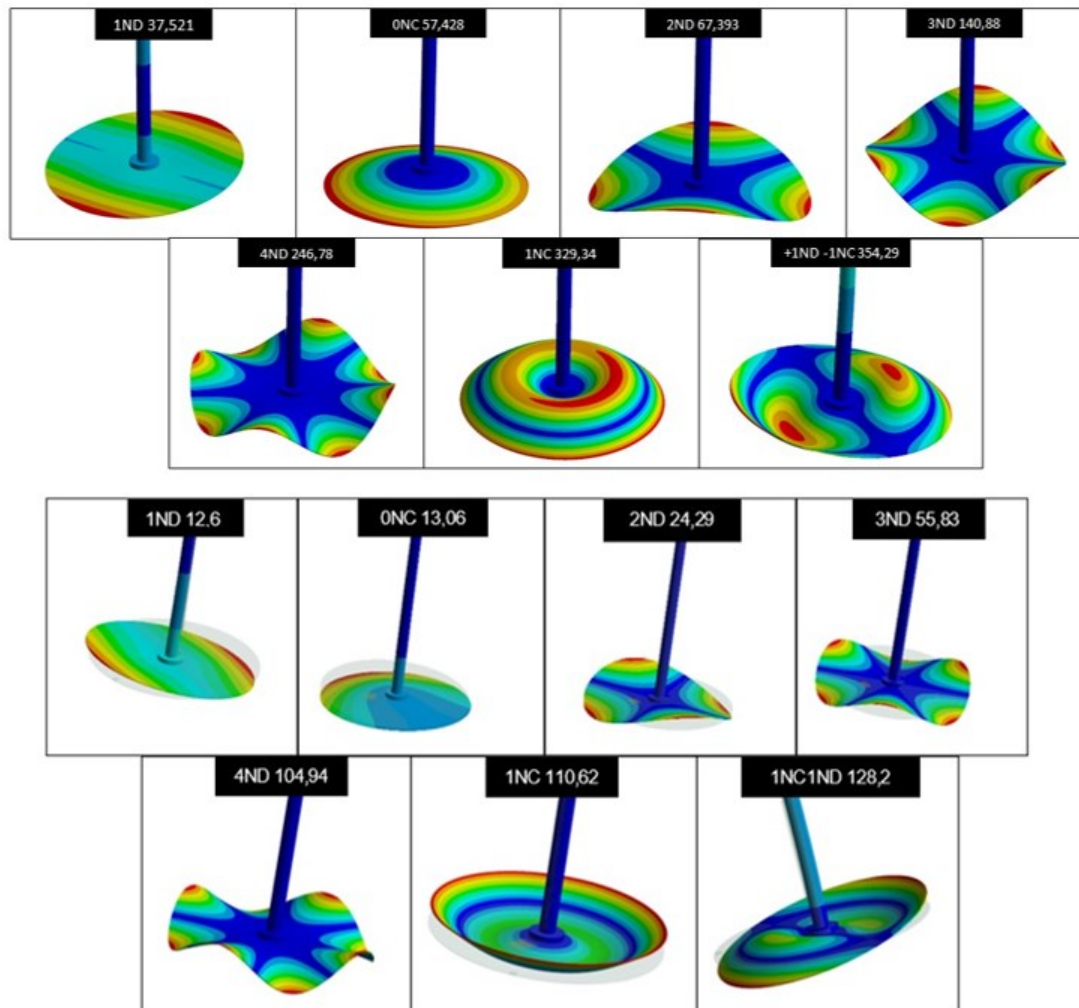


**Figure 73** Comparison between the modal shape in the air on the top and water on the bottom

Firstly, it is possible to observe from the previous figure that the mode shapes are the same except for the 0NC which does not present the typical deformation of this mode as in the air. The main difference is the frequencies at which they appear it is possible to notice a drop in the frequencies at which the mode shapes appear due to the added mass effect which creates a mass surplus to the system and decreases the natural

frequency, as explained in chapter 3.4.

To highlight the drop of the frequency from air to water and to quantify the added mass effect induced by the water in the following **Table 24** it is calculated the FRR, that is the percentage of frequency reduction from air to water, the equation used to calculate the FRR is the [6. 1].

For the first seven mode shapes in the simulation, we have a range of FRR that goes from 57,35% to 76,22%. Regarding the FRR it is possible to notice that the percentage of drop decreases when the number of the nodal diameters increases, this phenomenon is produced because the deformation of the mode shapes moves less water than before, in fact increasing the frequency of the deformation of the disk is less intense than the first mode shapes.

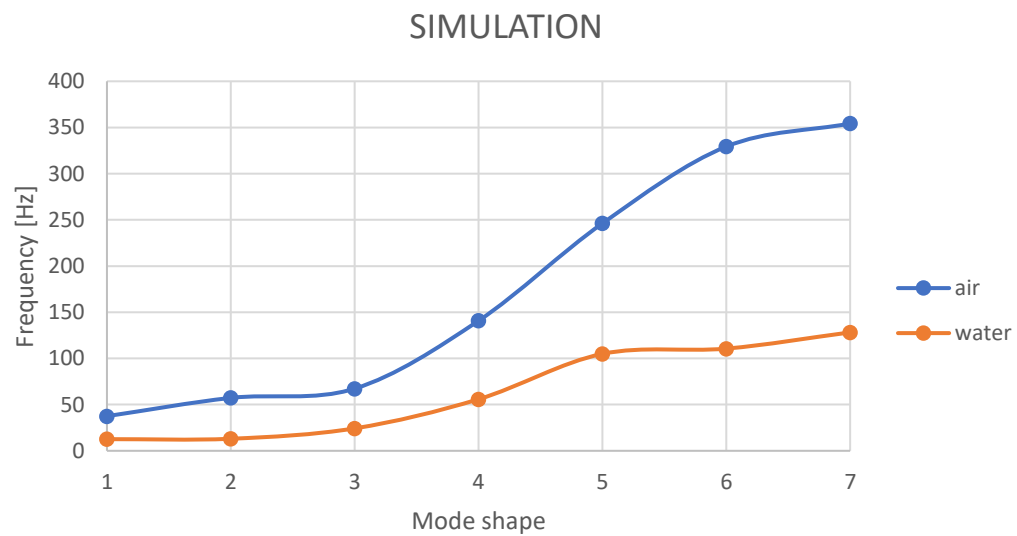
In addition, the column *WATER\_THEORETIC* in **Table 24**, presents the calculation of frequencies in water with the FRR of the simulation but starting from the air frequencies of the laboratory, this was done to highlight the difference between the simulation and test, in particular, to find what should have happened in the tests with the values of the FRR in simulation.

Comparison between air and water									
	air [Hz]	water [Hz]	FRR [%]		AIR_Laboratory [Hz]	WATER_THEORIC [Hz]	WATER_Laboratory [Hz]	FRR [%]	ERROR [%]
1ND	37,5	12,97	65,41%		39,82	13,77	13,1	67,10%	0,99%
0NC	57,3	13,628	76,22%		41,24	9,81	12,1	70,66%	11,21%
2ND	67,3	24,533	63,55%		69,12	25,20	22,04	68,11%	10,14%
3ND	140,78	56,09	60,16%		147,06	58,59	51,77	64,80%	7,70%
4ND	246,2	105,01	57,35%		246,47	105,13	128,85	47,72%	18,50%
1NC	329,34	111,33	66,20%		277,05	93,65	136,82	50,62%	18,63%
1NC1ND	354,29	128,45	63,74%		292,27	105,96	122,60	58,05%	4,56%

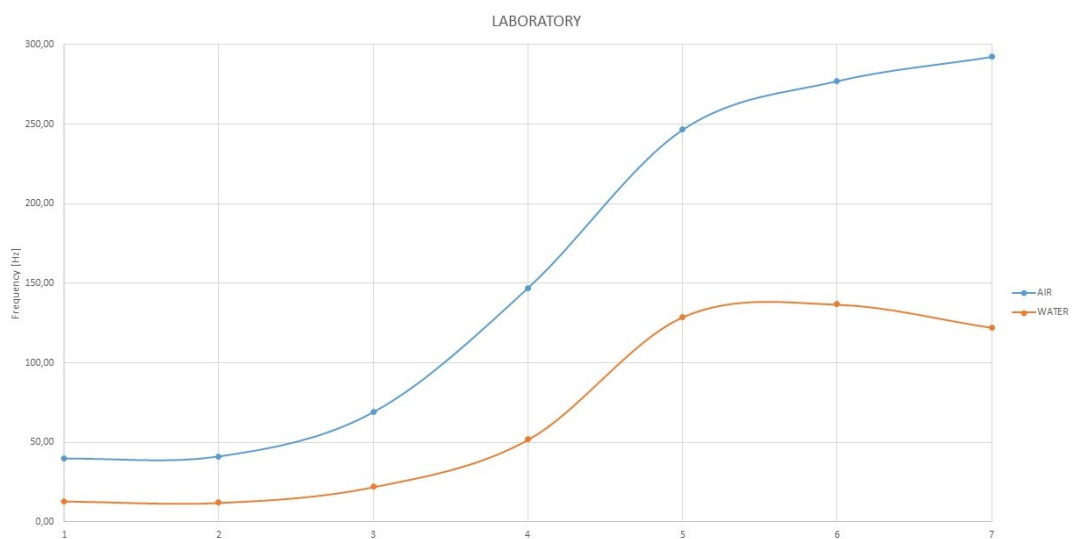
**Table 24** Comparison between the frequency in air in water

From the previous results, it is clear that the mode shapes have not undergone a change from water except for the 0NC. The FRR represents the effect of the AVMI on the modal response of the disk, to compare the trend of FRR in simulation and laboratory is useful to use some graphs, in fact using the graphs it is possible to observe the trends of the natural frequencies obtained in the laboratory and simulation, and comparing them to investigate the similarities. The Figures below (**Figure 75**, **Figure 74**, **Figure 76**) is presented the comparison between the drop of the frequency in the laboratory and simulation, and the last picture has analyzed the trend of the average of the FRR both in the laboratory and in simulation.

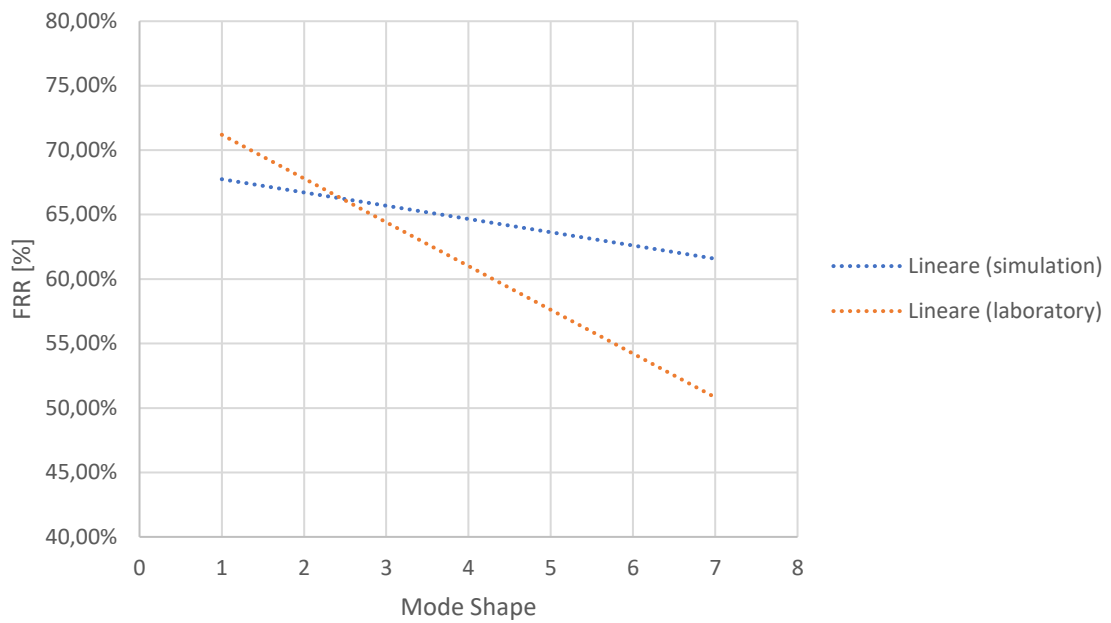
From the first two pictures, it is clear that the trend is similar except for the error already analyzed there is a widening of the curves when the number of the mode shapes increases, which could be in contrast with what was said before but looking at the last figure it is possible to notice that the trend of both tendency lines tends to decrease and move toward an asymptote at a higher number of mode shape, in fact looking at the NC group and ND group separately it is possible to notice that when the frequency increases the FRR decreases because the movement of the disk is less intense and is moved less water. These results confirm that when the frequency increases the effect of the added mass is less intense in percentage terms.



**Figure 75** Trend lines of the frequency in air and in water for the simulation test



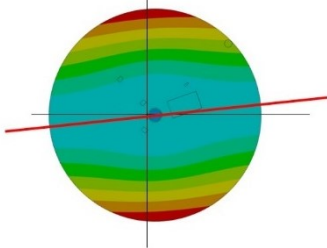
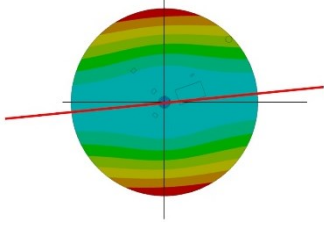
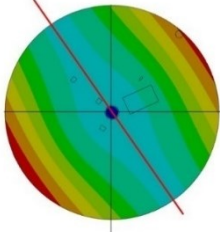
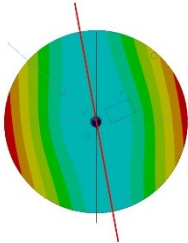
**Figure 74** Trend lines of the frequency in air and in water for the laboratory test



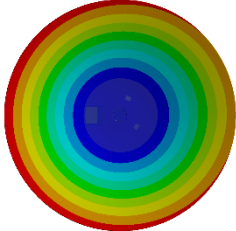
**Figure 76** Trend of FRR for both simulation and test

The effect of the water is not only decreasing the natural frequencies but has also an influence on the distance that decreases between different natural frequencies, in fact in the air for the laboratory the first mode shape is at 39,82 Hz and the last is at 292,27 Hz with a difference of 252,45 Hz, in water the first one is at 13,1 while the last one is at 136,82 Hz with a distance of 123,72 Hz. Moreover, the 1ND and 0NC have changed their positions from that found in the air the value of the 1ND is 13,1 and the value of the 0NC is 12,1, in simulation the situation is similar, although they have not changed position they are practically overlapping, the 1ND closer to the 0NC than in air. The effect is similar for the 1NC1ND and 1NC, in fact also, in this case, the mode shapes have changed their position in the laboratory, and as the first two mode shapes they are closer in simulation. Regarding this phenomenon and looking at the results it is clear that the water has a greater effect on the mode shapes characterized by the presence of NC and on the mode shape with both NC and ND despite having a higher frequency.

The next step is to compare the mode shape in the air and water to analyze the position of the nodal lines and to understand if the nodal lines are in the same position between the simulation in air and water. The following tables represent the nodal lines for the first seven mode shapes.

+1ND	
	
-1ND	
	

**Table 25** Comparison between the water simulation's nodal lines (left) and air simulation's nodal lines (right) for the 1ND

0NC	
Not available	

**Table 26** Comparison between the water simulation's nodal lines (left) and air simulation's nodal lines (right) for the 0NC

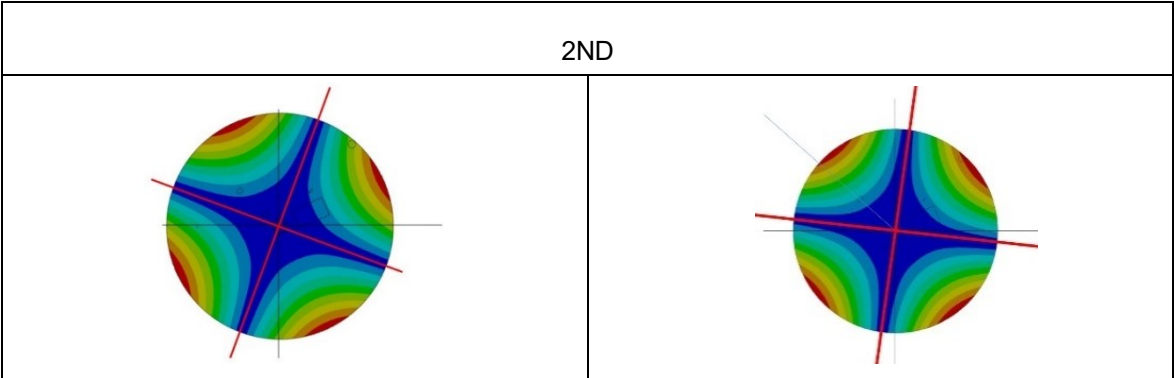


**Table 27** Comparison between the water simulation's nodal lines (left) and air simulation's nodal lines (right) for the 2ND

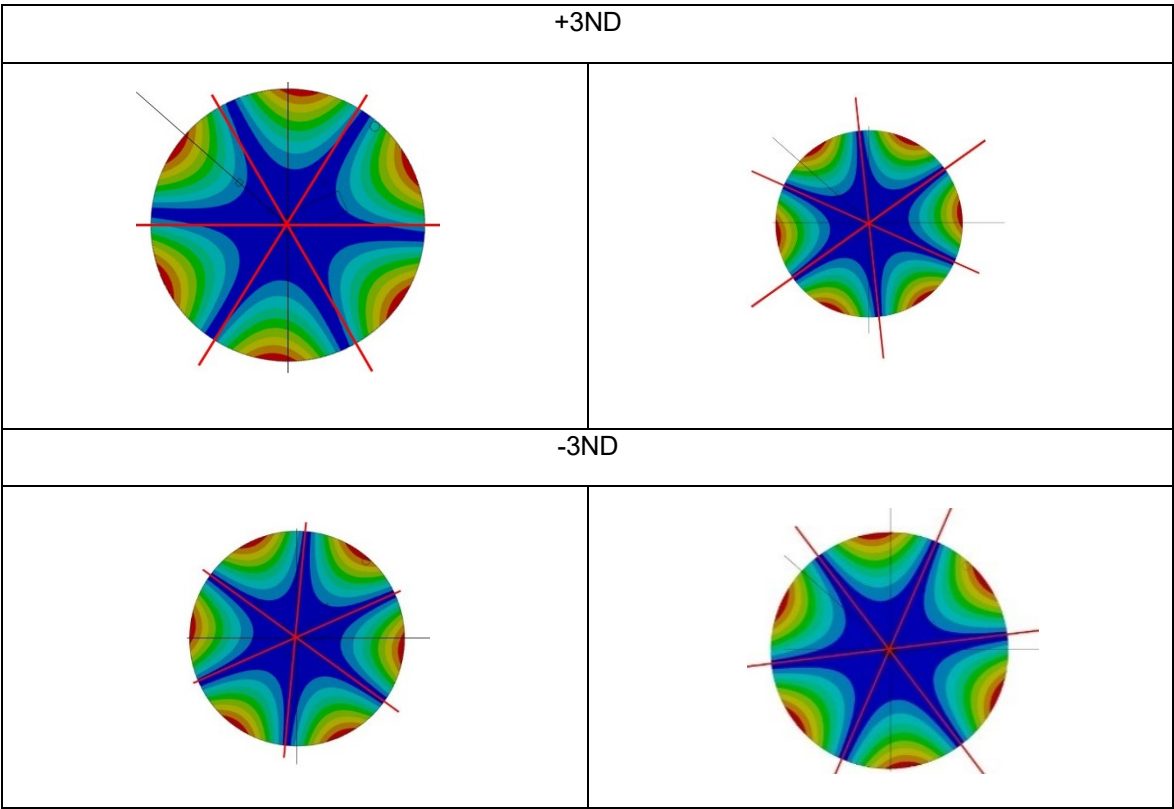


**Table 28** Comparison between the water simulation's nodal lines (left) and air simulation's nodal lines



(right) for the 3ND

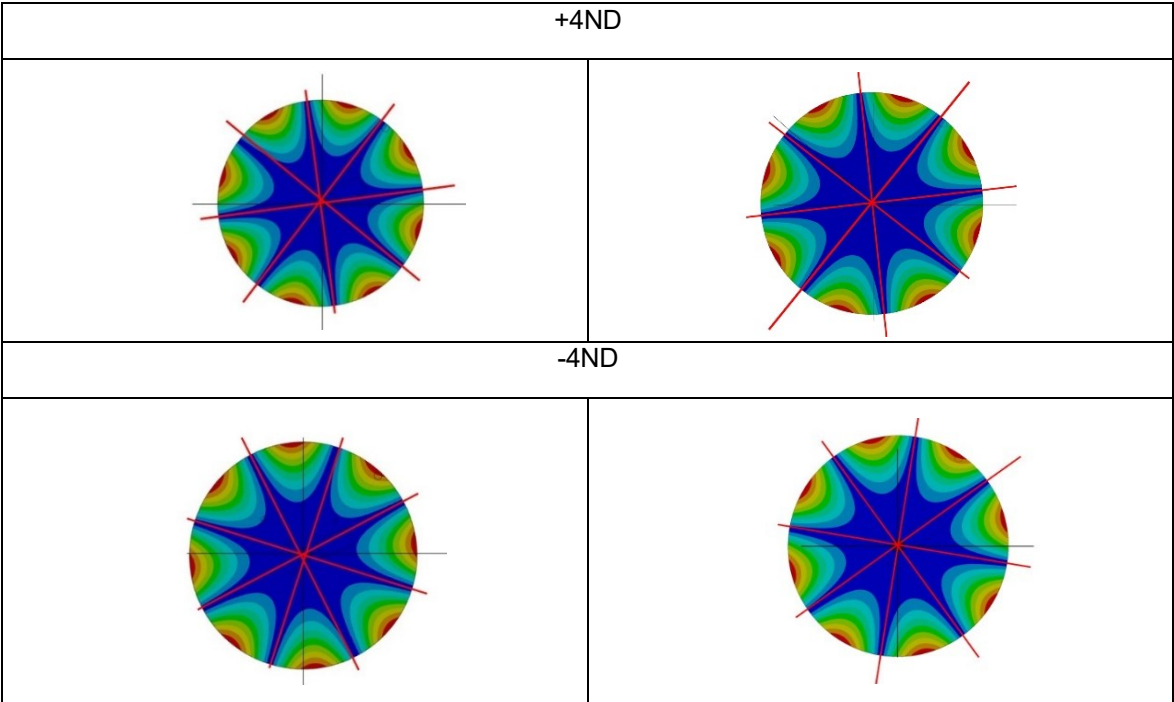


**Table 29** Comparison between the water simulation's nodal lines (left) and air simulation's nodal lines (right) for the 4ND

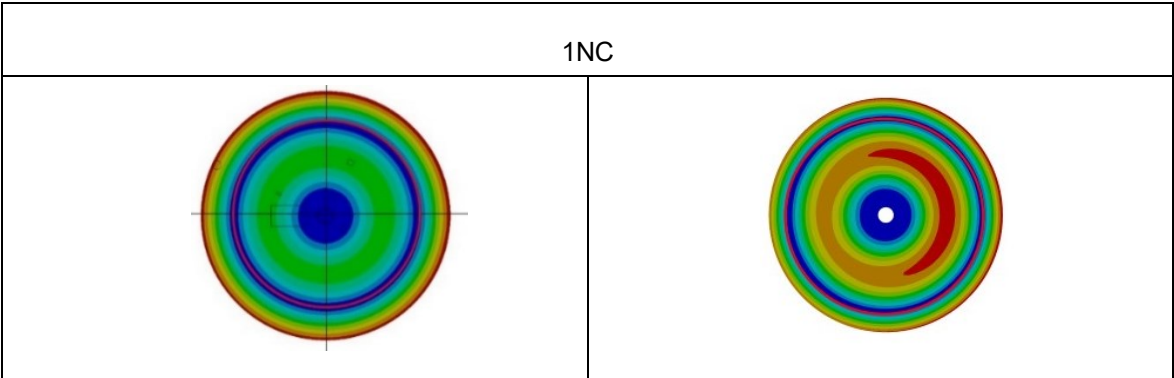


**Table 30** Comparison between the water simulation's nodal lines (left) and air simulation's nodal lines (right) for the 1NC

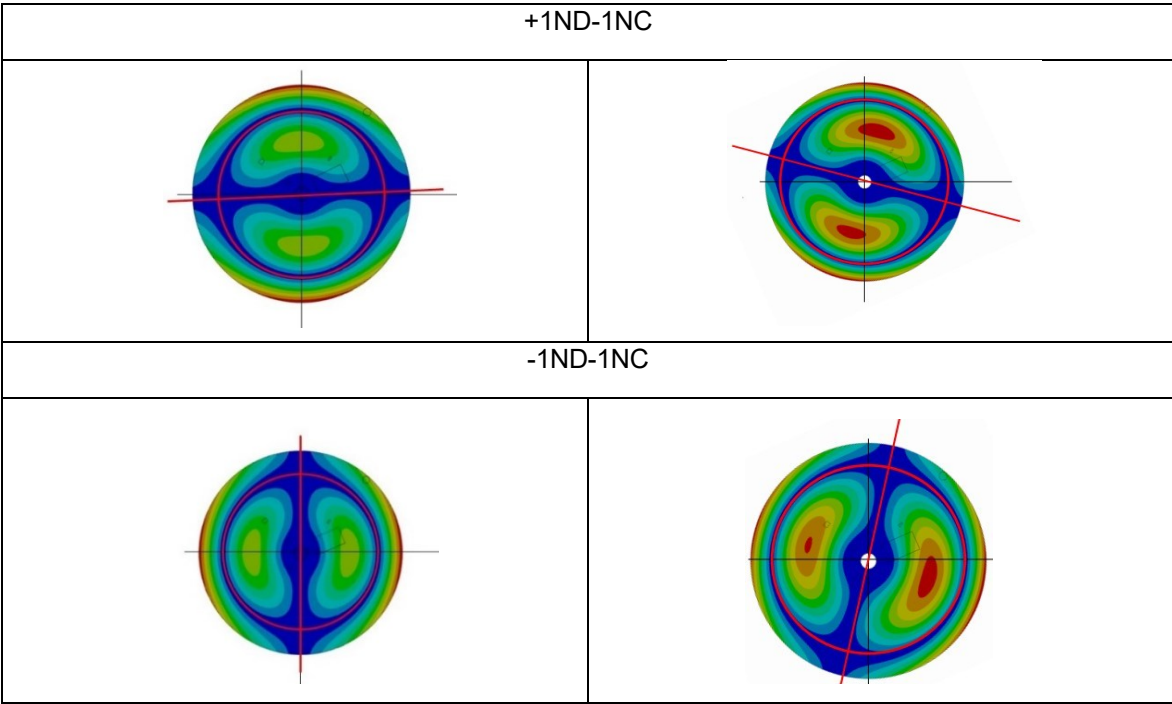


**Table 31** Comparison between the water simulation's nodal lines (left) and air simulation's nodal lines (right) for the 1ND1NC

From the previous comparisons, it is clear that the mode shapes are the same as in water but there is a rotation between the nodal lines in the water and air, especially for the ND lines, in particular, the difference is higher for the first mode shapes, and it decreases when the frequency increases. The situation changes for the nodal rings that have the same dimension both in water and air. The difference between the ND in water and air could be brought back to the new boundary conditions that were necessary to define due to the new configuration of the structure with the tank.

In conclusion, the curves of the strain frequency response are put in the same graph to observe how the peaks are shifted by the effect of the presence of the water.

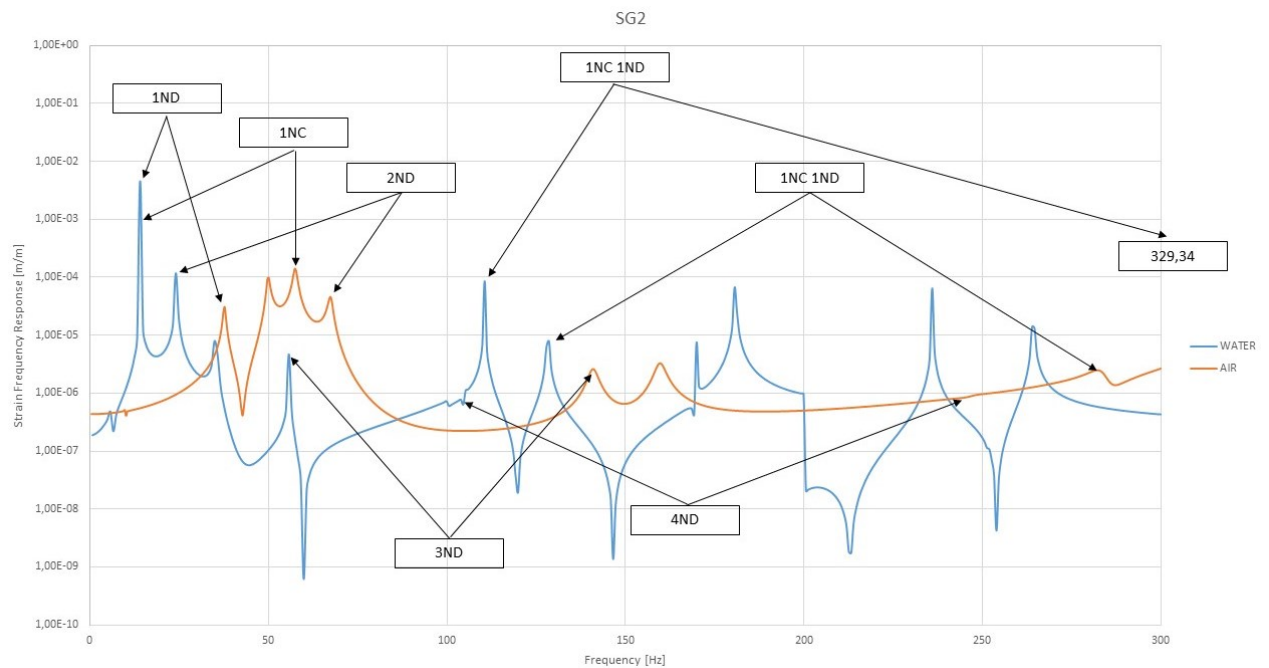


**Figure 77** Comparison between the strain peaks in water and in air

**Figure 77** shows the peaks of the amplitude for the model in the air and the model in water. There are several peaks due to the presence of the torsional mode shapes and due to the shaft bending but looking only at the disk mode shapes it is clear that all the mode shapes are shifted due to the presence of the water. This graph confirms the fact that the water has an effect on the mode shape and also that the model can capture this influence and create a behavior similar to the laboratory results, especially for some mode shapes. The 0NC, the 1NC and are not well detected by the model, probably due to the new boundary condition necessary to adapt the geometry to the new conditions in the water.

To summarize this chapter, as theoretically supposed the water affects the structural response of the disk, in particular, the mode shapes are the same as in air except for the 0NC, the difference is in the value of the frequency at which they appear because the water decreases the value of the frequency. All the analysis confirms the presence of the influence of the water and that the model can simulate correctly the structural response of the disk in water.

## 8. Project Plan

To have an idea of the time spent on the project and all the steps the project plan is illustrated in the Gantt diagram in **Table 32**. The different tasks are labeled on the left of the diagram and are assigned to the different weeks scheduled. The project takes 20 weeks from the middle of September to the middle of February.

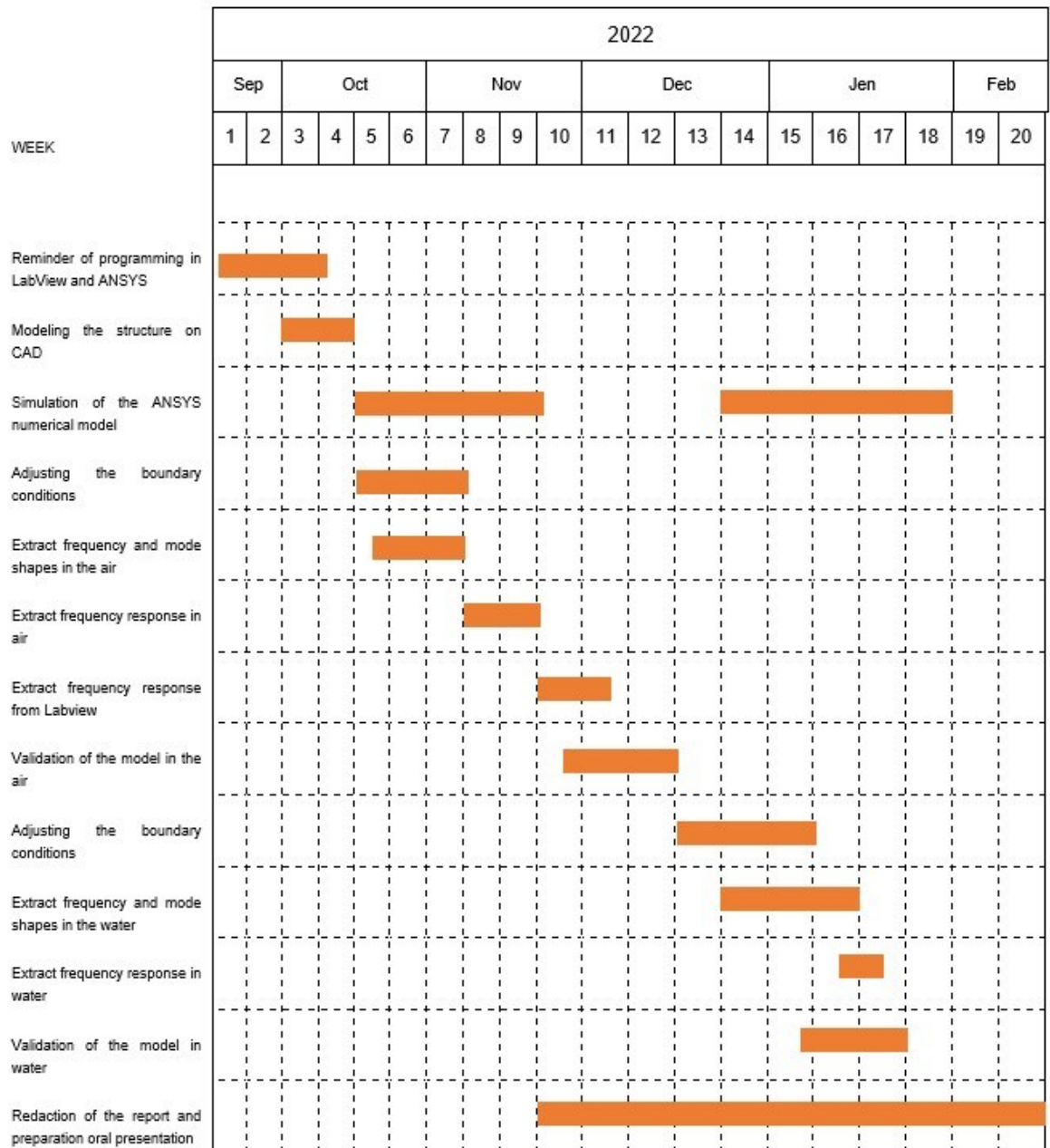


**Table 32** Gantt diagram representing the project plan

## 9. Budget

In this chapter, the budget of the project is analyzed in **Table 33**, in which there is a list of the different costs that take part during the project. First of all, the cost of the engineer who is in charge to develop the project, the average salary for the engineer is 15 €/h. The duration of the project is 20 weeks, from the middle of September to the middle of February, assuming an average of a worked hour of 40h/week (8h/day for five days a week), and the total of the worked hours is 800h.

Moreover, the project must be supervised by two doctors from the university, so the worked hours used by them to supervise the project must be considered. Considering 2h/week and 20€/h for one doctor.

Additionally, not only the work of the people must be considered there are several support services such as the office material, electricity, and internet connection. For the office material is considered a cost of 50€ for the duration of the project, instead, for the electricity and the internet it is considered all the amount of worked hours, the electricity includes not only the computer but for all the lights and all the devices of the office. Considering the last price of the electricity of 0,361€/kWh and considering 1,5kW per hour, the total cost will be 0,5415 €/h. Moreover, the amortization of the computer is calculated considering 25% of annual amortization. The computer was bought for 1500€, with an amortized cost of 375€/year, the amortization for the duration of the project is 156,25€.

Finally, all the costs of the software must be considered by annual subscription, the license must be paid for the year even if the duration of the project is 5 months. Summing the cost and adding an extra cost for the "IVA", the total budget of the project amount to 24002,43€.

	Unit	Cost per unit	Total cost
<b>Technical and support services</b>			
Technical engineer	800 h	15 €/h	12000 €
Doctors of the university (supervisors)	80 h	40 €/h	3200 €
Electricity consumption	800 h	0.5415 €/h	433,2 €
Internet connection	5 months	30 €/month	150 €
<b>Research Material</b>			
ANSYS license software	1 year	4,000 €/year	4,000 €
LabVIEW license software	1 year	3,523 € / year	3,523 €
<b>Research Equipment</b>			
Amortization of the laptop	5 months	375 €/year	156,25 €
Office material	-	-	50 €
<b>Total without taxes:</b>			19836,72€
VAT ("IVA") 21 %			+4165,71
<b>Total budget:</b>			<b>24002,43 €</b>

**Table 33** Total Budget of the project

## 10. Environmental impact

Regarding the environmental impact of the project, the electrical consumption of the sensors and the computer used for implementing the controller must be considered.

On average, a laptop typically uses between 50 and 100 W/hour of electricity when it is being used, depending on the model. Concretely, the Lenovo Legion laptop used for this project has a power consumption of 57 W/hour. Considering that the laptop is used for the estimated 800 hours worked for this project, this represents a power consumption of around 44.69 kWh for performing the project, which also includes the time spent in the laboratory performing experiments. Depending on the type of fuel or energy source used to produce this electricity, as well as depending on the type and efficiency of electric power plants, it will be produced amount of carbon dioxide (CO<sub>2</sub>) to produce this electricity. As an averaged value, it is considered that in September 2021 is produced around 200 g of equivalent CO<sub>2</sub> per kWh of electricity in Spain, the value obtained from the "electricity map" interactive site. Therefore, to produce the 44.69 kWh needed for the laptop, it is going to be produced around 8.94 kg of CO<sub>2</sub>.

As no natural light arrives in the laboratory, is needed constant lighting to illuminate it and work in the test rig. This is considered to be supplied by a 40-Watt bulb equivalent compact fluorescent. Considering that the laboratory spent around 5 hours per week, this ends up with a total light consumption of 5.6 kWh, which is equivalent to producing, using the same CO<sub>2</sub> emission factors, 1.12 kg of CO<sub>2</sub>.

All in all, the total amount of CO<sub>2</sub> emitted for lighting the room and powering the computer is estimated to be around 13.880 kg of CO<sub>2</sub>.

To perform numerical experiments in the laboratory, apart from powering all the sensors and the computer used for the controller, is also needed to introduce water into the tank. The water introduced in the reservoir, which has a maximum capacity of 122 l of water, is not going to be polluted in the experimental process, so it can be safely dumped in the conventional sewage system without the need to treat it.

Finally, once the life span of the sensors and the computer used in the test rig ends, they have to be treated as Waste from Electrical and Electronic Equipment (WEEE). The EU has different rules on how to treat these WEEE to address environmental and other issues caused by the growing number of discarded electronics in the EU, which have some hazardous materials. Hence, these WEEE have to be collected and treated to recycle them, separating the hazardous components and reusing some

materials to create new electronic equipment.

## 11. CONCLUSION

This project has aimed to develop and validate a mathematical model, and to perform a simulation of the modal response of a disk in air, without and with rotation, and submerged in water.

Using simulation software the complex behavior of the disk predicted with the model has been compared with the laboratory tests obtained with a series of sensors and actuators. The same instruments have been considered and introduced in the CAD model. To excite the disk a piezoelectric patch has been used so that it has been possible to simulate an external load excited with an input voltage. The results obtained using the modal analysis and harmonic analysis tools of Ansys in the air have shown a good correlation between the results of the laboratory and the simulation. The same mode shapes have been obtained with low errors for the ND mode shapes while for the NC mode shapes the error has been higher, which means a good correlation for the ND modes and less for the NC modes. The confirmation that the model is capable of reproducing correctly the structural response in the air comes from the strain frequency response in which the peaks of amplitude are the same as those found in the laboratory test. Moreover, to complete the validation of the model a rotational velocity has been applied to analyze its effect of it on the natural frequency. It has been found that there are frequencies that are doubled and one of them increases with the rotation meanwhile the other decreases. The linear increase and reduction rates of these frequencies follow the same trend as the laboratory results.

The second part of the project has been focused on the changes of structural response observed when the disk is submerged in water predicted by using the modal acoustic and the harmonic acoustic tools of Ansys. The obtained results have shown a drop in the natural frequencies due to the added mass effect of the water as expected from a theoretical approach. Also, in this case, the ND mode shapes have been modeled more accurately than the NC models. In particular, a very large error has been found for the 1NC and for the 4ND modes which could be related to the influence of the rest of the test rig components such as the shaft, the bearings, and the beams of the supporting frame.

Hence, it has been possible to conclude that the model is good enough to validate the results in air and water although with the presence of some errors due to the complex behavior of the structure that is not influenced only by the disk but by all the components of the test rig. Moreover, the presence of a limited number of sensors on the test rig has reduced the number and quality of the results obtained with the tests and their comparison with the simulations. Therefore, it is concluded that in the future it would be better to have more sensors on the disk in different positions.

Starting from this analysis, future works will be focused on creating a mathematical model for a more complex structure like a complete hydraulic turbine unit to be able to predict its structural response out of the nominal operating point and submerged in water which currently presents a high degree of difficulty.





## Bibliografia

### Referències bibliogràfiques:

- [1] R. Basso, "Elementi di meccanica delle vibrazioni", Padova, libreria progetto
- [2] D Thorby, Structural Dynamics and Vibration in Practice. Amsterdam: Elsevier, 2008.
- [3] D. J. Inman, Engineering Vibration - second edition. Upper Saddle River NJ: Prentice Hall, 2000
- [4] OMEGA, [online] <https://www.omega.com/en-us/resources/accelerometers-types>
- [5] Zine Ghemari, Saad Salah, and Rabah Bourrenane, "Resonance effect Decreases and Accuracy Increase of Piezoelectric Accelerometer Measurement by Appropriate Choice of Frequency Range", Shock and Vibration, 2018  
[Resonance Effect Decrease and Accuracy Increase of Resonance Effect Decrease and Accuracy Increase of](#)
- [6] Vinayak Ranjan and M.K..Ghosh, "Transverse Vibration of spinning disk with attached distributed patch and discrete point masses using finite element analysis", International Journal of Engineering, 2009. Available: [58062-Article%20Text-102456-1-10-20100818%20\(1\)](#)
- [7] Barasch, S. and Chen, Y., 1972. On the vibration of rotating disk, American Society of Mechanical Engineers, Journal of Applied
- [8] Alexandre Presas, David Valentin, Eduard Egusquiza, Carme Valero, Ulrich Seidel, " Influence of the Rotation on the natural frequencies of a submerged-confined disk in water", Journal of Sound and Vibration, 2014,  
<https://reader.elsevier.com/reader/sd/pii/S0022460X14008475?token=DCE0D242B88941A3C6FE43D27AAF054217CA8A3FB4A0ECA9F3BB616909506041995DD5728ECE297513418FDB8DD7D3CB&originRegion=eu-west-1&originCreation=20230114144734>
- [9] Tokyo Measuring Instruments Lab, "Waterproof strain gauges". [Online], [https://tml.jp/e/product/strain\\_gauge/wf\\_list.html](https://tml.jp/e/product/strain_gauge/wf_list.html)
- [10] PI Ceramic, "P-876 duraact patch transducer", Februart 2021. [ONLINE], <https://www.piceramic.com/en/products/piezoceramic-actuators/patch-transducers/p-876-duraact-patch-transducer-101790/#description>
- [11] Anju V Nair, Abdul Rahman Mohd Kasim, Mohd Zuki Salleh, "Vibration analysis of circular plates in contact with fluid: A numerical approach", 2017, Faculty of Industrial Sciences and Technology, Lebuhraya Tun Razak
- [12] M.K.Kwak and K.C.Kim., "Axisymmetric vibration of circular plates in contact with fluid", Barcelona, Journal of Sound and Vibration, 1991.
- [13] Soft db, "understanding the vibrations and how they effect both structures and human", 2021,

- [online]. <https://www.softdb.com/understanding-vibrations/>
- [14] D. Valentin, A. Presas, E. Egusquiza and C. Valero, "Influence of the added mass effect and boundary conditions on the Dynamic Response of submerged and confined structures", in *IOP Conference Series: Earth and Environmental Science*, vol 22, 12 2014
- [15] H. Lamb, R.V. Southwell, The vibrations of spinning discs, *Proc. R. Soc. London* 99 (1921) 272–280.
- [16] A.S. Bouboulas and N.K. Anifantis, "Vibration Analysis of a Rotating Disk with a Crack", *International Scholarly Research Notices*. <https://courses.ansys.com/wp-content/uploads/2020/05/Lesson-5-Evaluate-Strain-Results.pdf>
- [17] N. Baddour, J.W. Zu, "A revisit of spinning disk model", University of Toronto, ScienceDirect. <https://reader.elsevier.com/reader/sd/pii/S0307904X00000664?token=8BE828993AEA1713873FAE7970A00EE280330641D82DEA24D7A8CA57951897A9A0F68B67F4EE2C93384DB4BAA0EB581D&originRegion=eu-west-1&originCreation=20221227092900>
- [18] Blevins R D, *Formulas for Natural Frequency and Mode Shapes*, 1979
- [19] W. Dziembowski and G. Kovacs, "On the role of resonances in double-mode pulsation", 1983
- [20] Richard K. Jones, "The Well-Tempered Timpani", [online], <https://wt.pauken.org/chapter-2/modes-and-nodes>
- [21] Peter Avitabile, *Experimental Modal Analysis*, Sound & Vibration Magazine, University of Massachusetts Lowell, Massachusetts USA [https://www.uml.edu/docs/s-v-jan2001\\_modal\\_analysis\\_tcm18-189939.pdf](https://www.uml.edu/docs/s-v-jan2001_modal_analysis_tcm18-189939.pdf)
- [22] ANSYS guide, "equivalent (von-mises) strain" [Online], <https://courses.ansys.com/wp-content/uploads/2020/05/Lesson-5-Evaluate-Strain-Results.pdf>
- [23] ANSYS guide, "principal strain", [Online], <https://courses.ansys.com/wp-content/uploads/2019/04/1.3.3-Principal-Stress--rebranded.pdf>
- [24] X. Huang, *Contribution to the Dynamic Response of Hydraulic Turbomachinery Components*, CDIF, UPC, Barcelona, 2011.
- [25] C.G. Rodríguez, E. Egusquiza, X. Escaler, Q.W. Liang, F. Avellan, Experimental investigation of added mass effects on a Francis turbine runner in still water, *J. Fluids Struct.* 22 (2006) 699–712.
- [26] Q.W. Liang, C.G. Rodríguez, E. Egusquiza, X. Escaler, M. Farhat, F. Avellan, Numerical simulation of fluid added mass effect on a Francis turbine runner, *Comput. Fluids* 36 (2007) 1106–1118.
- [27] H. Lamb, R.V. Southwell, The vibrations of spinning discs, *Proc. R. Soc. London* 99 (1921) 272–280.
- [28] A. Presas, D. Valentin, E. Egusquiza, C. Valero, U. Seidel, Influence of the rotation on the natural

- frequencies of a submerged-confined disk in water, *J. Sound and Vibration*. 337 (2015) 161-180.
- [29] MDPI, "Effect of boundary conditions on fluid–structure coupled modal analysis of runners." [Online].
- [30] COMSOL INC., "Piezoelectric materials: Understanding the standards," February 2021. [Online]. Available: <https://www.comsol.com/blogs/piezoelectric-materials-understan%20ding-standards/>
- [31] PI Ceramic, "Brochure of the dura-act piezoelectric patch transducer", February 2021. [Online].
- [32] PI Ceramic, "Specific parameters of the standard material" February 2021.
- [33] D. Valentin, A. Presas, E. Egusquiza, and C. Valero, "Influence of the added mass effect and boundary conditions on the dynamic response of submerged and confined structures," in *IOP Conference Series: Earth and Environmental Science*, vol. 22, 12 2014, p. 032042.
- [34] APC International Ltd., "Piezoelectric constants," February 2021. [Online]. Available: <https://www.americanpiezo.com/knowledge-center/piezo-theory/piezoelectric-consta%20nts.html>
- [35] PI Ceramic, "Piezoelectric materials," February 2021. [Online]. Available: <https://www.piceramic.com/en/products/piezoelectric-materials/>
- [36] C.G Rodriguez, E. Egusquiza, X. Escaler. Q.W. Liang. F.Avellan, "Experimental investigation of added mass effects on a Francis turbine runner in still water", *Journal of Fluids and Structure*, 2006
- [37] X.S.Botello, "Modelling and control of the vibration of a rotatory disk", *Escola Tecnica Superior d'Enginyeria Industrial de Barcelona*, 2021
- [38] Xavier Escaler, Oscar De la Torre, "Axisymmetric vibrations of a circular Chladini plate in air and fully submerged in water", *Journal of Fluids and Structure*, 2018
- [39] Ainara Duran Hervas, "Study of the fluid effects on a submerged circular plate", *Escola Tecnica Superior d'Enginyeria Industrial de Barcelona*, 2020
- [40] Amabili, "Effect of finite fluid depth on the hydroelastic vibrations of the circular and annular plates", *Journal of sound and vibrations*, 1996
- [41] A. Presas, D. Valentin, E. Egusquiza, C. Valero, U. Seidel, W. Weber, "Natural frequencies of rotating disk-like structures submerged viewed from the stationary frame", in *IOP Conference Series: Earth and Environmental Science*, 49 (2016) 082023.
- [42] Ehsan Askari, Kyeong-Hoon Jeong, Marco Amabili, "Hydroelastic vibration of circular plate immersed in a liquid filler container with free surface", *Journal of Sound and Vibration*, 2013



## 12. Appendix

### A CHARACTERISTIC OF THE PIEZOELECTRIC PATCH

#### A1 Piezoelectric effect

The piezoelectric effect is the property of a material to display an electric charge on its surface (producing a change in its polarization) under the application of external mechanical stress. On the contrary, the converse piezoelectric effect is the production of a mechanical strain due to a change in the polarization of the material.

To characterize the behavior of a piezoelectric patch, it is needed to define several material properties that define the relationship between the material polarization and its deformation. This relationship can be defined using two different ways: the *strain-charge* form or the *stress-charge* form [30].

The strain-charge form is written as:

$$\begin{aligned} S &= s_E T + d^T E \\ D &= d T + \epsilon_0 \epsilon_{tt} E \end{aligned} \quad (\text{A.1})$$

Where  $S[\frac{m}{m}]$  is the strain,  $T[\text{Pa}]$  is the stress,  $E[\frac{V}{m}]$  is the electric field and  $D[\frac{C}{m^2}]$  is the electric displacement field. The material parameters  $s_E[\frac{m^2}{N}]$ ,  $d[\frac{C}{N}]$  and  $\epsilon_{tt}$  are the material compliance, coupling properties, and relative permittivity at constant stress.  $\epsilon_0$  is the permittivity of free space, and it has a value of  $8.854 \times 10^{-12} [\frac{F}{m}]$ .

With this notation, the above equations can be written as:

$$\begin{pmatrix} S_{xx} \\ S_{yy} \\ S_{zz} \\ S_{yz} \\ S_{xz} \\ S_{xy} \end{pmatrix} = \begin{pmatrix} s_{E11} & s_{E12} & s_{E13} & s_{E14} & s_{E15} & s_{E16} \\ s_{E21} & s_{E22} & s_{E23} & s_{E24} & s_{E25} & s_{E26} \\ s_{E31} & s_{E32} & s_{E33} & s_{E34} & s_{E35} & s_{E36} \\ s_{E41} & s_{E42} & s_{E43} & s_{E44} & s_{E45} & s_{E46} \\ s_{E51} & s_{E52} & s_{E53} & s_{E54} & s_{E55} & s_{E56} \\ s_{E61} & s_{E62} & s_{E63} & s_{E64} & s_{E65} & s_{E66} \end{pmatrix} \begin{pmatrix} T_{xx} \\ T_{yy} \\ T_{zz} \\ T_{yz} \\ T_{xz} \\ T_{xy} \end{pmatrix} + \begin{pmatrix} d_{11} & d_{21} & d_{31} \\ d_{12} & d_{22} & d_{32} \\ d_{13} & d_{23} & d_{33} \\ d_{14} & d_{24} & d_{34} \\ d_{15} & d_{25} & d_{35} \\ d_{16} & d_{26} & d_{36} \end{pmatrix} \begin{pmatrix} E_x \\ E_y \\ E_z \end{pmatrix}$$

$$\begin{pmatrix} D_x \\ D_y \\ D_z \end{pmatrix} = \begin{pmatrix} d_{11} & d_{12} & d_{13} & d_{14} & d_{15} & d_{16} \\ d_{21} & d_{22} & d_{23} & d_{24} & d_{25} & d_{26} \\ d_{31} & d_{32} & d_{33} & d_{34} & d_{35} & d_{36} \end{pmatrix} \begin{pmatrix} T_{xx} \\ T_{yy} \\ T_{zz} \\ T_{yz} \\ T_{xz} \\ T_{xy} \end{pmatrix} + \epsilon_0 \begin{pmatrix} \epsilon_{rT11} & \epsilon_{rT12} & \epsilon_{rT13} \\ \epsilon_{rT21} & \epsilon_{rT22} & \epsilon_{rT23} \\ \epsilon_{rT31} & \epsilon_{rT32} & \epsilon_{rT33} \end{pmatrix} \begin{pmatrix} E_x \\ E_y \\ E_z \end{pmatrix}$$

**Figure 78 Strain-charge form representation of a piezoelectric material. Image from [30]**

On the contrary, the *stress-charge* form relates the physical properties as follows:

(A.2)

$$S = c_E T - e^T E$$

$$D = e T + \epsilon_0 \epsilon_{rs} E$$

The material parameters  $c_E \left[ \frac{N}{m^2} \right]$ ,  $e \left[ \frac{N}{Vm} \right]$  and  $\epsilon_{rs}$  correspond to the material stiffness, coupling properties, and relative permittivity at constant strain.

Within this notation, the above two equations can be written as:

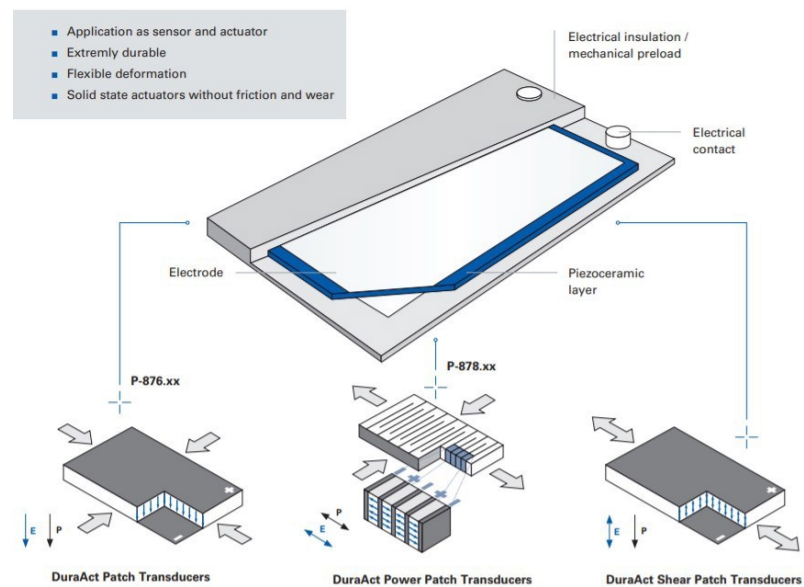
$$\begin{pmatrix} T_{xx} \\ T_{yy} \\ T_{zz} \\ T_{yz} \\ T_{xz} \\ T_{xy} \end{pmatrix} = \begin{pmatrix} c_{E11} & c_{E12} & c_{E13} & c_{E14} & c_{E15} & c_{E16} \\ c_{E21} & c_{E22} & c_{E23} & c_{E24} & c_{E25} & c_{E26} \\ c_{E31} & c_{E32} & c_{E33} & c_{E34} & c_{E35} & c_{E36} \\ c_{E41} & c_{E42} & c_{E43} & c_{E44} & c_{E45} & c_{E46} \\ c_{E51} & c_{E52} & c_{E53} & c_{E54} & c_{E55} & c_{E56} \\ c_{E61} & c_{E62} & c_{E63} & c_{E64} & c_{E65} & c_{E66} \end{pmatrix} \begin{pmatrix} S_{xx} \\ S_{yy} \\ S_{zz} \\ S_{yz} \\ S_{xz} \\ S_{xy} \end{pmatrix} + \begin{pmatrix} e_{11} & e_{21} & e_{31} \\ e_{12} & e_{22} & e_{32} \\ e_{13} & e_{23} & e_{33} \\ e_{14} & e_{24} & e_{34} \\ e_{15} & e_{25} & e_{35} \\ e_{16} & e_{26} & e_{36} \end{pmatrix} \begin{pmatrix} E_x \\ E_y \\ E_z \end{pmatrix}$$

$$\begin{pmatrix} D_x \\ D_y \\ D_z \end{pmatrix} = \begin{pmatrix} e_{11} & e_{12} & e_{13} & e_{14} & e_{15} & e_{16} \\ e_{21} & e_{22} & e_{23} & e_{24} & e_{25} & e_{26} \\ e_{31} & e_{32} & e_{33} & e_{34} & e_{35} & e_{36} \end{pmatrix} \begin{pmatrix} S_{xx} \\ S_{yy} \\ S_{zz} \\ S_{yz} \\ S_{xz} \\ S_{xy} \end{pmatrix} + \epsilon_0 \begin{pmatrix} \epsilon_{rS11} & \epsilon_{rS12} & \epsilon_{rS13} \\ \epsilon_{rS21} & \epsilon_{rS22} & \epsilon_{rS23} \\ \epsilon_{rS31} & \epsilon_{rS32} & \epsilon_{rS33} \end{pmatrix} \begin{pmatrix} E_x \\ E_y \\ E_z \end{pmatrix}$$

**Figure 79** Stress-charge form representation of a piezoelectric material. Image from [30]

## A.2 Piezoelectric patch P-876.A12hure



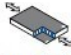
The piezoelectric patch used in the rotating disc is the Dura Act Piezoelectric Patch Transducer P-876.A12, from PI ceramics. This patch can either work as a sensor or an actuator, as it can generate and store an electrical charge using a laminated structure of piezoceramic, electrodes, and a polymer enclosure. The enclosure is used to electrically insulate the patch and make it mechanically robust, as it is shown in **Figure 80**.



**Figure 80** Composition of the piezoelectric patch from PI Ceramic, as well as the polarization direction of each model. Image from [31]

The P-876.A12 model, according to the brochure of the Dura Act Piezoelectric Transducers of PI ceramics (Figure A.4), works with an operating voltage that ranges from -100 to +400 V (thus, making it necessary to use an amplifier to achieve the +400 V), presents a maximum blocking force of 265 N and is composed by the piezoelectric material PIC255, which is based on modified lead zirconate titanate (PZT) and barium titanate.



		 DuraAct Patch Transducer				 DuraAct Power Patch Transducer	 DuraAct Shear Patch Transducer
		P-876.A11	P-876.A12	P-876.A15	P-876.SP1	P-878.A1	
Motion & positioning	Operating voltage range [V]	-50 to 200	-100 to 400	-250 to 1.000	-100 to 400	-20 to 120	
	Min. lateral/axial deformation [ $\mu\text{m}/\text{m}$ ]	400	650	800	650	250/1.200	
	Rel. lateral/axial deformation [ $\mu\text{m}/\text{V}$ ]	1,6	1,3	0,64	1,3	1,2/10	
Mechanical properties	Blocking force [N]	90	265	775	280	44	
	Min. bending radius [mm]	12	20	70	-	24	
Drive properties	Electrical capacitance [nF]	150 $\pm$ 20 %	90 $\pm$ 20 %	45 $\pm$ 20 %	8 $\pm$ 20 %	100 $\pm$ 20 %	Customized development on request
	Piezoceramic material	PIC255	PIC255	PIC255	PIC255	PIC252	
	Active piezoceramic thickness [ $\mu\text{m}$ ]	100	200	500	200	300	
Miscellaneous	Contacting	Solder points	Solder points	Solder points	Solder points	Solder points	
	Dimensions L x W x D (mm)	61 x 35 x 0,4	61 x 35 x 0,5	61 x 35 x 0,8	16 x 13 x 0,5	27 x 9,4 x 0,6	
	Recommended electronics	E-413, E-821, E-835	E-413, E-821, E-835	E-413, E-821, E-835	E-413, E-821, E-835	E-503, E-504, E-505, E-506, E-610, E-617, E-618, E-663, E-821, E-831, E-836	

**Figure 81** Composition of the piezoelectric patch, as well as the polarization direction of each model. Image from [31]

### A.3 Piezoceramic material PIC255

PZT materials can be classified as “soft” and “hard” PZT, depending on the mobility of the dipoles and, hence, on the polarization and depolarization behavior.

On the one hand, “soft” PZT materials are used for sensor and actuator applications, as they can be easily polarized even at low field strengths (they present large piezoelectric charge coefficients, moderate permittivity, and high coupling factors). Some other applications of soft PZT materials are used for micro-positioning, sensors such as conventional vibration detectors, ultrasonic transmitters, and receivers, or flow or level measurement, object identification or monitoring, and also as sound pickups on musical instruments. The piezoelectric materials classified as soft PZT are PIC151, PIC255, PIC155, PIC153, and PIC152.

On the other hand, “hard” piezoelectric materials can be subjected to high electrical and mechanical stresses, where their properties hardly change under these conditions. Therefore, hard PZT is used in high-power acoustic applications that include ultrasonic cleaning, machining of materials (ultrasonic welding, bonding, drilling,...), ultrasonic processors, the medical sector, and sonar technology. Some of these materials that are categorized as hard PZT are PIC181, PIC184, PIC144, PIC241, and

PIC300 [35].

As stated in the brochure information of Figure A.4, the material used in the DuraAct patch is the PIC255, which is defined as a soft PZT. The piezoelectric constants provided by the material datasheet of PI Ceramics are presented in Figure A.5.

		Unit	Soft PZT materials		
			PIC151	PIC255	PIC155
<b>Physical and dielectric properties</b>					
Density ( $\geq$ )	$\rho$	g/cm <sup>3</sup>	7.80	7.80	7.75
Curie temperature ( $\geq$ )	$T_c$	°C	250	350	340
Relative permittivity in the polarization direction $\perp$ to polarity	$\epsilon_{33}^T/\epsilon_0$ $\epsilon_{11}^T/\epsilon_0$		2400 1980	1850 1750	1550 1400
Dielectric loss factor ( $\leq$ )	$\tan \delta$	10 <sup>-3</sup>	20	20	25
<b>Electro-mechanical properties</b>					
Coupling factor	$k_p$		0.62	0.62	0.62
	$k_t$		0.53	0.47	0.48
	$k_{31}$		0.38	0.35	0.35
	$k_{33}$		0.69	0.69	0.69
	$k_{15}$		0.65	0.66	0.65
Piezoelectric charge coefficient	$d_{31}$	10 <sup>-12</sup> C/N	-210	-180	-165
	$d_{33}$		500	400	360
	$d_{15}$		610	550	540
Piezoelectric voltage coefficient	$g_{31}$	10 <sup>-3</sup> Vm/N	-11.5	-11.3	-12.9
	$g_{33}$		22	25	27
<b>Acousto-mechanical properties</b>					
Frequency coefficient	$N_p$	Hz·m	1950	2000	1960
	$N_1$		1500	1420	1500
	$N_3^*$		1750	1370	1780
	$N_t^*$		1950	2000	1990
	$N_5^*$		830	870	820
Elastic compliance coefficient	$S_{11}^E$	10 <sup>-12</sup> m <sup>2</sup> /N	15.0	16.1	15.6
	$S_{33}^E$		19.0	20.7	19.7
Elastic stiffness coefficient	$C_{33}^D$	10 <sup>10</sup> N/m <sup>2</sup>	10.0	15.6	11.1
Mechanical quality factor	$Q_m$		100	80	80
<b>Temperature stability</b>					
Temperature coefficient of $\epsilon_{33}^T$ (in the range of -20 °C bis +125 °C)	$TK \epsilon_{33}$	10 <sup>-3</sup> /K	4	3	4
<b>Time stability (relative change of the parameter per decade of time in %)</b>					
Relative permittivity	$C_\epsilon$	%		-1.0	-2.0
Coupling factor	$C_k$	%		-1.0	-2.0

**Figure 82** Specific parameters of the standard materials. Imagine from: [32]

The constants given by the manufacturer represent the following physical properties [34]:

- **Curie Temperature  $T_c$  [°C]**

The Curie Temperature is defined as the temperature at which the crystal structure of the material changes from a piezoelectric structure (non-symmetrical) to a non-piezoelectric structure (symmetrical), losing all its piezoelectric properties.

- **Dielectric Loss Factor  $\tan \delta$**

The dielectric loss factor, also known as the dissipation factor, is defined as the tangent of the dielectric loss angle  $\tan \delta$ , which determines the ratio of effective conductance to effective susceptance in a parallel circuit, measured by using an impedance bridge. The values for  $\tan \delta$  are usually determined at 1 kHz.

- **Permittivity constant  $E$**

The permittivity, also called dielectric constant  $E$ , is the dielectric displacement per unit of the electric field. Depending on the superscript of this constant it means that it is measured at constant stress  $E^T$  or constant strain  $E^S$ . The subscripts  $E_{ij}$  correspond to  $i$  the direction of the dielectric displacement and  $j$  the direction of the electric field.

The dielectric constant is usually given as a ratio of the permittivity of the material to the permittivity of free space  $E_0 = 8.854 \times 10^{-12} \text{ F/m}$ . The values given by the manufacturer for PIC255 are  $E^T = 1750 E_0$ , which is the permittivity for dielectric displacement and electric field in direction 1, and  $E^T = 1750 E_0$  which is the same but in direction 3, parallel to direction 1.

- **Electro-mechanical coupling factor  $k$**

This factor is defined as the ratio of the mechanical energy accumulated in response to an electrical input or vice versa. It is an indicator of the effectiveness with which a piezoelectric material converts electrical into mechanical energy, or converts mechanical into electrical energy. The first subscript of  $k$  denotes the direction along which the electrodes are applied, whereas the second subscript denotes the direction along which the mechanical energy is applied.

- **Piezoelectric charge coefficient  $d$**

It represents the polarization generated per unit of mechanical stress  $T$  [C/N] applied to a piezoelectric material or is the mechanical strain  $S$  experienced by a piezoelectric material per unit of the electric field applied [m/V]. The first subscript

indicates the direction of polarization generated in the material when the electric field,  $E$ , is zero. The second subscript is the direction of the applied stress. Alternatively, the first subscript can be the direction of the applied field strength, and the second one is the induced strain.

- **Piezoelectric voltage coefficient  $g$**

It is the ratio of the electric field generated by a piezoelectric material per unit of mechanical stress applied [Vm/N] or the mechanical strain experienced by a piezoelectric material per unit of electric displacement applied. The first subscript indicated the direction of the electric field generated in the material (or the direction of the applied electric displacement), whereas the second subscript is the direction of the applied stress (or the induced strain). This factor is important for assessing a material's suitability for sensing applications, as it depends on the strength of the induced electric field produced by a piezoelectric material in response to applied physical stress.

- **Acoustic-mechanical frequency coefficient  $N$**

The frequency coefficient  $N$  is the product of the resonance frequency  $f_s$  and the linear dimension of the ceramic element governing the resonance. Depending on the geometry of the patch it can be defined 3 differently constants: the Radial Mode Disc resonance frequency constant  $N_p = f_s \cdot D_\phi$  (where  $D_\phi$  is the diameter of the ceramic element), the Thickness Mode Disc frequency constant  $N_T = f_s \cdot h$  (where  $h$  is the thickness  $h$  of the ceramic element), and the Longitudinal Mode frequency constant  $N_L = f_s \cdot l$  (where  $l$  is the length of the element).

- **Elastic compliance coefficient  $s$**

Is the strain produced in a piezoelectric material per unit of stress applied and, for the 11 and 33 directions, is the reciprocal of the modulus of elasticity (Young's modulus  $Y$ )? We can distinguish between  $s^D$ , which is the compliance under a constant electric displacement  $D$ , and  $s^E$ , which is the compliance under a constant electric field  $E$ . The first subscript indicates the direction of strain and the second one the direction of stress.

Notice that, as the piezoelectric is an anisotropic material, all the piezoelectric constants provided by the manufacturer present two subscripts that relate the direction of the electric field associated with the voltage applied, or the charge produced, with the direction of mechanical

stress or strain. Superscripts indicate a constant mechanical or electrical boundary condition.

Normally, the direction of the positive polarization is made to coincide with the Z-axis of the rectangular system (subscript 3), where directions X and Y are represented by subscripts 1 and 2, respectively. Shear about this X, Y, and Z axis is represented by the subscripts 4, 5, and 6, respectively, as schematized in Figure A.6 [34].

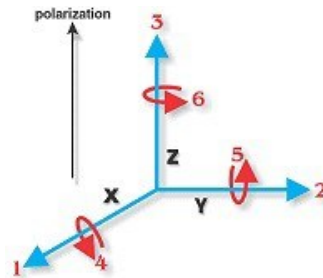


**Figure 83** Directions of forces affecting a piezoelectric element. Image from [34]

## B ANSYSIS

The main program used to perform the simulation is ANSYSIS, the *workbench environment* of it. During the simulation, the modal analysis, the harmonic analysis, the modal acoustic, and the harmonic acoustic analysis were performed.

The initial page of the workbench is shown in Figure 84, where is possible to add all the blocks from the Toolbox on the left. In this project, the modal analysis, the harmonic analysis, the modal acoustic, and the harmonic acoustic are inserted.

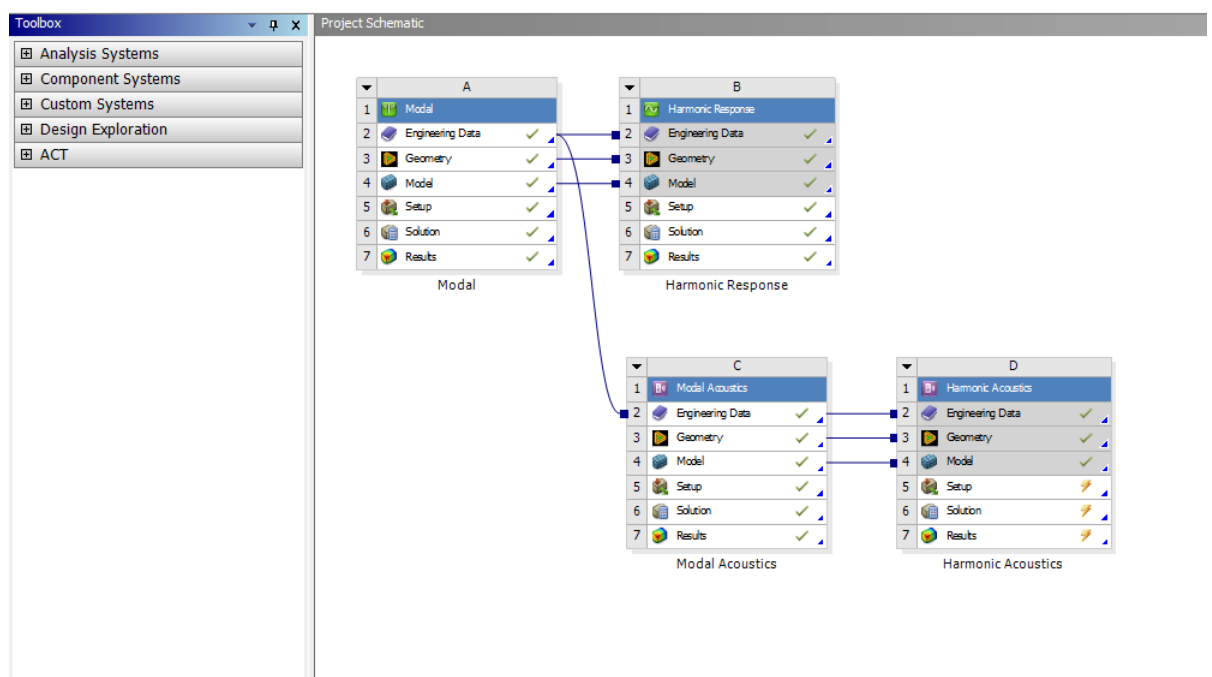
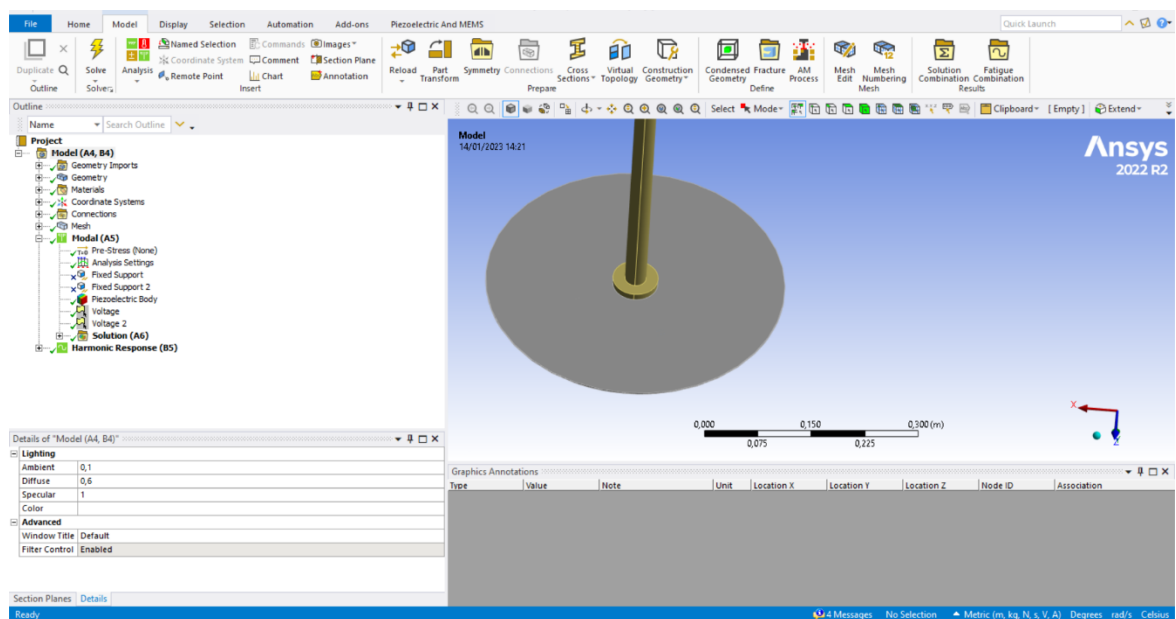


Figure 84 Workbench main page

## B.1 modal analysis

The first block is the modal analysis used to perform the simulation of a structure in the air. The first step is to import the geometry, from an external file, inside the **Geometry** section. After this, it is necessary to create a single geometry from all the parts of the structure, for doing this the **Designmodeler** has to be opened.

Once obtained one part of the model and the setup must be defined. Opening the section **model**, a new interface is shown, in **Figure 85**.



**Figure 85** New interface obtained from the model section

In the new page opened the block modal analysis is already in, the parameters that have to define are the range of frequency where the modal analysis has to be performed and the type of solution that has to be shown. The first one is possible to perform from the section **Analysis setting**, while the second part has to be defined which type of solution has to be performed. To obtain the several solutions it is necessary to open the section and then insert. **Figure 86** is illustrated how to obtain the mode shapes from a total deformation simulation

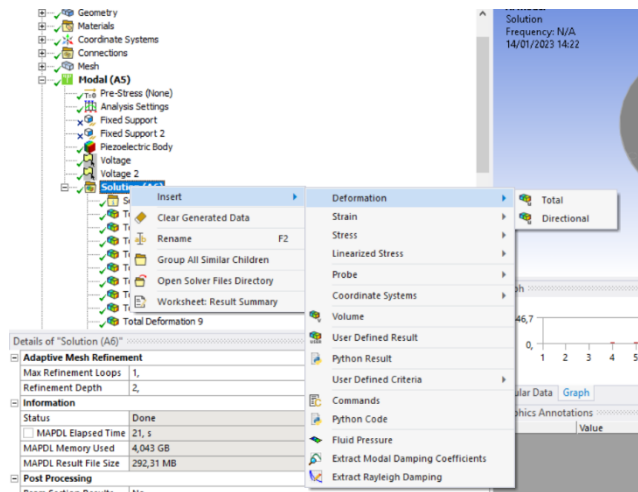


**Figure 86** Sequence to obtain the mode shapes from a total deformation simulation

In the modal analysis, there are no loads, so although the figure presents a piezoelectric patch there is no effect from this sensor. Moreover, it is possible to add some boundary conditions like **Fixed support** that implies the absence of stiffness, but it is better to define them in the previous section called **connections** where there are several possibilities of boundary condition, the ones used in this project **Bushing** that are a type of boundary condition that can represent the correct behavior of the bearings.

The last step is the possibility to add a **rotational velocity**, as a boundary condition, from the section modal (Figure 87). To define the rotation is possible to use a vector of the components of the velocity around the axis.

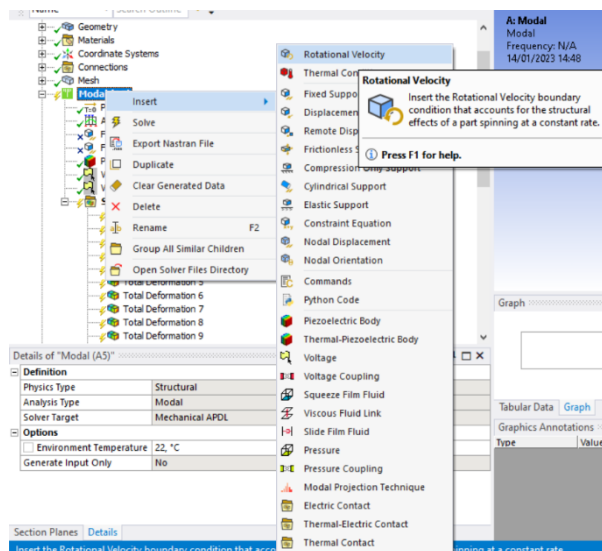


**Figure 87** Rotational velocity in modal analysis



## B.2 Harmonic analysis

The harmonic analysis is the second block of the simulation, adding it from the toolbox it is possible to connect the information about the materials, the geometry, and the model directly from the first page. That means that all the boundary conditions, the mesh, and the materials are the same as the modal analysis whether need to redefine everything.

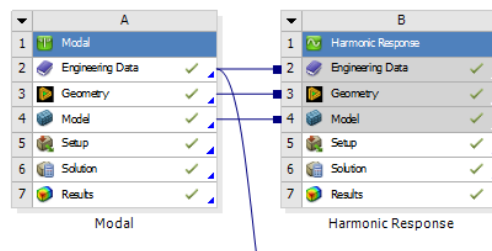


**Figure 88** Coupling between modal and harmonic analysis

Opening the section model the new environment as in modal analysis is opened. In the harmonic analysis is necessary to define an external load, in the specific case of the project it is necessary to add a piezoelectric patch, that is the sensor that excites the disk, and two voltages for the positive and negative layer. The voltage and the piezoelectric patch are added from the harmonic section, in **Figure 89** is shown how to insert a piezoelectric body.

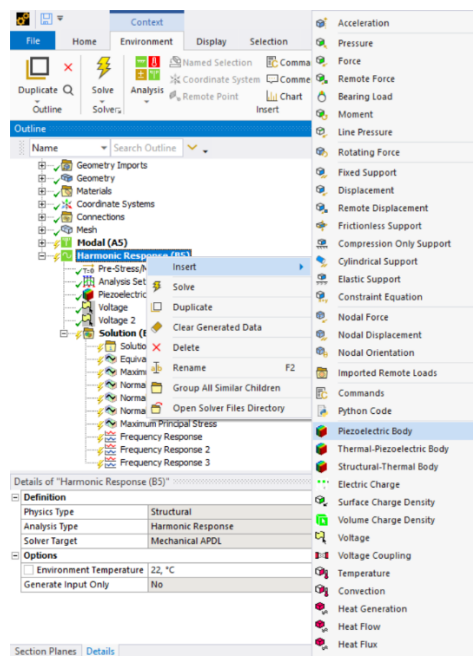


**Figure 89** Adding a piezoelectric body in harmonic analysis

The harmonic analysis is principally used to obtain the strain frequency response, to perform this analysis a strain frequency response has to be defined from the section analysis as it is shown in **Figure 90**.

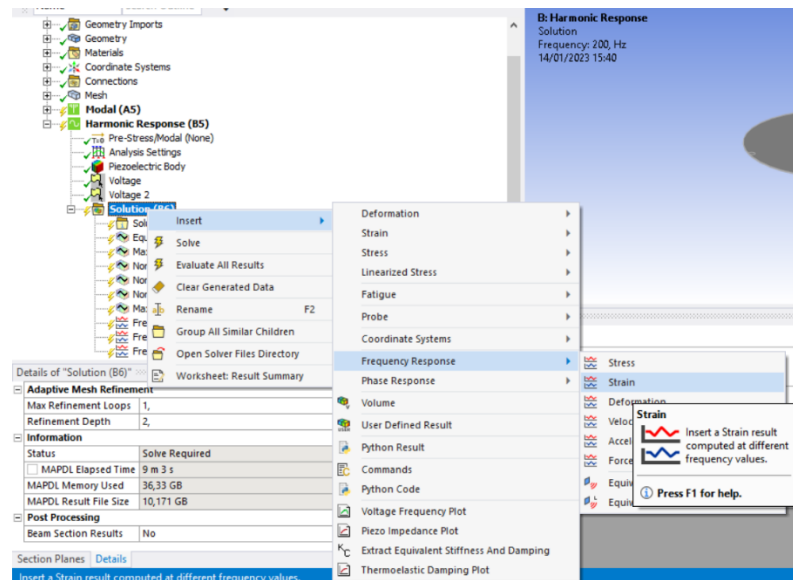


**Figure 90** Adding a strain frequency response

### B.3 Modal acoustic

The main difference between the modal acoustic with the modal analysis is the possibility to add fluid and perform the analysis considering the presence of a new element inside the simulating, thus to do this it is necessary to define three different surfaces so that the main structure and the fluid are considered as separate entities. Those surfaces are three *Acoustic regions*, that is the zone where the fluid is present, the *Physic region*, which is the main structure of the model, and the *Fluid Solid Interface* which is the most important part of the modal analysis definition of this interface that permits to simulate the fluid and the structure and merge the results where there is contact.

To define those entities, it is necessary to add them from the section *modal acoustic*, the first one that must be defined is the *Physic region* and then the *Fluid Solid Interface*, while the *Acoustic region* is already inserted by the software. **Figure 92** shows how to add the *Physic region*.

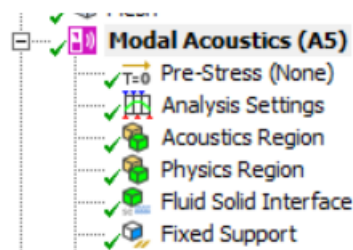


**Figure 91** Sections of the modal acoustic analysis

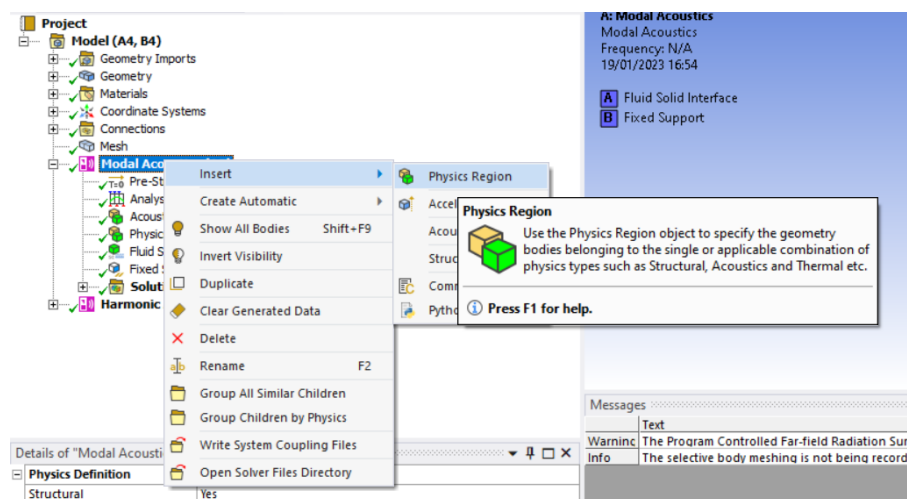
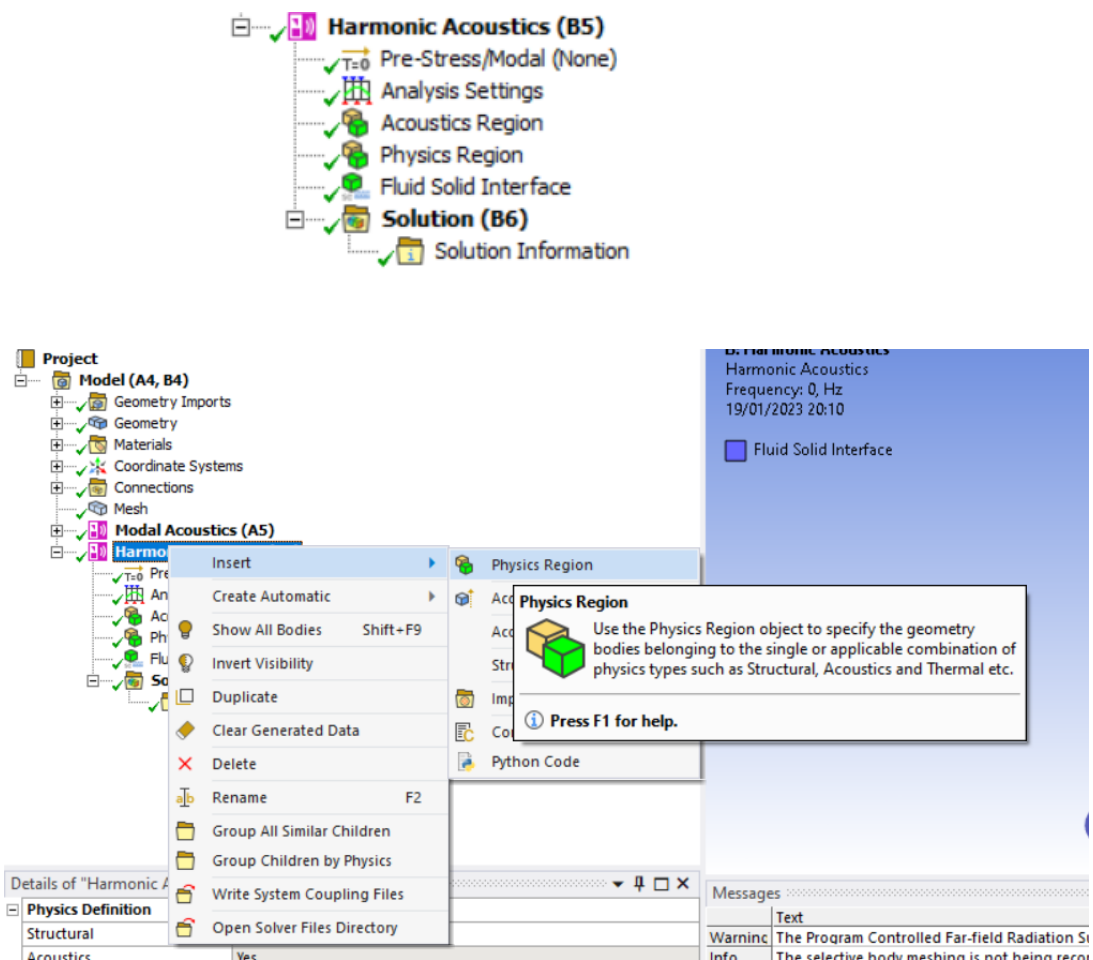


**Figure 92** Definition of a Physic region in modal analysis

## B.4 Harmonic modal analysis

This simulation aims to extract the strain frequency response as in harmonic analysis, the difference is the necessity of defining the *Acoustic region*, which is the zone where the fluid is present, the *Physic region*, which is the main structure of the model, and *Fluid Solid Interface* that is the most important part of the modal analysis, in fact, is the definition of this interface that permits to simulate the fluid and the structure and merge the results where there is contact., due to the presence of a fluid region.

To define those entities, it is necessary to add them from the section *harmonic acoustic*, the first one that must be defined is the *Physic region* and then the *Fluid Solid Interface*, while the *Acoustic region* is already inserted by the software. **Figure 92** shows how to add the *Physic region*.



## C LabVIEW

LabVIEW is the software used to extract the temporal signal, FFT, and FRF from the laboratory results. The interface is very simple as it is possible to see in Figure 93.

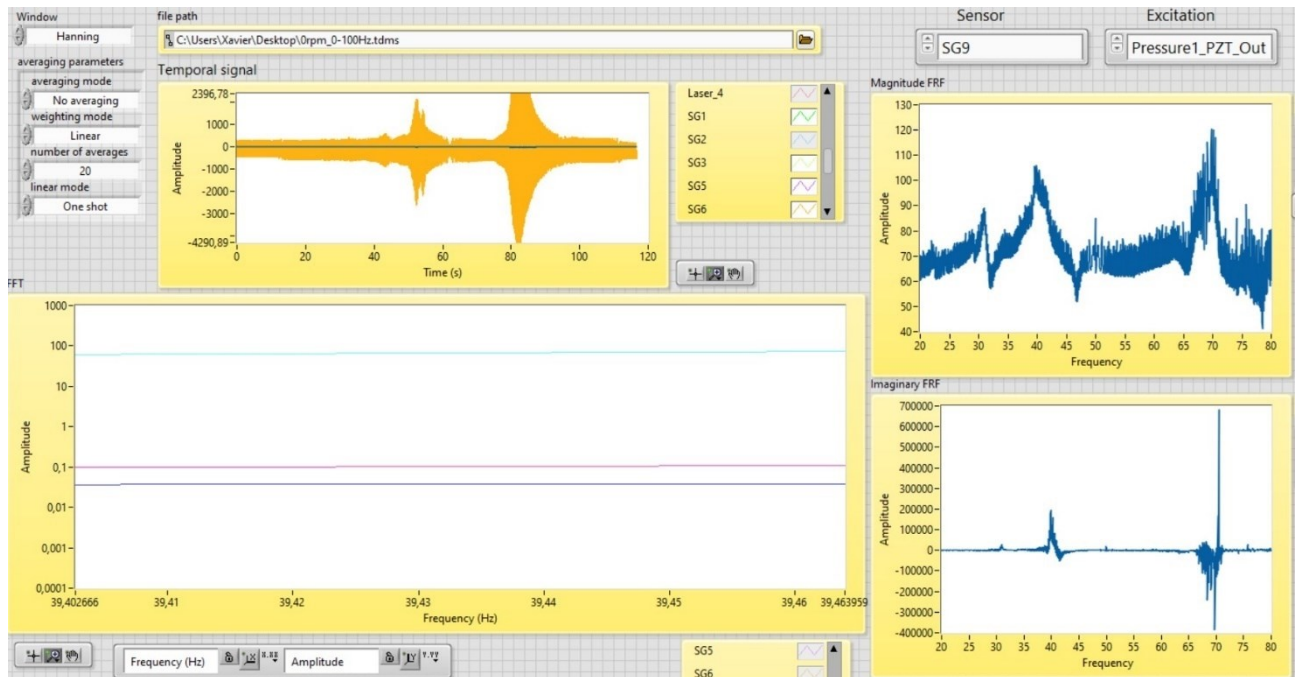


**Figure 93** Interface of LabVIEW

On the top, where there is the section *file path*, it is possible to insert the file tdms that contains the laboratory information. Once fill in this section all the information about the temporal signal, FRF and FFT is presented immediately presented by the software.

On the right top there are two sections called *sensor and excitation*, in the first one the sensors are chosen to obtain a specific FRF, while in the second section, it is chosen the sensor that creates the excitation, in the case of the project is a piezoelectric patch called *Pressure1\_PZT\_Out*.

In the graph of the FFT, all the sensors are already inside the graph but it is possible selecting and deselect a signal view with a right-click on the table located in the right corner at the bottom of the FFT graph.

All the signals can be exported on excel with a right click on the center of the graphs.

## D. RESULTS OF THE HARMONIC ANALYSIS IN AIR

To lighten the report many of the graphs were not included especially the ones of the SFR. In this appendix the are collected.

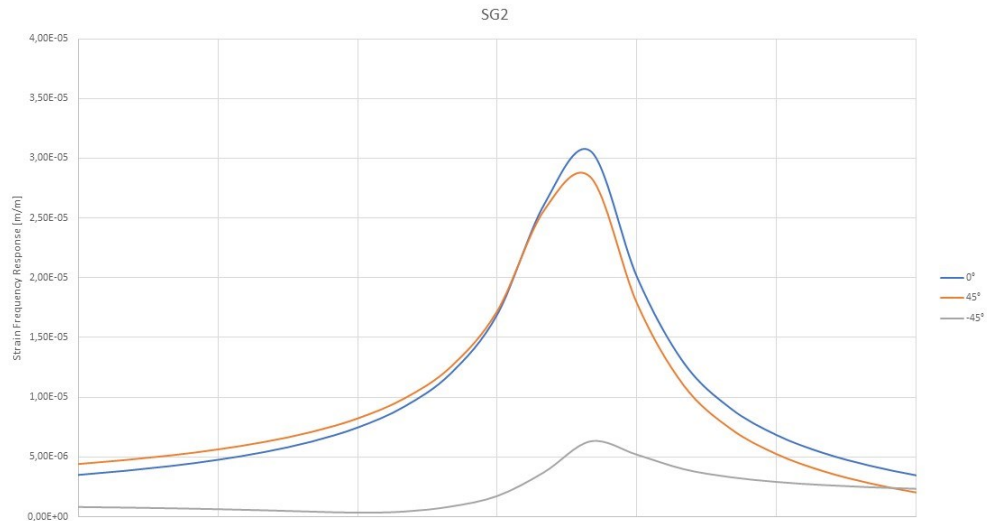


**Figure 94** Peak of 1ND in Strain Frequency Response

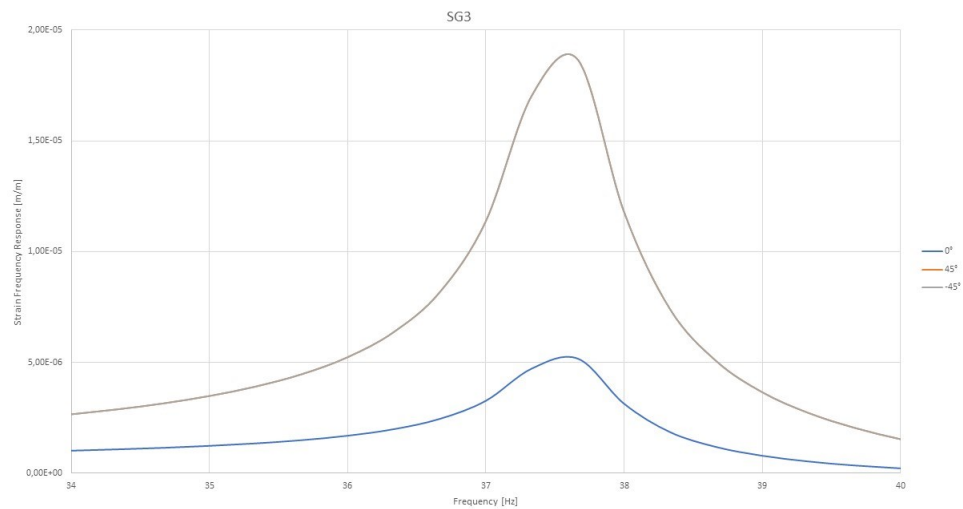


**Figure 95** Peak of amplitude of 1ND analyzed by the SG3 along three directions

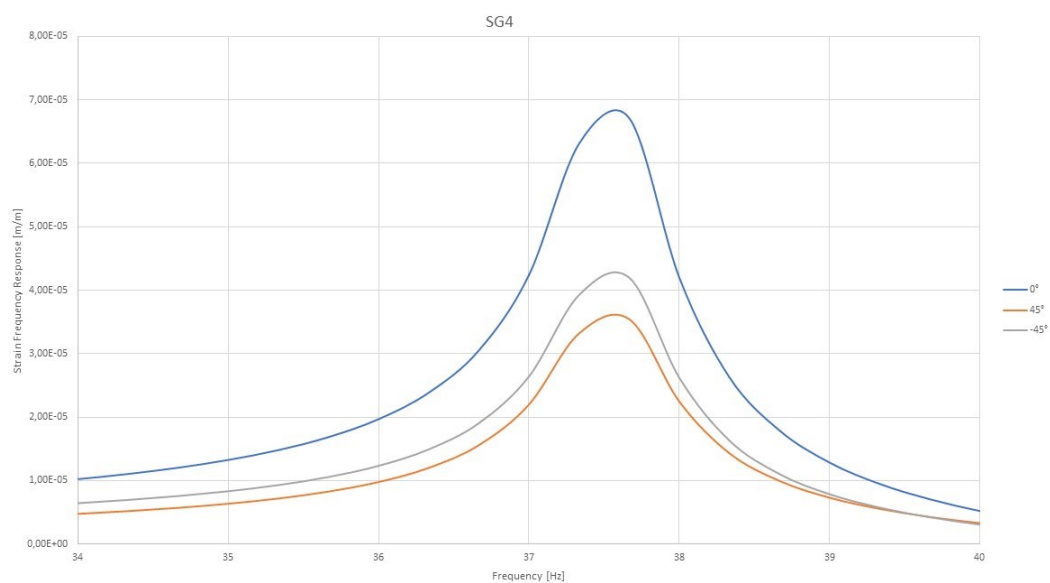


**Figure 96** Peak of the amplitude of 1ND analyzed by the SG4 along three directions

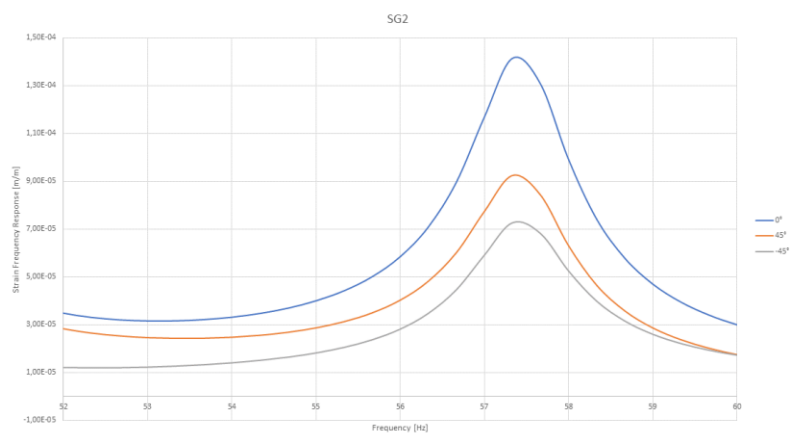


**Figure 97** Peak of the amplitude of 0NC analyzed by the SG4 along three directions

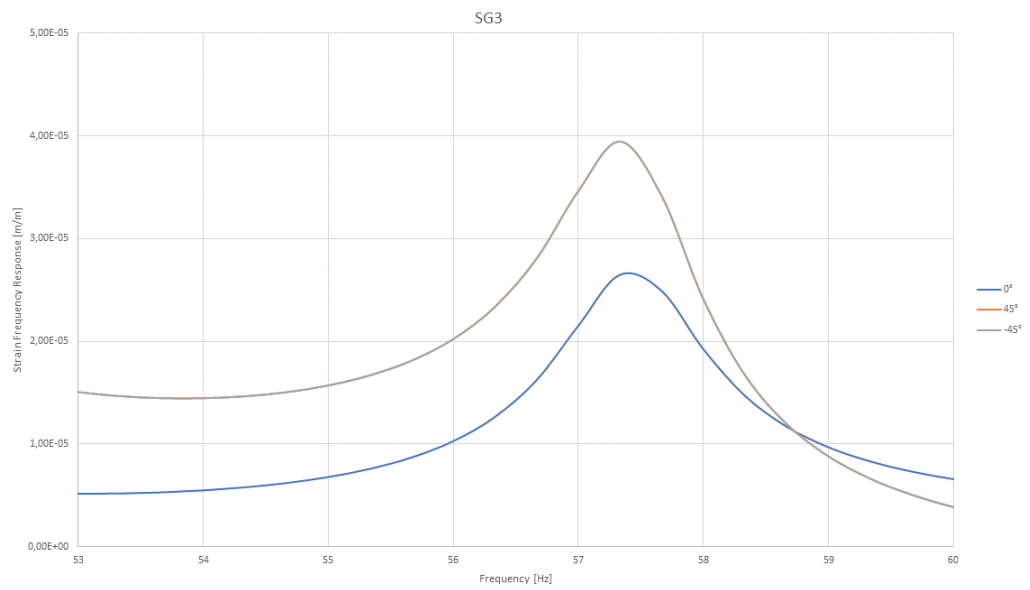


**Figure 98** Peak of the amplitude of 0NC analyzed by the SG3 along three directions

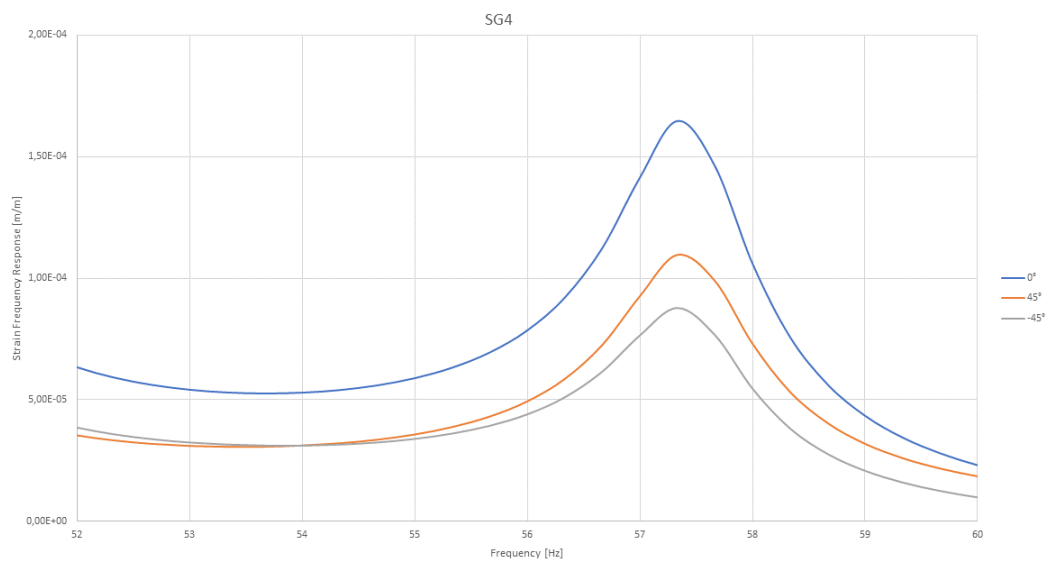


**Figure 99** Peak of the amplitude of 0NC analyzed by the SG4 along three directions



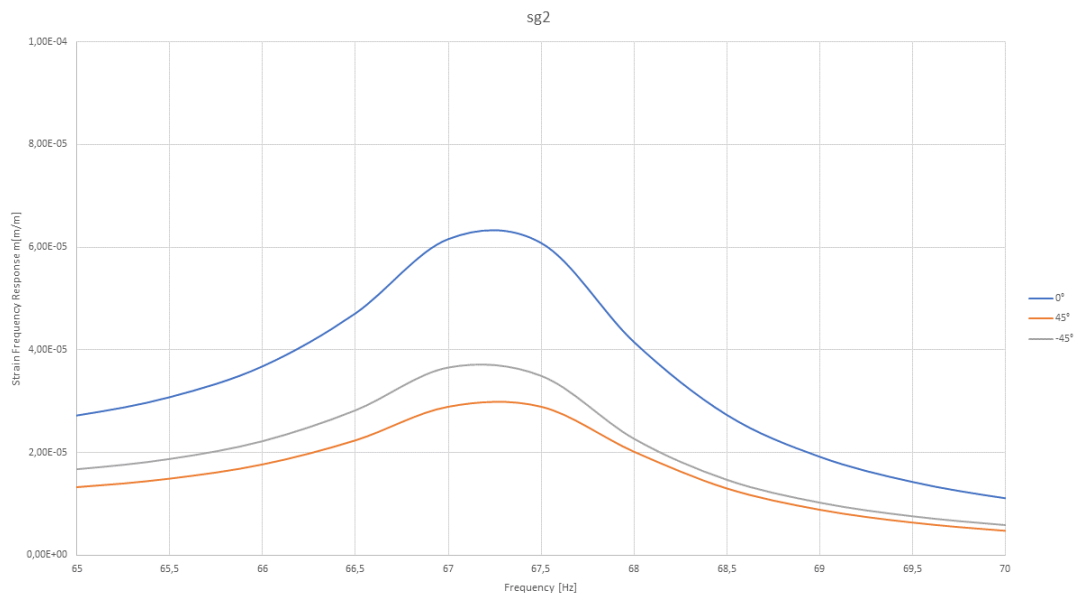


**Figure 100** Peak of the amplitude of 2ND analyzed by the SG2 along three directions

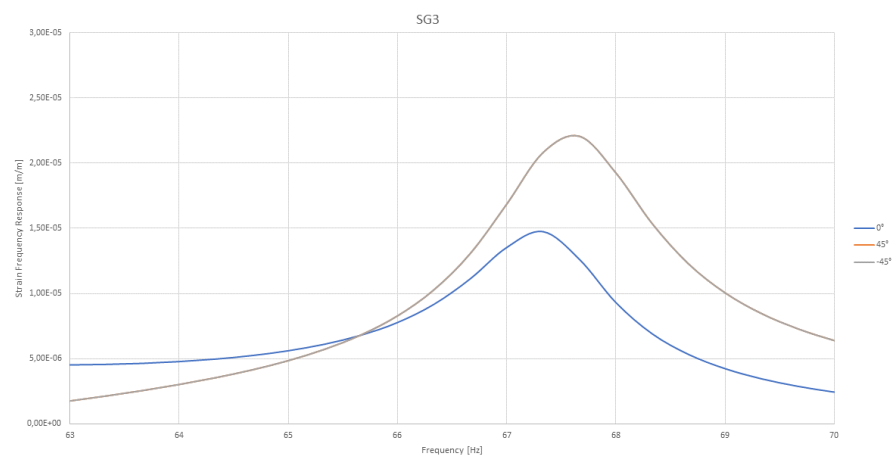


**Figure 101** Peak of the amplitude of 2ND analyzed by the SG2 along three directions

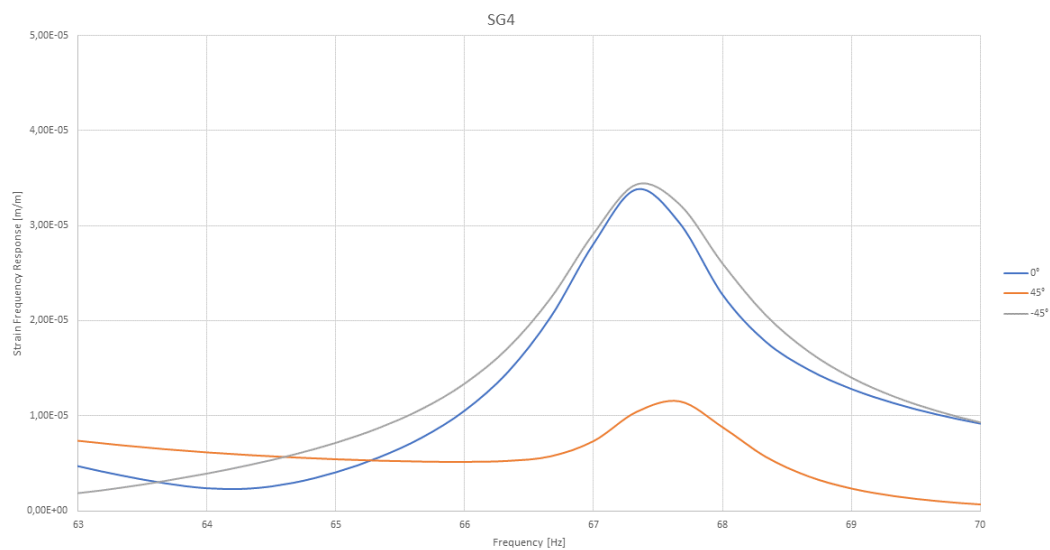


**Figure 102** Peak of the amplitude of 2ND analyzed by the SG3 along three directions

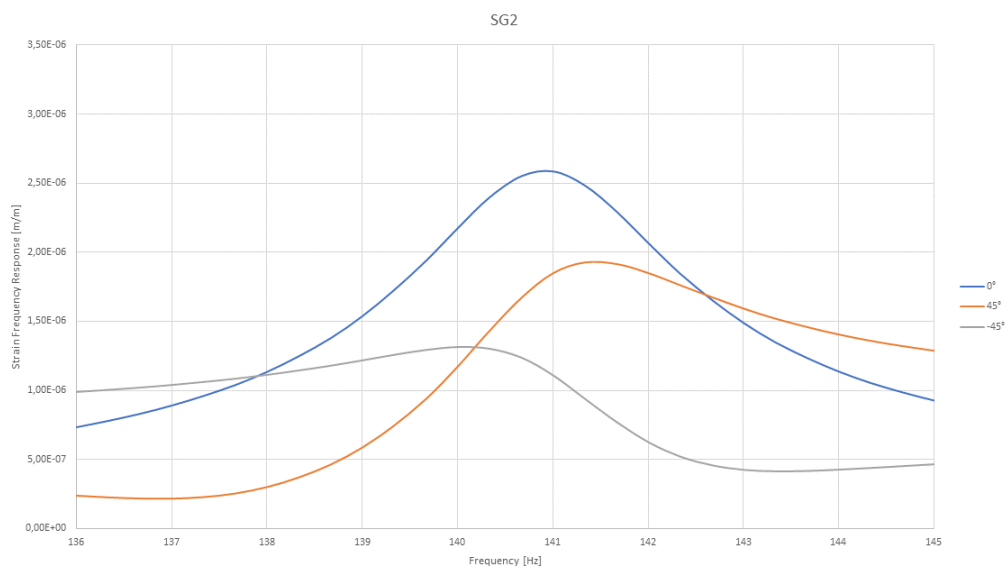


**Figure 103** Peak of the amplitude of 3ND analyzed by the SG2 along three directions

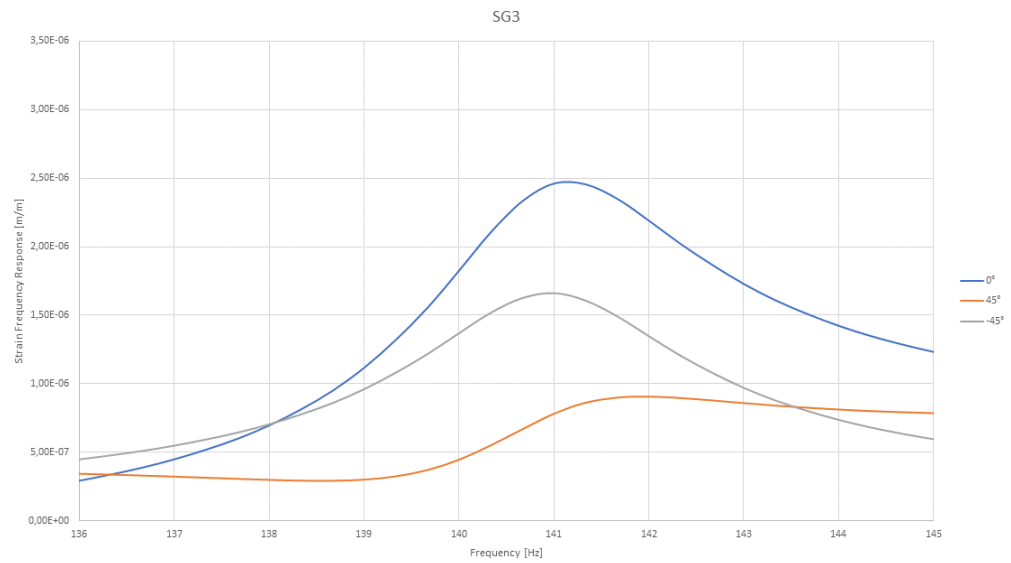


**Figure 104** Peak of the amplitude of 3ND analyzed by the SG3 along three directions

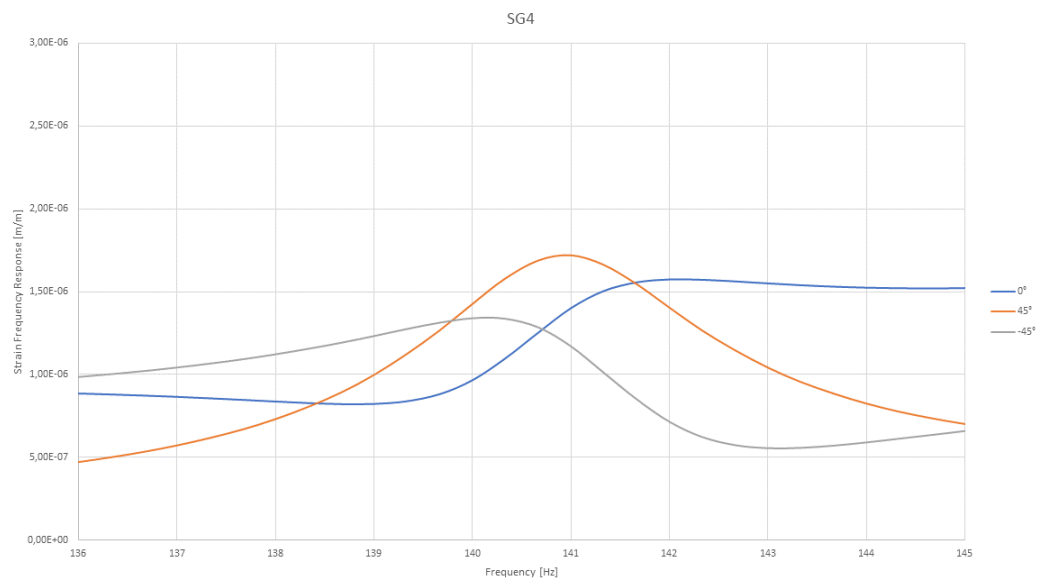


**Figure 105** Peak of the amplitude of 3ND analyzed by the SG4 along three directions

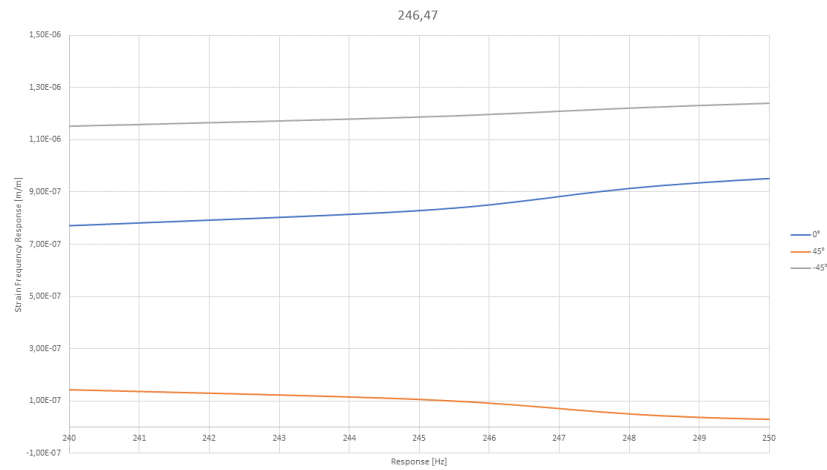


**Figure 106** Peak of the amplitude of 4ND analyzed by the SG2 along three directions

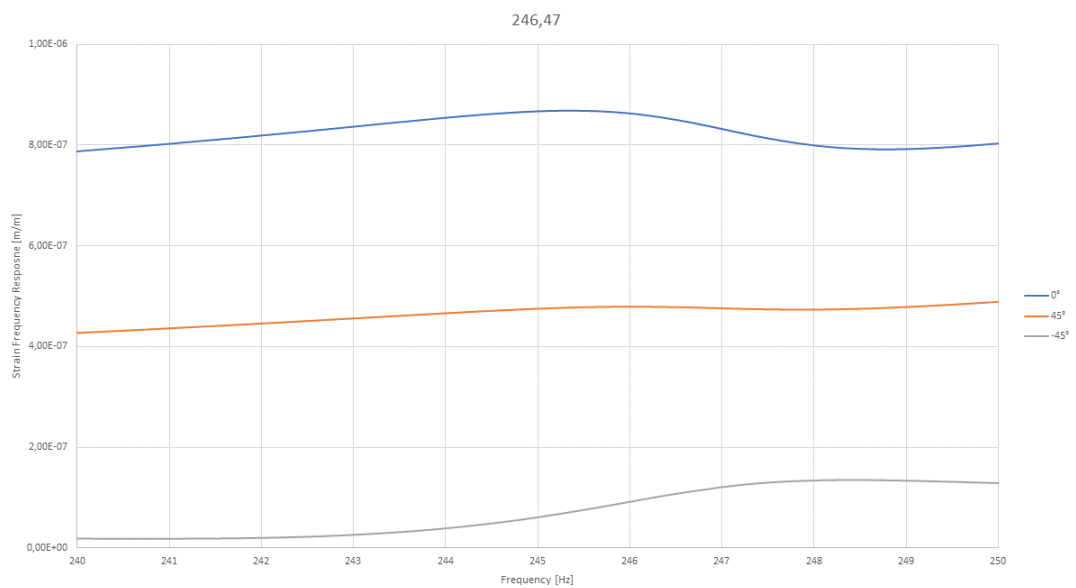


**Figure 107** Peak of the amplitude of 4ND analyzed by the SG3 along three directions

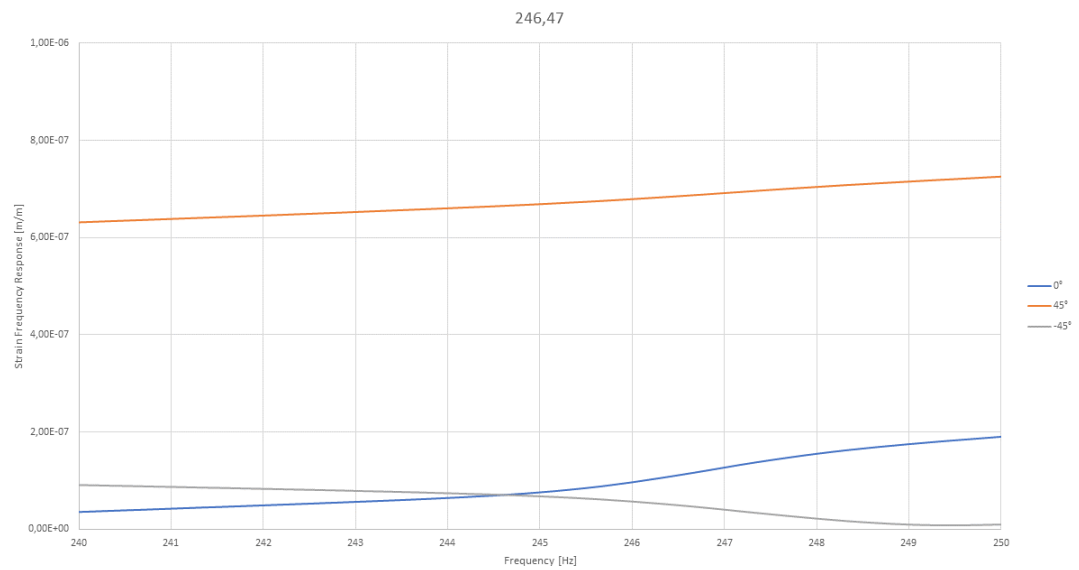


**Figure 108** Peak of the amplitude of 4ND analyzed by the SG4 along three directions

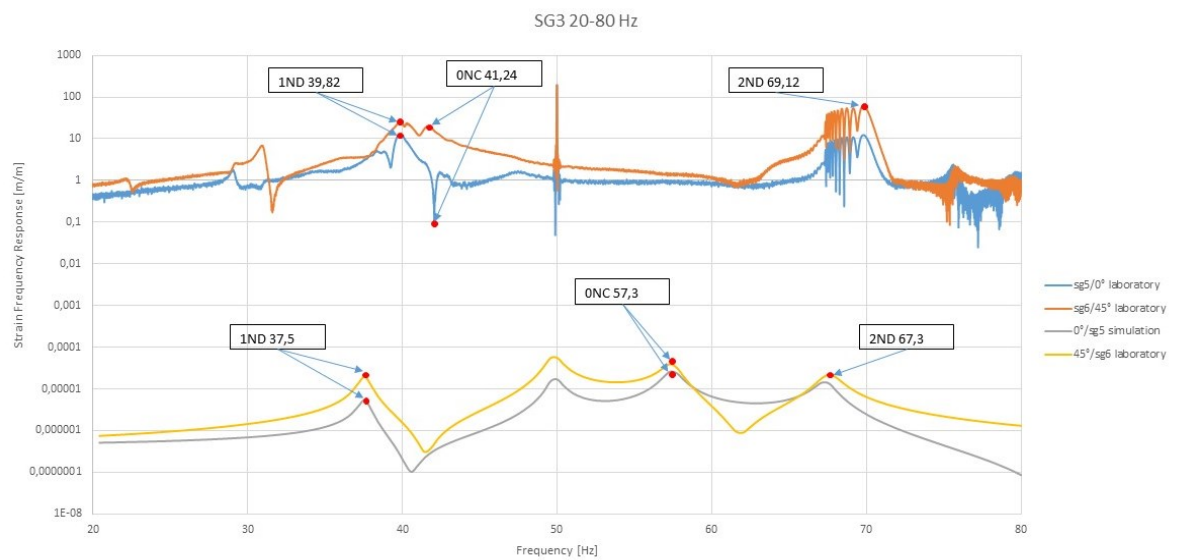


**Figure 109** Strain gauges signal from laboratory and simulation for SG3

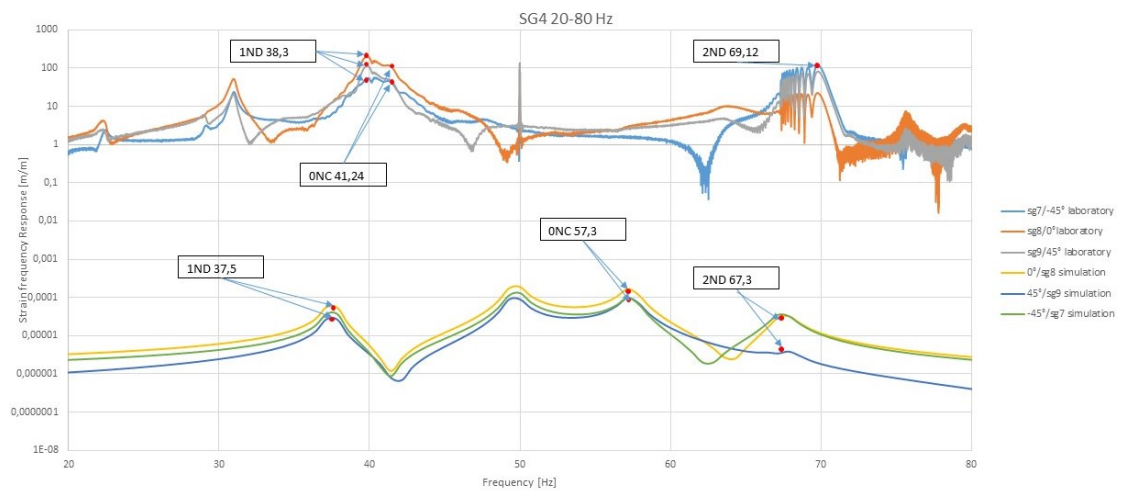


**Figure 110** Strain gauges signal from laboratory and simulation for SG4

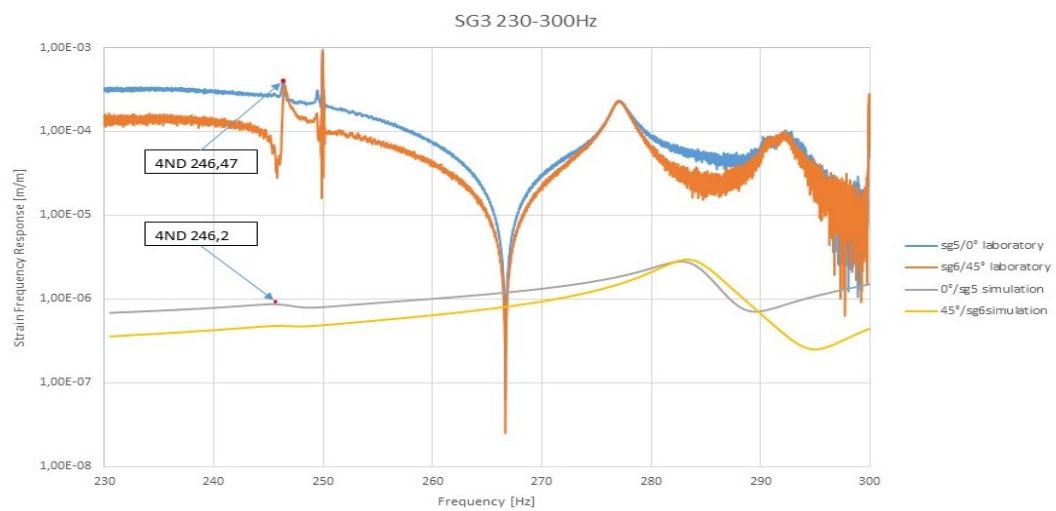


**Figure 111** Strain gauges signal from laboratory and simulation for SG3

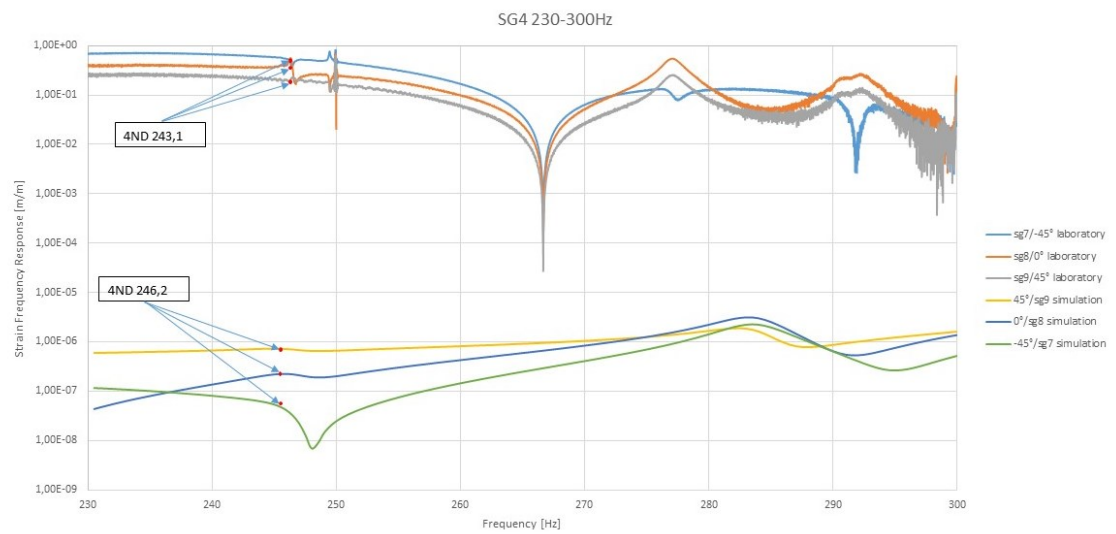


**Figure 112** Strain gauges signal from laboratory and simulation for SG4

### Graph of the disk submerged in water:

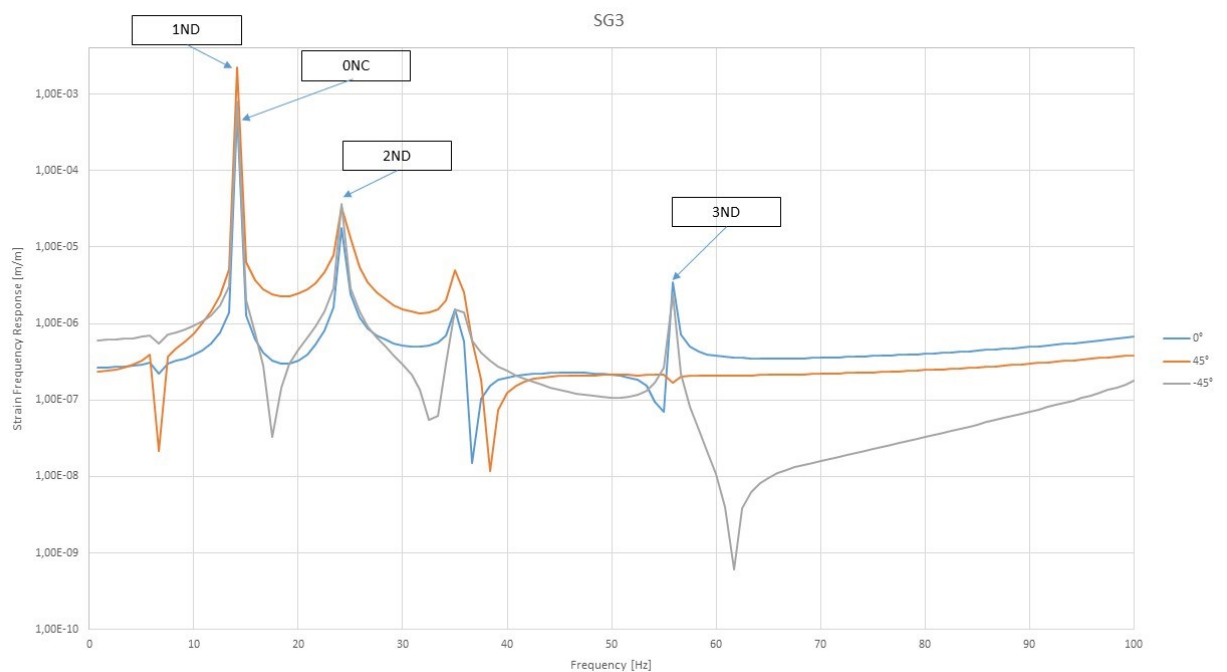


**Figure 113** Peaks of the amplitude for the SG3 in the range of frequency 0-100Hz

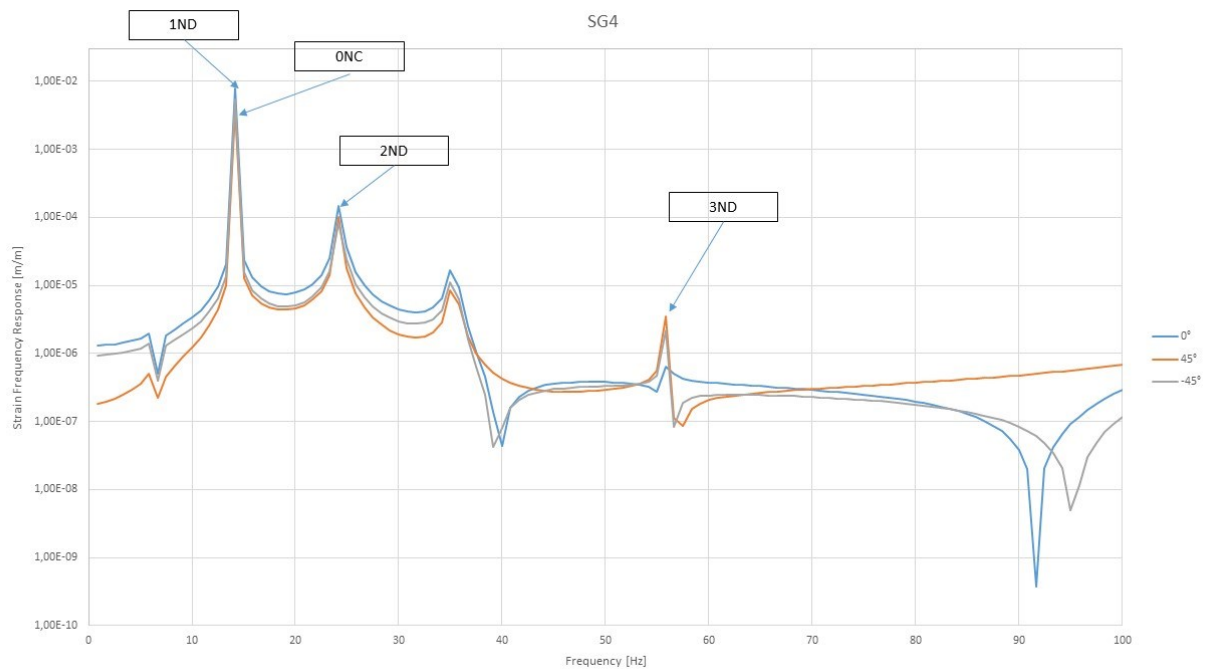


**Figure 114** Peaks of the amplitude for the SG4 in the range of frequency 0-100Hz

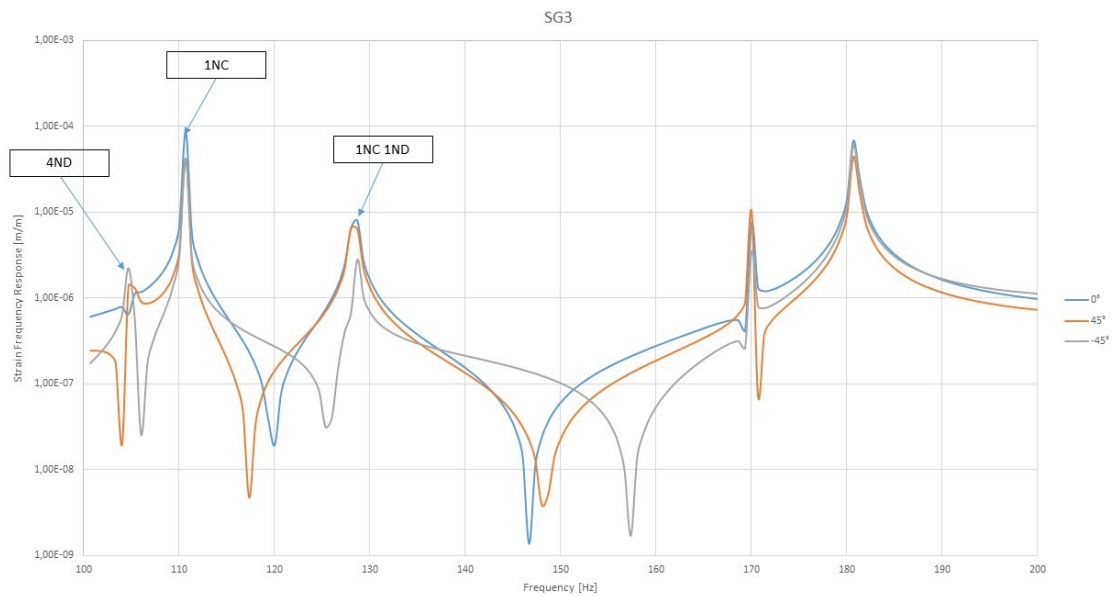


**Figure 115** Peaks of the amplitude for the SG3 in the range of frequency 100-200Hz



## E. COORDINATE SYSTEMS FOR THE THREE SG

The strain gauge can detect the deformation and the strain of a structure in a particular spot, in the case of the project the strain gauges can detect the signal in three different directions, To analyze the three directions in the simulation it is necessary to define three coordinate systems: one is in the radial direction ( $0^\circ$ ) and the other two are at  $45^\circ$  and  $-45^\circ$  relative to the radial direction. The following figures are illustrated the three coordinate systems for SG2, SG3, and SG4.

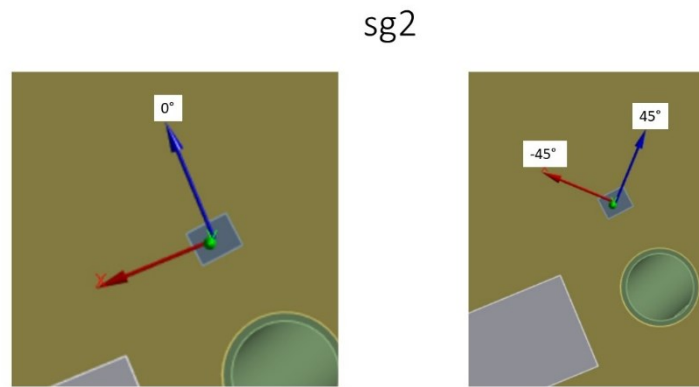


**Figure 116** Illustration of the three directions of the SG2



**Figure 117** Position of the SG3 on the bottom and the three directions of analysis

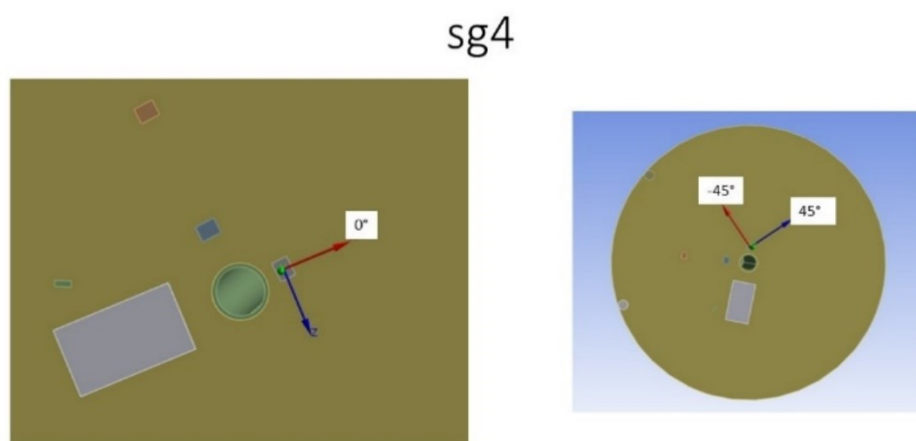


**Figure 118** Position of the sg4 on the top of the disk and the three directions of analysis

## Acknowledgments

First of all, I would like to thank all my family who have always supported me during these years. Secondly, I want to thank Professor Xavier Escaler and Xavier Botello who followed me during these months and gave me all the support I needed, and Professor Giovanna Cavazzini who has allowed me to carry out this experience. Thank you to all my friends from the MongolPerzen group that will follow me to Mongolia, to my lifelong friends, My roommates who have put up with me for five years, friends from university, the amazing people I met in Erasmus who made this experience unforgettable: Francesca, I Francesco, Rosario, Claudia, Andrea, Matteo, Hugo and Raphael. A big thanks to the love of my life, Eleonora, who despite the thousand moments spent far away is still here to support me and put supporting me for nine years, I would like to thank you for all the moments spent together and all the future ones, I probably wouldn't be here without you and I wouldn't have arrived where I am today, thank you, I love you.

*"Fare o non fare, non c'è provare". cit. Yoda*